



## 저작자표시-비영리-변경금지 2.0 대한민국

이용자는 아래의 조건을 따르는 경우에 한하여 자유롭게

- 이 저작물을 복제, 배포, 전송, 전시, 공연 및 방송할 수 있습니다.

다음과 같은 조건을 따라야 합니다:



저작자표시. 귀하는 원저작자를 표시하여야 합니다.



비영리. 귀하는 이 저작물을 영리 목적으로 이용할 수 없습니다.



변경금지. 귀하는 이 저작물을 개작, 변형 또는 가공할 수 없습니다.

- 귀하는, 이 저작물의 재이용이나 배포의 경우, 이 저작물에 적용된 이용허락조건을 명확하게 나타내어야 합니다.
- 저작권자로부터 별도의 허가를 받으면 이러한 조건들은 적용되지 않습니다.

저작권법에 따른 이용자의 권리는 위의 내용에 의하여 영향을 받지 않습니다.

이것은 [이용허락규약\(Legal Code\)](#)을 이해하기 쉽게 요약한 것입니다.

[Disclaimer](#)

약학박사 학위논문

# Mixture Analysis Using High-Resolution $^{13}\text{C}$ - $^{13}\text{C}$ NMR Spectra

고해상도  $^{13}\text{C}$ - $^{13}\text{C}$  NMR 스펙트럼을 활용한  
혼합물 분석

2020 년 8 월

서울대학교 대학원

약학과 천연물과학 전공

차 진 욱



## Abstract

# Mixture Analysis Using High-Resolution $^{13}\text{C}$ - $^{13}\text{C}$ NMR Spectra

Jin Wook Cha

Natural Products Science

College of Pharmacy

The Graduate School

Seoul National University

The homonuclear  $J$ -coupling interaction between  $^{13}\text{C}$  nuclei is very important information for the structure analysis based on NMR spectroscopy of organic compounds especially consisting of carbon skeleton. However, due to the low natural abundance of  $^{13}\text{C}$  nuclei, its utilization was made in very limited areas. In this study, novel NMR analysis methods that can be applied to natural/mixed and metabolite analysis using  $^{13}\text{C}$ - $^{13}\text{C}$  coupling interactions was presented.

First, the method of generating a high-resolution  $^{13}\text{C}$ - $^{13}\text{C}$  correlation spectrum through a two-dimensional  $^1\text{H}$ - $^{13}\text{C}$  HMBC spectrum was studied and applied to actual natural compound to evaluate their feasibility of structural analysis. In addition,

DECODE procedure was devised for structural analysis of complex natural products from this obtained  $^{13}\text{C}$ - $^{13}\text{C}$  correlation spectrum. It was then confirmed that this could be applied to a mixture of actual natural compound to extract  $^{13}\text{C}$  spectra of individual pure compounds from the NMR spectrum of the mixture. When applied to a complex natural product mixture of rotenone and brucine with many quaternary carbons, the method resolved very close carbon peaks and extracted clean individual spectra. Essentially providing molecule-wide  $^{13}\text{C}$  connectivity for complex molecules from  $^1\text{H}$ -detected 2D spectra, our approach should prove useful in many areas of NMR analysis.

Next, novel  $^1\text{H}$ - $^{13}\text{C}$  HSQC method was developed to effectively analyze  $J_{\text{CC}}$ -coupling information of  $^{13}\text{C}$ -isotope labeled compounds commonly used in cellular metabolite analysis. To this end, a modification of HSQC pulse sequence which can suppress the signal distortion were carried out and  $J$ -scaling module which can selectively amplifying the  $J_{\text{CC}}$  interaction also employed to the pulse sequence. The usefulness of novel HSQC pulse sequence was evaluated by several types of uniformly labeled  $^{13}\text{C}$ -isotope compounds such as U- $^{13}\text{C}$  acetate and U- $^{13}\text{C}$  lactate which are frequently encountered in cellular metabolic analysis. As a result, while conventional HSQC spectrum provide phase-distorted and poor-resolution signals, the resulted HSQC spectrum gives pure in-phase  $J_{\text{CC}}$  scaled HSQC signals of  $^{13}\text{C}$ -isotope labeled compounds. Since the novel HSQC sequence can provide high-resolution signals due to  $^{13}\text{C}$ - $^{13}\text{C}$  interactions within relatively short acquisition time, it could be applicable to the real-time NMR metabolomics which limited measurement time.

**Keywords:**  $^{13}\text{C}$ - $^{13}\text{C}$  correlation,  $J$ -coupling, covariance, spectral deconvolution, mixture analysis, natural products

**Student number:** 2016-30517

# Table of Contents

<b>Abstract.....</b>	<b>i</b>
<b>Table of Contents.....</b>	<b>iii</b>
<b>List of Figures.....</b>	<b>viii</b>
<b>List of Abbreviations.....</b>	<b>x</b>
<b>1 Introduction.....</b>	<b>1</b>
<b>2 Theoretical basis of NMR spectroscopy .....</b>	<b>5</b>
2.1 Free evolution of the density operator.....	6
2.1.1 The wave function and the density matrix.....	6
2.1.2 The evolution of the density operator.....	7
2.2 Rotations of the density operator .....	8
2.2.1 Transformation of the spin density operator.....	8
2.2.2 Effect of non-selective inversion for the bilinear operator .....	9
2.3 Evolution of the Cartesian operator .....	10
2.3.1 Free precession .....	10
2.3.2 Chemical shift and $J$ -coupling evolution of the density operator.....	10
2.3.3 Spin-echo pulse sequence.....	11
2.4 Frequency discrimination and lineshape in 2D NMR.....	13
2.4.1 Properties of the indirect domain signal in 2D NMR.....	13
2.4.2 The States-Haberkorn-Ruben (SHR) method.....	14
2.4.3 Time-Proportional Phase-Incrementation (TPPI) method.....	15
2.5 Coherence selection by PFG .....	17
2.5.1 Magnetic field gradient.....	17
2.5.2 Phase evolution of the coherence in magnetic field gradient .....	17

2.5.3	Acquiring a spatially dependent phase by the PFG.....	18
2.5.4	Dephasing by the field gradient.....	19
2.5.5	Selection of P-type and N-type spectra by the PFG.....	20
2.6	Adiabatic fast passage.....	22
2.6.1	Adiabatic condition .....	22
2.6.2	Pros of the adiabatic fast passage .....	23
2.6.3	Cons of the adiabatic fast passage .....	23
<b>3</b>	<b>DECODE procedure for spectral deconvolution.....</b>	<b>24</b>
3.1	Introduction .....	25
3.2	Theoretical and experimental backgrounds in DECODE .....	28
3.2.1	Covariance NMR Spectroscopy .....	28
3.2.2	Theory of the covariance NMR spectroscopy .....	28
3.2.3	Relationship between 2D NMR and Covariance NMR.....	29
3.2.4	Speeding up the eigen-decomposition by SVD.....	31
3.2.5	Indirect Covariance NMR spectroscopy.....	32
3.3	Spectral deconvolution of mixture using Covariance NMR .....	33
3.3.1	Relationship between PCA and Covariance NMR .....	33
3.3.2	NMR mixture analysis using PCA .....	33
3.4	High-quality HMBC spectra using NUS-mHMBC .....	35
3.4.1	Resolution enhancement of the indirect domain .....	35
3.4.2	Modification of the HMBC pulse sequence .....	36
3.5	Experimental section.....	39
3.5.1	NMR measurements .....	39
3.5.2	NUS sampling schedule. ....	39
3.6	Results and discussion.....	41
3.6.1	High-resolution mHMBC spectrum with NUS acquisition .....	41

3.6.2	iCov on NUS-mHMBC for $^{13}\text{C}$ - $^{13}\text{C}$ correlation spectrum.....	43
3.7	Mixture analysis with iCov-NUS-mHMBC spectrum.....	46
3.7.1	Limitations of iCov for the spectral deconvolution.....	46
3.7.2	The heterogeneity of HMBC correlation information.....	47
3.7.3	Signal overlap on the $F_2$ projection domain.....	49
3.7.4	Disproportion of the signal intensity.....	50
3.7.5	Undesirable covariance signal line shape.....	51
3.8	Signal processing tailored to iCov-eigendecomposition.....	53
3.8.1	Spectral merging.....	53
3.8.2	Calculation of the first moment for the spectral moment filtering ....	54
3.8.3	iCov calculation with the spectral moment filtering function .....	54
3.8.4	Dataset normalization.....	55
3.8.5	Peak-digitization.....	56
3.8.6	Extracting eigenmodes; individual 1D spectra.....	57
3.8.7	An optional $J$ -modulation-based overlap filter.....	58
3.9	Experimental section.....	62
3.9.1	NMR measurements.....	62
3.9.2	DECODE processing.....	62
3.10	Results and discussion.....	63
3.11	Conclusion.....	72
<b>4</b>	<b><math>^{13}\text{C}</math>-<math>^{13}\text{C}</math> distortion-free <math>J</math>-scaled HSQC.....</b>	<b>74</b>
4.1	Introduction.....	75
4.2	Origin of the HSQC signal distortion by $J_{\text{CC}}$ -coupling.....	77
4.2.1	Evolution of $J$ -couplings during finite length of delays.....	77
4.2.2	Analysis of NMR signal: AX spin system.....	78
4.2.3	Analysis of NMR signal: A general case.....	82



4.3	Experimental section .....	84
4.3.1	NMR measurements .....	84
4.3.2	Simulation of the HSQC signal .....	84
4.4	Results .....	86
4.4.1	Simulation and verification of product operator analysis.....	86
4.5	Considerations for $^{13}\text{C}$ - $^{13}\text{C}$ distortion-free HSQC signal .....	87
4.5.1	Coherence selection by PFG to reduce $t_1$ -noise artefacts .....	87
4.5.2	Fast broadband adiabatic inversion pulse .....	90
4.5.3	A phase shift problem of the adiabatic inversion .....	90
4.5.4	Acquiring a pure phase refocusing .....	92
4.5.5	Evaluation of refocusing efficiency.....	95
4.6	Implementation of the $J$ -scaling pulse sequence.....	97
4.6.1	Product operator analysis of the $J$ -scaling sequence .....	97
4.6.2	Effect of the inversion efficiency for the $J$ -scaling .....	100
4.7	Experimental section .....	102
4.7.1	NMR measurements .....	102
4.7.2	Adiabatic pulses.....	103
4.7.3	Simulation of the HSQC signal .....	103
4.8	Results and discussion.....	104
4.8.1	Validation of the $J$ -scaling sequence .....	104
4.8.2	Comparison of signal distortion effects by adiabatic pulses .....	104
4.8.3	Acquiring of the $^{13}\text{C}$ - $^{13}\text{C}$ distortion-free HSQC signal.....	108
4.9	Conclusions .....	110
<b>5</b>	<b>Conclusion .....</b>	<b>111</b>
<b>A</b>	<b>Pulse sequence codes.....</b>	<b>114</b>

A.1	NMR pulse sequence codes for Bruker Topspin 3.6 .....	114
<b>B</b>	<b>Python processing scripts .....</b>	<b>120</b>
B.1	Processing scripts for DECODE procedure .....	120
B.2	Signal simulation scripts for $J$ -scaled HSQC .....	127
<b>C</b>	<b>Bibliography .....</b>	<b>130</b>
	국문초록 .....	144

## List of Figures

---

Figure 2.1 Pulse sequence for coherence selection PFG.....	18
Figure 3.1 Comparison of 2D NMR and its indirect covariance spectrum..	32
Figure 3.2 Pulse sequence for mHMBC .....	38
Figure 3.3 The effect of mHMBC and NUS on rotenone. ....	42
Figure 3.4 Comparison of iCov spectra of rotenone .....	44
Figure 3.5 Application of iCov spectrum for the structural assignment .....	44
Figure 3.6 An 1, <i>n</i> -ADEQUATE spectrum of rotenone.....	45
Figure 3.7 iCov-NUS-mHMBC spectrum of mixture .....	47
Figure 3.8 Comparison of 1D NMR signal and its spectral derivative.....	60
Figure 3.9 Pulse sequence for mHMBC with <i>J</i> -modulation filter.....	61
Figure 3.10 The effects of spectral merging and spectral moment filter .....	65
Figure 3.11 The effects of signal normalization and peak digitization .....	66
Figure 3.12 Results of DEOCDE.....	67
Figure 3.13 Expansions of DECODE results .....	68
Figure 3.14 NMR spectra of mixture of sucrose and quinic acid.....	69
Figure 3.15 Comparison of DECODE with/without <i>J</i> -modulation filter .....	70
Figure 3.16 DECODE results for three amino acids mixture.....	71
Figure 4.1 Origin of the signal distortion .....	80
Figure 4.2 Pulse sequence of ge-ps-PEP-HSQC .....	81

Figure 4.3 Comparison of actual HSQC and its simulated signal .....	86
Figure 4.4 Comparison of HSQC spectra with/without coherence selection by PFG.....	88
Figure 4.5 Proposed pulse sequence for HSQC using gradient pulses with coherence selection step outside of the $t_1$ -evolution period. ....	88
Figure 4.6 The relation between magnetic field vectors in rotating frames used to describe adiabatic pulses .....	92
Figure 4.7 Comparison of $^{13}\text{C}$ spectra according to the number of adiabatic inversion pulses.....	95
Figure 4.8 Pulse sequences for comparison of phase shift effects .....	96
Figure 4.9 Schematic sequence of the $J$ -scaling module .....	98
Figure 4.10 Exemplified $J$ -scaling module for two-dimensional HSQC.....	98
Figure 4.11 Comparison of HSQC signals according to $J$ -scaling factor ...	105
Figure 4.12 Comparison of HSQC signals according to pulse type and its duration.....	106
Figure 4.13 Pulse sequence of $^{13}\text{C}$ - $^{13}\text{C}$ distortion-free $F_1$ -pure in-phase $J$ -scaled HSQC .....	107
Figure 4.14 Comparison of HSQC signals using HSQC, NUS-HSQC and $J$ -scaled HSQC .....	109

## List of Abbreviations

---

<b>ADEQUATE</b>	adequate double quantum transfer experiment
<b>AIP</b>	absorptive in-phase
<b>CASE</b>	computer-assisted structure elucidation
<b>COSY</b>	correlation spectroscopy
<b>Crp</b>	chirped
<b>CTP</b>	coherence-transfer pathway
<b>DAP</b>	dispersive anti-phase
<b>DECODE</b>	deconvolution of mixed spectrum from carbon carbon correlation spectrum using enhanced demix
<b>FID</b>	free induction decay
<b>HMBC</b>	heteronuclear multiple-bond correlation
<b>HSQC</b>	heteronuclear single-quantum correlation
<b>iCov</b>	indirect covariance
<b>INADEQUATE</b>	incredible natural abundance double quantum transfer experiment
<b>INEPT</b>	insensitive nuclei enhancement by polarization transfer
<b>LPFJ</b>	low-pass <i>J</i> -filter
<b>NMR</b>	nuclear magnetic resonance

<b>NP</b>	natural products
<b>NUS</b>	non-uniform sampling
<b>PCA</b>	principal component analysis
<b>PEP</b>	preservation of equivalent pathways
<b>PFG</b>	pulse field gradient
<b>RF</b>	radio-frequency
<b>SHR</b>	State-Haberkorn-Ruben
<b>SNR</b>	signal-to-noise ratio
<b>SVD</b>	singular value decomposition
<b>TOCSY</b>	total correlation spectroscopy
<b>TPPI</b>	time-proportional phase-incrementation

---

# **Chapter 1**

## **1 Introduction**

## **$^{13}\text{C}$ - $^{13}\text{C}$ scalar coupling interaction in NMR spectroscopy**

In a structure analysis of organic compounds consisting of the carbon skeleton, the homonuclear  $^{13}\text{C}$ - $^{13}\text{C}$  scalar coupling interaction between  $^{13}\text{C}$  nuclei can give most intuitive structural information. But, their extremely low natural abundance limits their practical application for the structural analysis. In this thesis, two novel NMR acquisition and processing methods regarding to  $^{13}\text{C}$ - $^{13}\text{C}$  NMR scalar coupling interaction.

Firstly, in chapter 2, it provides a brief description of the theoretical basis of NMR used throughout this thesis. Next, in chapter 3, a spectral deconvolution method based on the mathematical operation of NMR spectrum called as covariance NMR spectroscopy which provides  $^{13}\text{C}$ - $^{13}\text{C}$  correlation spectrum from usual high-sensitivity proton detected  $^1\text{H}$ - $^{13}\text{C}$  correlation spectrum and computational processing method which is tailored to eigendecomposition operation will be discussed. In a following section at chapter 4, novel HSQC pulse sequence which is applicable for NMR based cellular metabolic analysis using  $^{13}\text{C}$ -isotope labeled compounds.

## **Mixture analysis using $^{13}\text{C}$ - $^{13}\text{C}$ correlation NMR spectroscopy**

The physical separation of mixed chemical species to obtain a pure structural information has been considered as an inevitable step. In particular, natural products (NPs), due to its complexity of structure, the structural study with a mixture NMR spectrum have been regarded impossible. In general, however, isolation and purification steps require not only laborious and time-consuming process but also gives rise to loss of chemical component itself. Thus, several approaches in order to extract individual signals from mixed spectrum have been developed based on NMR spectroscopy.<sup>1,2,3,4</sup>



It has been known that PCA analysis of NMR spectrum containing mixed chemical species can give individual spectra in forms of an eigenmode.<sup>4</sup> Previous studies, however, based on isotropic mixing between proton spins to classify same group of spins, have limitations; it is prone to result in spurious data due to degeneracy ( $^1\text{H}$ - $^1\text{H}$  TOCSY)<sup>5</sup> and only shows part of information on account of the discrete proton spin system even with hetero-nuclear correlation spectrum ( $^1\text{H}$ - $^{13}\text{C}$  HSQC-TOCSY).<sup>6</sup> This fragmentation, especially, a crucial problem in natural products which consist of several discrete proton spin systems. Instead of  $^1\text{H}$ - $^1\text{H}$  correlation information obtained from  $^1\text{H}$ - $^1\text{H}$  TOCSY spectrum, the choice of  $^{13}\text{C}$ - $^{13}\text{C}$  correlation information of individual molecules will give rise to nearly complete structural information without an ambiguity.

In this context, in chapter 3, a novel acquisition and processing method (DECODE) will be discussed. It can extract chemical shift information of individual species from the spectrum of mixed organic compounds as is. Since the DECODE method is based on HMBC spectrum, unlike previous methodology based on proton-based correlation spectroscopy, it can provide overall carbon chemical shift information including quaternary carbons. This enables an application of deconvolution method to the more complex structures even composed of several discrete proton spin systems. The virtue of DECODE is the intuitive structural information of compounds. In most cases, carbon chemical shift information of unknown compounds can be directly linked to its structure information by the comparison to spectral database. the integrity of results,  $^{13}\text{C}$ - $^{13}\text{C}$  correlation spectrum and its deconvolution spectrum, was evaluated with several model natural product compounds and resulted data allowed recovering of almost fully individual information of model compounds with moderate structural complexity and spectral overlap.

## **Distortion-free and high-resolution HSQC using $^{13}\text{C}$ -isotope**

Development of the high-field NMR spectrometer has enabled an acquiring of high-sensitivity and high-resolution NMR spectrum. However, the analysis of  $J$ -coupling information of the NMR signal in the indirect domain of the two-dimensional NMR spectrum such as real-time cell metabolites analysis, which has constraints in measurement time, remains a challenge.

On the other hands, an employing of  $^{13}\text{C}$ -isotope labeled compound for the NMR metabolomics can give unique splitting patterns and coupling constants information originated from  $^{13}\text{C}$ - $^{13}\text{C}$  coupling interaction that provide important structural information regarding the cellular metabolic process as well as increase of NMR signals such as  $^1\text{H}$ - $^{13}\text{C}$  correlation spectrum.<sup>7,8,9</sup> But it has been known that due to  $^{13}\text{C}$ - $^{13}\text{C}$  interaction undesirable signal distortions, which hamper an analysis of  $^{13}\text{C}$ - $^{13}\text{C}$  coupling information, were arisen together.<sup>10,11</sup>

In chapter 4, it will show that the development of novel HSQC method which can give distortion-free HSQC signal and selective resolution enhancement of  $J_{\text{CC}}$  splitting signals. To this end, an analytical solution of HSQC signal which gives signal distortion with  $^{13}\text{C}$ -isotope compound was provided and considerations for an introduction of  $J$ -scaling pulse sequence<sup>12,13,14</sup> increasing of  $J_{\text{CC}}$  splitting signal resolution into the HSQC pulse sequence were discussed. Finally, the feasibility of novel HSQC pulse sequence into  $^{13}\text{C}$ -isotope labeled compound was presented.

## **Chapter 2**

### **2 Theoretical basis of NMR spectroscopy**

## 2.1 Free evolution of the density operator

### 2.1.1 The wave function and the density matrix

The time-dependent Schrödinger equation for the evolution of a state function  $|\psi(t)\rangle$  is given by

$$\frac{d}{dt}|\psi(t)\rangle = -i\mathcal{H}(t)|\psi(t)\rangle$$

where  $\mathcal{H}(t)$  is the Hamiltonian of the system and the state function  $|\psi(t)\rangle = \sum_{i=1}^n c_i(t)|i\rangle$ .

The expectation value of some property,  $\langle A \rangle$ , can be written as

$$\begin{aligned}\langle A \rangle &= \int \psi^* \mathbf{A} \psi d\tau = \langle \psi | \mathbf{A} | \psi \rangle \\ &= \sum_{mn} c_m^* c_n \langle m | \mathbf{A} | n \rangle\end{aligned}$$

The products  $c_m^* c_n$  can be regarded as the elements of a matrix form of an operator  $\mathbf{P} = |\psi\rangle\langle\psi|$  defined as

$$P_{mn} = \langle n | \mathbf{P} | m \rangle = c_m^* c_n$$

Then, using the operator  $\mathbf{P}$ , the expectation value,  $\langle A \rangle$ , can be re-written as

$$\begin{aligned}\langle A \rangle &= \sum_{nm} c_n c_m^* \langle m | \mathbf{A} | n \rangle \\ &= \sum_{nm} \langle n | \mathbf{P} | m \rangle \langle m | \mathbf{A} | n \rangle = \sum_n \langle n | \mathbf{P} \mathbf{A} | n \rangle \\ &= \sum_{nm} P_{nm} A_{nm} = \sum_n (P \mathbf{A})_{nn} \\ &= \text{Tr}(\mathbf{P} \mathbf{A})\end{aligned}$$

where  $\text{Tr}()$  is the trace of a matrix.

For the mixed state, the statistical value of the expectation value is obtained by averaging over the probability distribution with a probability density,  $P(\psi)$

$$\begin{aligned}\langle \overline{A} \rangle &= \int P(\psi) \langle \psi | \mathbf{A} | \psi \rangle d\tau \\ &= \sum_{nm} \int P(\psi) c_n c_m^* d\tau \langle m | \mathbf{A} | n \rangle \\ &= \sum_{nm} \overline{c_n c_m^*} \langle m | \mathbf{A} | n \rangle\end{aligned}$$

Here, the ensemble average of coefficients,  $\overline{c_n c_m^*}$ , forms a matrix that is referred to as the *density matrix* and the density matrix is the matrix representation of an operator  $\hat{\sigma}$  referred to as the *density operator*.

$$\overline{c_n c_m^*} = \overline{\langle n | \mathbf{P} | m \rangle} = \langle n | \hat{\sigma} | m \rangle = \sigma_{nm}$$

### 2.1.2 The evolution of the density operator

The evolution of the *density operator*,  $\hat{\sigma}$ , can be expressed by following equation known as *Liouville-von Neumann* equation

$$\frac{d\hat{\sigma}(t)}{dt} = -i[\hat{H}, \hat{\sigma}(t)]$$

If the Hamiltonian is time independent, the solution is as follows

$$\hat{\sigma}(t) = \hat{U}(t) \hat{\sigma}(0) \hat{U}(t)^{-1} \text{ where } \hat{U}(t) = \exp(-i\hat{H}t)$$

## 2.2 Rotations of the density operator

### 2.2.1 Transformation of the spin density operator

The transformation of the spin density operator by RF pulse along a  $x$ -axis with field strength,  $\omega_1$ , during a delay,  $\tau$ , could be analyzed by *cyclic commutation relationships* of the angular momentum operators

$$\hat{\sigma}(\tau) = \hat{R}_x(\theta)\hat{\sigma}(0)\hat{R}_x(-\theta) ; \theta = \omega_1 \tau$$

where the rotation operator  $\hat{R}$  is

$$\hat{R}_x(\theta) = \exp(-\omega_1 \tau \hat{I}_x)$$

$$\hat{R}_y(\theta) = \exp(-\omega_1 \tau \hat{I}_y)$$

Since  $\hat{R}_x(\theta)$  is expressed by

$$\hat{R}_x(\theta) = E \cos\left(\frac{\theta}{2}\right) - 2i \hat{I}_x \sin\left(\frac{\theta}{2}\right)$$

A matrix representation of  $\hat{R}_x(\theta)$  and  $\hat{R}_x(-\theta)$  has following forms

$$\hat{R}_x(\theta) = \begin{bmatrix} \cos\left(\frac{\theta}{2}\right) & -i \sin\left(\frac{\theta}{2}\right) \\ -i \sin\left(\frac{\theta}{2}\right) & \cos\left(\frac{\theta}{2}\right) \end{bmatrix}, \quad \hat{R}_x(-\theta) = \begin{bmatrix} \cos\left(\frac{\theta}{2}\right) & i \sin\left(\frac{\theta}{2}\right) \\ i \sin\left(\frac{\theta}{2}\right) & \cos\left(\frac{\theta}{2}\right) \end{bmatrix}$$

Similar analysis of  $\hat{R}_y(\theta)$  and  $\hat{R}_y(-\theta)$  gives

$$\hat{R}_y(\theta) = \begin{bmatrix} \cos\left(\frac{\theta}{2}\right) & -\sin\left(\frac{\theta}{2}\right) \\ \sin\left(\frac{\theta}{2}\right) & \cos\left(\frac{\theta}{2}\right) \end{bmatrix}, \quad \hat{R}_y(-\theta) = \begin{bmatrix} \cos\left(\frac{\theta}{2}\right) & \sin\left(\frac{\theta}{2}\right) \\ -\sin\left(\frac{\theta}{2}\right) & \cos\left(\frac{\theta}{2}\right) \end{bmatrix}$$

For 1/2-spin, matrix representations of Cartesian spin angular momentum operators are

$$\hat{I}_x = \frac{1}{2} \begin{bmatrix} 0 & 1 \\ 1 & 0 \end{bmatrix}, \quad \hat{I}_y = \frac{1}{2} \begin{bmatrix} 0 & -i \\ i & 0 \end{bmatrix}, \quad \hat{I}_z = \frac{1}{2} \begin{bmatrix} 1 & 0 \\ 0 & -1 \end{bmatrix}$$

For example, applying a pulse of angle  $\theta$  around the  $x$  axis to  $\hat{I}_y$  gives

$$\hat{R}_x(\theta)\hat{I}_y\hat{R}_x(-\theta) = \hat{I}_y \cos(\theta) + \hat{I}_z \sin(\theta)$$

Using the *cyclic commutation relationships* of angular momentum operators, one can obtain results as below

$$\hat{I}_\alpha \hat{I}_\beta = i \hat{I}_\gamma$$

$$\hat{R}_\alpha(\theta)\hat{I}_\beta\hat{R}_\alpha(-\theta) = \hat{I}_\beta \cos(\theta) + \hat{I}_\gamma \sin(\theta)$$

$$\hat{R}_\beta(\theta)\hat{I}_\alpha\hat{R}_\beta(-\theta) = \hat{I}_\alpha \cos(\theta) - \hat{I}_\gamma \sin(\theta)$$

### 2.2.2 Effect of non-selective inversion for the bilinear operator

The effect of non-selective inversion operator,

$$\hat{R}_\gamma(\pi) \exp\{-\pi(\hat{I}_\gamma + \hat{S}_\gamma)\} \quad (\gamma = x \text{ or } y)$$

for the  $J$ -coupling operator,  $2\pi J_{IS}\hat{I}_z\hat{S}_z$ , is evaluated by

$$\begin{aligned} \hat{R}_x(\pi) 2\pi J_{IS}\hat{I}_z\hat{S}_z\hat{R}_x(-\pi) &= \exp\{-\pi(\hat{I}_x + \hat{S}_x)\} 2\pi J_{IS}\hat{I}_z\hat{S}_z \exp\{\pi(\hat{I}_x + \hat{S}_x)\} \\ &= 2\pi J_{IS} \underbrace{\exp(-\pi\hat{I}_x)\hat{I}_z \exp(\pi\hat{I}_x)}_{-\hat{I}_z} \underbrace{\exp(-\pi\hat{S}_x)\hat{S}_z \exp(\pi\hat{S}_x)}_{-\hat{S}_z} \\ &= 2\pi J_{IS}(-\hat{I}_z)(-\hat{S}_z) \\ &= 2\pi J_{IS}\hat{I}_z\hat{S}_z \end{aligned}$$

## 2.3 Evolution of the Cartesian operator

### 2.3.1 Free precession

Under the chemical shift Hamiltonian,  $\hat{H} = \Omega_I \hat{I}_z$ , an evolution of the product operator during a delay,  $t$ , is expressed by has the form,

$$\begin{aligned}\hat{I}_x &\xrightarrow{\Omega_I \hat{I}_z} \hat{I}_x \cos(\Omega_I t_1) + \hat{I}_y \sin(\Omega_I t_1) \\ \hat{I}_y &\xrightarrow{\Omega_I \hat{I}_z} \hat{I}_y \cos(\Omega_I t_1) - \hat{I}_x \sin(\Omega_I t_1) \\ \hat{I}_z &\xrightarrow{\Omega_I \hat{I}_z} \hat{I}_z\end{aligned}$$

For a weakly coupled two spins,  $I$  and  $S$ , with the where  $J_{IS}$  is the  $J$ -coupling constant. Under the  $J$ -coupling Hamiltonian,  $\hat{H} = 2\pi J_{IS} \hat{I}_z \hat{S}_z$ , an evolution of the Cartesian operator during delay,  $t$ , is expressed by

$$\begin{aligned}\hat{I}_x &\xrightarrow{2\pi J_{IS} \hat{I}_z \hat{S}_z t} \hat{I}_x \cos(\pi J_{IS} t) + 2\hat{I}_y \hat{S}_z \sin(\pi J_{IS} t) \\ \hat{I}_y &\xrightarrow{2\pi J_{IS} \hat{I}_z \hat{S}_z t} \hat{I}_y \cos(\pi J_{IS} t) - 2\hat{I}_x \hat{S}_z \sin(\pi J_{IS} t) \\ \hat{I}_z &\xrightarrow{2\pi J_{IS} \hat{I}_z \hat{S}_z t} \hat{I}_z \\ 2\hat{I}_x \hat{S}_z &\xrightarrow{2\pi J_{IS} \hat{I}_z \hat{S}_z t} 2\hat{I}_x \hat{S}_z \cos(\pi J_{IS} t) + \hat{I}_y \sin(\pi J_{IS} t) \\ 2\hat{I}_y \hat{S}_z &\xrightarrow{2\pi J_{IS} \hat{I}_z \hat{S}_z t} 2\hat{I}_y \hat{S}_z \cos(\pi J_{IS} t) - \hat{I}_x \sin(\pi J_{IS} t)\end{aligned}$$

### 2.3.2 Chemical shift and $J$ -coupling evolution of the density operator

Evolution of the density operator with a time independent Hamiltonian,  $\hat{H}_0$ , in a rotating frame during  $t$  has a form

$$\hat{\rho}(t) = \exp(-i\hat{H}_0 t) \hat{\sigma}(0) \exp(i\hat{H}_0 t)$$

$$\text{where } \hat{H}_0 = \hat{H}_1 + \hat{H}_2; \quad \hat{H}_1 = \Omega_1 \hat{I}_z + \Omega_2 \hat{S}_z \quad \text{and} \quad \hat{H}_2 = 2\pi J_{IS} \hat{I}_z \hat{S}_z$$



Here  $\hat{H}_1$  is a Zeeman interaction (chemical shift) Hamiltonian in a rotating frame and  $\hat{H}_2$  is a  $J$ -coupling Hamiltonian of two weakly coupled spin  $I$  and  $S$ .

Since two Hamiltonian operators  $\hat{H}_1$  and  $\hat{H}_2$  are commute, the evolution of the density operator can be expressed as follows,

$$\hat{\rho}(t) = \exp(-i\hat{H}_2 t) \underbrace{\exp(-i\hat{H}_1 t) \hat{\sigma}(0) \exp(i\hat{H}_1 t)}_{\hat{\rho}(t_1)} \exp(i\hat{H}_2 t)$$

Assuming the density operator has a form of  $\hat{I}_x$ , after free precession with  $\hat{H}_1$

$$\begin{aligned} \hat{\sigma}(t_1) &= \exp(-i\hat{H}_1 t) \hat{I}_x \exp(i\hat{H}_1 t) \\ &= \exp\{-i(\Omega_I \hat{I}_z + \Omega_S \hat{S}_z)t\} \hat{I}_x \exp\{-i(\Omega_I \hat{I}_z + \Omega_S \hat{S}_z)t\} \\ &= \exp\{-i\Omega_I \hat{I}_z t\} \hat{I}_{1x} \exp\{i\Omega_I \hat{I}_z t\} \underbrace{\exp\{-i\Omega_S \hat{S}_z t\} \exp\{-i\Omega_S \hat{S}_z t\}}_E \\ &= \hat{I}_x \cos(\Omega_I t) + \hat{I}_y \sin(\Omega_I t) \end{aligned}$$

Then,  $J$ -coupling evolution of the density operator with  $\hat{H}_2$  gives

$$\begin{aligned} \hat{\sigma}(t) &= \exp(-i\hat{H}_2 t) \hat{\rho}(t_1) \exp(i\hat{H}_2 t) \\ &= \exp(-i\hat{H}_2 t) \hat{I}_x \cos(\Omega_I t) \exp(i\hat{H}_2 t) + \exp(-i\hat{H}_2 t) \hat{I}_y \sin(\Omega_I t) \exp(i\hat{H}_2 t) \\ &= \exp(-i2\pi J_{IS} \hat{I}_z \hat{S}_z t) \hat{I}_x \cos(\Omega_I t) \exp(i2\pi J_{IS} \hat{I}_z \hat{S}_z t) \\ &\quad + \exp(-i2\pi J_{IS} \hat{I}_z \hat{S}_z t) \hat{I}_y \sin(\Omega_I t) \exp(i2\pi J_{IS} \hat{I}_z \hat{S}_z t) \\ &= \cos(\Omega_I t) \{ \hat{I}_x \cos(\pi J_{IS} t) + 2\hat{I}_y \sin(2\pi J_{IS} \hat{S}_z t) \} \\ &\quad + \sin(\Omega_I t) \{ \hat{I}_y \cos(\pi J_{IS} t) - 2\hat{I}_x \sin(2\pi J_{IS} \hat{S}_z t) \} \\ &= \hat{I}_x \cos(\Omega_I t) \cos(\pi J_{IS} t) + 2\hat{I}_y \hat{S}_z \cos(\Omega_I t) \sin(\pi J_{IS} t) + \hat{I}_y \sin(\Omega_I t) \cos(\pi J_{IS} t) \\ &\quad - 2\hat{I}_x \hat{S}_z \sin(\Omega_I t) \sin(\pi J_{IS} t) \end{aligned}$$

### 2.3.3 Spin-echo pulse sequence

Let us consider weakly coupled two spin system with a Hamiltonian in the rotating frame reference

$$\hat{H}_0 = \hat{H}_1 + \hat{H}_2; \quad \hat{H}_1 = \Omega_1 \hat{I}_z + \Omega_2 \hat{S}_z \quad \text{and} \quad \hat{H}_2 = 2\pi J_{IS} \hat{I}_z \hat{S}_z$$

After a free evolution during  $\tau_1$ , if one applying a pulse of angle  $\pi$  around the  $x$  axis followed by free evolution during  $\tau_2$ , the total evolution of density operator is described by

$$\begin{aligned} \hat{\sigma}(\tau_1 + \tau_2) &= \exp(-i\hat{H}_0\tau_2) \hat{R}_x(\pi) \exp(-i\hat{H}_0\tau_1) \hat{\sigma}(0) \exp(i\hat{H}_0\tau_1) \hat{R}_x(-\pi) \exp(i\hat{H}_0\tau_2) \\ &= \exp\{-i(\hat{H}_1 + \hat{H}_2)\tau_2\} \hat{R}_x(\pi) \exp\{-i(\hat{H}_1 + \hat{H}_2)\tau_1\} \hat{R}_x(-\pi) \hat{R}_x(\pi) \\ &\quad \times \hat{\sigma}(0) \hat{R}_x(-\pi) \hat{R}_x(\pi) \exp\{i(\hat{H}_1 + \hat{H}_2)\tau_1\} \hat{R}_x(-\pi) \exp\{i(\hat{H}_1 + \hat{H}_2)\tau_2\} \\ &= \exp(-i\hat{H}_2\tau_2) \exp(-i\hat{H}_1\tau_2) \hat{R}_x(\pi) \exp(-i\hat{H}_1\tau_1) \\ &\quad \times \hat{R}_x(-\pi) \hat{R}_x(\pi) \exp(-i\hat{H}_2\tau_1) \hat{R}_x(-\pi) \hat{\sigma}(0) \hat{R}_x(\pi) \exp(i\hat{H}_1\tau_1) \\ &\quad \times \hat{R}_x(-\pi) \hat{R}_x(\pi) \exp(i\hat{H}_2\tau_1) \hat{R}_x(-\pi) \exp(i\hat{H}_1\tau_2) \exp(i\hat{H}_2\tau_2) \\ &= \exp\{-i\hat{H}_2(\tau_2 + \tau_1)\} \exp\{-i\hat{H}_1(\tau_2 - \tau_1)\} \hat{R}_x(\pi) \hat{\sigma}(0) \\ &\quad \times \hat{R}_x(-\pi) \exp\{i\hat{H}_1(\tau_2 - \tau_1)\} \exp\{i\hat{H}_2(\tau_2 + \tau_1)\} \\ &= \hat{R}_x(\pi) \exp\{-i\hat{H}_2(\tau_2 + \tau_1)\} \exp\{-i\hat{H}_1(\tau_2 - \tau_1)\} \hat{\sigma}(0) \\ &\quad \times \exp\{i\hat{H}_1(\tau_2 - \tau_1)\} \exp\{i\hat{H}_2(\tau_2 + \tau_1)\} \hat{R}_x(-\pi) \end{aligned}$$

Assuming,  $\hat{\sigma}(0) = \hat{I}_x$  then,

$$\begin{aligned} \hat{\sigma}(\tau_1 + \tau_2) &= \hat{I}_x \cos\{\Omega_I(\tau_2 - \tau_1)\} \cos\{\pi J_{IS}(\tau_2 + \tau_1)\} \\ &\quad + 2\hat{I}_y \hat{S}_z \cos\{\Omega_I(\tau_2 - \tau_1)\} \sin\{\pi J_{IS}(\tau_2 + \tau_1)\} \\ &\quad - \hat{I}_y \sin\{\Omega_I(\tau_2 - \tau_1)\} \cos\{\pi J_{IS}(\tau_2 + \tau_1)\} \\ &\quad + 2\hat{I}_x \hat{S}_z \sin\{\Omega_I(\tau_2 - \tau_1)\} \sin\{\pi J_{IS}(\tau_2 + \tau_1)\} \end{aligned}$$

$$\text{If } \tau_1 = \tau_2, \quad \hat{\sigma}(2\tau_1) = \hat{I}_x \cos\{\pi J_{IS}(2\tau_1)\} + 2\hat{I}_y \hat{S}_z \sin\{\pi J_{IS}(2\tau_1)\}$$

## 2.4 Frequency discrimination and lineshape in 2D NMR

### 2.4.1 Properties of the indirect domain signal in 2D NMR

In the two-dimensional NMR the modulation in the  $t_1$  domain is cosine or sine modulated<sup>15</sup>. Consider a cosine modulated signal,  $\cos(\Omega t_1)$ , in the  $t_1$  domain. Then, we obtain a two-dimensional signal

$$S(t_1, t_2) = \cos(\Omega_1 t_1) \exp(i \Omega_2 t_2) \exp(-R_2^1 t_1) \exp(-R_2^2 t_2)$$

Using a property,

$$\cos(\Omega_1 t_1) = \frac{1}{2} \{ \exp(i \Omega_1 t_1) + \exp(-i \Omega_1 t_1) \}$$

Then,

$$\begin{aligned} S(t_1, t_2) = \frac{1}{2} \{ \exp(i \Omega_1 t_1) \exp(i \Omega_2 t_2) + \exp(-i \Omega_1 t_1) \exp(i \Omega_2 t_2) \} \\ \times \exp(-R_2^1 t_1) \exp(-R_2^2 t_2) \end{aligned}$$

A complex Fourier transformation of complex time-domain signal gives spectrum consist of real and imaginary frequency-domain signals

$$\begin{aligned} S(\omega) = \mathcal{F} \{ S(t) \} &= \int_{-\infty}^{\infty} \exp(i \omega_0 t) \exp(-i \omega t) \exp(Rt) dt \\ &= \underbrace{\frac{R}{(\omega_0 - \omega)^2 + R^2}}_{Real} - i \underbrace{\frac{(\omega_0 - \omega)}{(\omega_0 - \omega)^2 + R^2}}_{Imaginary} \end{aligned}$$

The real part of the spectrum is a peak with absorption mode *Lorentzian lineshape*,  $A(\omega)$ , whereas the imaginary part gives rise to dispersive *Lorentzian lineshape*,  $D(\omega)$ .

Therefore, after Fourier transformation along the both time domain, the frequency-domain signal is

$$S(\omega_1, \omega_2) = \frac{1}{2} \{ A(\Omega_1) + iD(\Omega_1) + A(-\Omega_1) + iD(-\Omega_1) \} \{ A(\Omega_2) + iD(\Omega_2) \}$$

$$\begin{aligned}
 &= \frac{1}{2} (A(\Omega_1)A(\Omega_2) + iA(\Omega_1)D(\Omega_2) + iD(\Omega_1)A(\Omega_2) - D(\Omega_1)D(\Omega_2)) \\
 &= +\frac{1}{2} (A(-\Omega_1)A(\Omega_2) + iA(-\Omega_1)D(\Omega_2) + iD(-\Omega_1)A(\Omega_2) - D(-\Omega_1)D(\Omega_2)) \\
 &= \frac{1}{2} \underbrace{(A(\Omega_1)A(\Omega_2) - D(\Omega_1)D(\Omega_2))}_{\text{Real } (\Omega_1, \Omega_2)} + i \underbrace{(A(\Omega_1)D(\Omega_2) + (\Omega_1)A(\Omega_2))}_{\text{Imaginary } (\Omega_1, \Omega_2)} \\
 &= +\frac{1}{2} \underbrace{(A(-\Omega_1)A(\Omega_2) - D(-\Omega_1)D(\Omega_2))}_{\text{Real } (-\Omega_1, \Omega_2)} + i \underbrace{(A(-\Omega_1)D(\Omega_2) + (-\Omega_1)A(\Omega_2))}_{\text{Imaginary } (-\Omega_1, \Omega_2)}
 \end{aligned}$$

Thus, cosine or sine modulation of two-dimensional NMR signal with respect to  $t_1$  will not only lead to lack the frequency discrimination in the  $F_1$  domain but give a phase-twist lineshapes in the resulted two-dimensional spectrum.

## 2.4.2 The States-Haberkorn-Ruben (SHR) method

The principle of hypercomplex method or SHR method<sup>16</sup> is as follows

Consider the cosine modulated two-dimensional NMR signal,  $S_c(t_1, t_2)$ ,

$$S_c(t_1, t_2) = \cos(\Omega_1 t_1) \exp(i \Omega_2 t_2) \exp(-R_2^1 t_1) \exp(-R_2^2 t_2)$$

Using the previous notation, Fourier transformation of signal with respect to  $t_2$ ,

$$S_c(t_1, \Omega_2) = \cos(\Omega_1 t_1) \exp(-R_2^1 t_1) \{A(\Omega_2) + iD(\Omega_2)\}$$

Discarding the imaginary part of the signal gives

$$S_{c, \text{Re}}(t_1, \Omega_2) = \cos(\Omega_1 t_1) \exp(-R_2^1 t_1) A(\Omega_2)$$

Again, same process could be applied for sine modulated signal

$$S_{s, \text{Re}}(t_1, \Omega_2) = \sin(\Omega_1 t_1) \exp(-R_2^1 t_1) A(\Omega_2)$$

Combining the real part of the cosine and sine modulated signals forms a new signal form  $S_{\text{SHR}}(t_1, \Omega_2)$

$$\begin{aligned}
 S_{\text{SHR}}(t_1, \Omega_2) &= S_{\text{c,Re}}(t_1, \Omega_2) + i S_{\text{s,Re}}(t_1, \Omega_2) \\
 &= \underbrace{\{\cos(\Omega_1 t_1) + i \sin(\Omega_1 t_1)\}}_{\exp(i\Omega_1 t_1)} \exp(-R_2^1 t_1) A(\Omega_2) \\
 &= \exp(i\Omega_1 t_1) \exp(-R_2^1 t_1) A(\Omega_2)
 \end{aligned}$$

Finally, Fourier transformation of  $S_{\text{SHR}}(t_1, \Omega_2)$  along the  $t_1$  gives

$$\begin{aligned}
 S_{\text{SHR}}(\Omega_1, \Omega_2) &= \{A(\Omega_1) + i D(\Omega_1)\} A(\Omega_2) \\
 &= A(\Omega_1) A(\Omega_2) + i D(\Omega_1) A(\Omega_2)
 \end{aligned}$$

And the real part of the  $S_{\text{SHR}}(\Omega_1, \Omega_2)$  provide a doubly absorptive lineshape,  $A(\Omega_1) A(\Omega_2)$ .

### 2.4.3 Time-Proportional Phase-Incrementation (TPPI) method

The principle of TPPI method<sup>17</sup> is as follows

Let us consider a cosine modulated signal of which phase shifted signal by  $\phi = \omega_{\text{add}} t_1$

$$S(\phi, t_1, t_2) = \cos(\Omega_1 t_1 + \phi) \exp(i \Omega_2 t_2) \exp(-R_2^1 t_1) \exp(-R_2^2 t_2)$$

If re-write the  $\phi$  as an  $\omega_{\text{add}} t_1$

$$S(\omega_{\text{add}}, t_1, t_2) = \cos\{(\Omega_1 + \omega_{\text{add}}) t_1\} \exp(i \Omega_2 t_2) \exp(-R_2^1 t_1) \exp(-R_2^2 t_2)$$

In the two-dimension NMR acquisition, the signal in  $t_1$  is recoded at evenly spaced in  $\Delta_1$ , where  $\Delta_1$  is the  $\frac{1}{2f_{\text{max}}}$  in second.

$$S(\phi, n\Delta, t_2) = \cos\{(\Omega_1 + \omega_{\text{add}}) n\Delta_1\} \exp(i \Omega_2 t_2) \exp(-R_2^1 n\Delta_1) \exp(-R_2^2 t_2)$$

By adding  $f_{\text{max}}$  Hz to the  $\Omega_1$ , all of offsets are changed to positive and a maximum frequency  $f_{\text{max}}$  and an interval  $\Delta_1 \left(= \frac{1}{2f_{\text{max}}}\right)$  are also changed to  $2f_{\text{max}}$  and  $\Delta'_1 \left(= \frac{1}{4f_{\text{max}}}\right)$  respectively.

$$S(n\Delta', t_2) = \cos \left\{ (\Omega_1 + 2\pi f_{max}) \frac{n}{4f_{max}} \right\} \exp(i\Omega_2 t_2) \exp(-R_2^1 n\Delta') \exp(-R_2^2 t_2)$$

$$S(n\Delta, t_2) = \cos \left( \Omega_1 n\Delta' + \frac{n\pi}{2} \right) \exp(i\Omega_2 t_2) \exp(-R_2^1 n\Delta') \exp(-R_2^2 t_2)$$

Therefore, incrementing the phase of the cosine modulated signal by  $\frac{\pi}{2}$  results in frequency discrimination in the  $F_1$  domain

$$\begin{aligned} S_{\text{TPPI}}(\Omega_1, \Omega_2) &= \frac{1}{2} \left\{ A(\Omega_1) + iD(\Omega_1) + \underbrace{A(-\Omega_1) + iD(-\Omega_1)}_{\text{discard}} \right\} A(\Omega_2) \\ &= \frac{1}{2} \{ A(\Omega_1)A(\Omega_2) + iD(\Omega_1)A(\Omega_2) \} \end{aligned}$$

In the same manner, the real part of the  $S_{\text{TPPI}}(\Omega_1, \Omega_2)$  provide a doubly absorptive lineshape,  $\frac{1}{2} A(\Omega_1)A(\Omega_2)$ .

## 2.5 Coherence selection by PFG

In modern NMR spectroscopy, there are two methods in which this selection of required signals is achieved. The *phase cycling*<sup>18,19</sup> procedure, firstly, selectively retains only the desirable signal through the accumulation of free construction decays resulted from the changing of the RF pulse for each experiment, and cancels out the unwanted signals. The second procedure employs *field gradient pulse*<sup>20,21</sup>. With a short-duration field gradient pulse which result in a field inhomogeneity, any coherences present will be de-phased. By a careful choice of the subsequent gradient pulses, however, within a pulse sequence one can ensure that refocusing of only the desired coherences.

### 2.5.1 Magnetic field gradient

If a field gradient,  $G$ , is applied to the magnetic field,  $B_0$  then,

$$B_z = B_0 + G_z$$

where  $G$  is the magnetic field gradient, in units  $\text{Tm}^{-1}$ , and  $z$  is the coordinate along the field direction, measured (in unit cm) from the centre of the sample.

For a nucleus with the gyromagnetic ratio,  $\gamma$ , the *Larmor frequency* can be described as

$$-\gamma B_z = -\gamma B_0 - \gamma G_z$$

$$\Omega_z = \Omega_0 - \gamma G_z$$

### 2.5.2 Phase evolution of the coherence in magnetic field gradient

Considering the only spatially dependent part,  $\Omega(z)$ , the evolution of the lowering operator (coherence order -1,  $\hat{I}_-$ ) with  $\Omega(z)$  during  $t$  is as follows

$$\hat{I}_- \xrightarrow{\Omega(z)\hat{I}_z} \exp(i\Omega(z)t)\hat{I}_-$$

For the multiple quantum coherence, for example  $\hat{I}_{1-}\hat{I}_{2-}$ ; double quantum coherence operator, the evolution spatially dependent part,  $\Omega(z)$ , during  $t$  is

$$\hat{I}_{1-}\hat{I}_{2-} \xrightarrow{\Omega(z)(\hat{I}_{1z}+\hat{I}_{2z})} \exp(2i\Omega(z)t)\hat{I}_{1-}\hat{I}_{2-}$$

The generalized expression of an acquired phase in the spatially dependent part,  $\phi(z)$ , for the coherence order  $p$  due to field gradient,  $G_z$  during  $t$  is

$$\phi(z) = -p \times \gamma G_z t$$

### 2.5.3 Acquiring a spatially dependent phase by the PFG

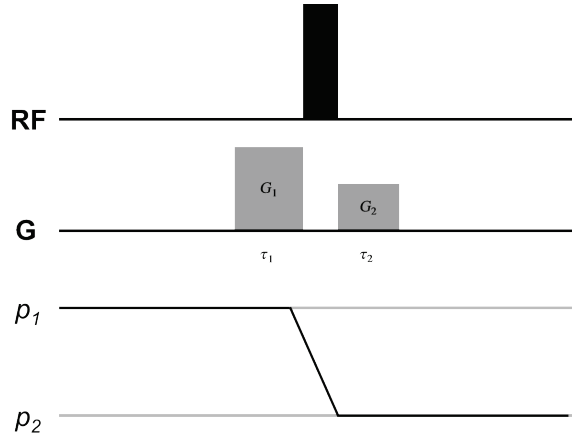


**Figure 2.1** Pulse sequence for coherence selection PFG

Black-wide bar indicates  $\pi$ -inversion pulse.  $G_1$  and  $G_2$  denotes strength of gradient pulse along the z-axis.  $\tau_1$  and  $\tau_2$  means duration of gradient pulse  $G_1$  and  $G_2$  respectively.  $p_1$  and  $p_2$  denote coherence order of the polarization.



The acquired phase  $\phi_1(z)$  of a  $p_1$ -order coherence during the first field gradient pulse  $G_1$  during  $\tau_1$  is

$$\phi_1(z) = -p_1\gamma G_1\tau_1$$

After applying RF, the acquired phase of  $p_2$ -order coherence during the second field gradient pulse  $G_2$  during  $\tau_2$  is

$$\phi_2(z) = -p_2\gamma G_2\tau_2$$

Therefore, final acquired spatially dependent phase is

$$\phi_{1+2}(z) = -p_1\gamma G_1\tau_1 - p_2\gamma G_2\tau_2$$

#### 2.5.4 Dephasing by the field gradient

Consider  $-1$ -quantum coherence operator with the spatially dependent phase factor,  $\phi = \gamma G_z t$

$$\exp(i\gamma G_z t) \hat{I}_-$$

One can evaluate the intensity of residual observable signals by simply adding up the acquired phase,  $\exp(i\gamma G_z t)$ , in along the  $z$ -axis in a detection range,  $L$ .

$$\begin{aligned} S_{\text{obs}}(t) &= \frac{1}{L} \int_{-\frac{1}{2}L}^{+\frac{1}{2}L} \exp(i\gamma G_z t) dz \\ &= \frac{\sin\left(\frac{1}{2}\gamma G_z L t\right)}{\frac{1}{2}\gamma G_z L t} = \frac{\sin x}{x} = \text{sinc}(x), \quad \text{where } x = \frac{1}{2}\gamma G_z L t \end{aligned}$$

$S_{\text{obs}}(t)$  has a form of the *sinc* function decayed over the time  $t$ .

For the proton nucleus, if  $G_z = 20 \text{ G cm}^{-1}$  and  $L = 1 \text{ cm}$ , then  $S_{\text{obs}}(t) = \frac{3.7 \times 10^{-6}}{t}$ .

At  $t = 0.37 \text{ ms}$ ,  $S_{\text{obs}}(t) \approx 0.01$

### 2.5.5 Selection of P-type and N-type spectra by the PFG

The P-type or anti-echo spectrum refers to its coherence order in  $t_1$  is of same sign to that in  $t_2$  whereas the N-type or echo spectrum is of opposite sign to that. Since the  $M_+ = \gamma I_+$  is the only observable magnetization and the expectation value of certain operator is defined as

$$\langle M_+ \rangle(t) = \text{Tr} \{ M_+ \hat{\sigma}(t) \} \text{ where } \hat{\sigma} \text{ is the density operator.}$$

Thus, the only observable density operator has  $-1$ -coherence order, thereby P-type spectrum has  $-1$ -coherence order and N-type spectrum has  $+1$ -coherence order in  $t_1$  respectively.

Let us consider, a Cartesian spin operator,  $-\hat{I}_y$ . Using an identity,  $\hat{I}_y = \frac{1}{2}(\hat{I}_+ - \hat{I}_-)$ , after a free evolution during  $t_1$  followed by applying the pulsed field gradient,  $G_a$  during  $\tau_z$  gives,

$$-\frac{1}{2}(\hat{I}_+ - \hat{I}_-) \xrightarrow{\Omega I_z t_1} \xrightarrow{\Omega I_z \tau_z + \gamma G_a \tau_z} -\frac{1}{2} [\exp\{-i(\Omega t_1 + \gamma G_a \tau_z)\} \hat{I}_+ - \exp\{i(\Omega t_1 + \gamma G_a \tau_z)\} \hat{I}_-]$$

Since an inversion pulse simply reverse the sign of the coherence order, after the  $\pi$ -pulse rotation along the  $x$ -axis the operator has a form,

$$-\frac{1}{2} [\exp\{-i(\Omega t_1 + \Omega \tau_z + \gamma G_a \tau_z)\} \hat{I}_+ \exp\{i(\Omega t_1 + \Omega \tau_z + \gamma G_a \tau_z)\} \hat{I}_-] \\ \xrightarrow{\pi \hat{I}_x} -\frac{1}{2} [\exp\{-i(\Omega t_1 + \Omega \tau_z + \gamma G_a \tau_z)\} \hat{I}_- - \exp\{i(\Omega t_1 + \Omega \tau_z + \gamma G_a \tau_z)\} \hat{I}_+]$$

Then, after applying the second pulse field gradient,  $G_a$  during  $\tau_z$ , followed by the free evolution during  $t_2$ , the observable density operator has a form of

$$-\frac{1}{2} [\exp\{-i(\Omega t_1 + \Omega \tau_z + \gamma G_a \tau_z)\} \hat{I}_-] \xrightarrow{\Omega I_z \tau_z + \gamma G_a \tau_z} -\frac{1}{2} \{ \exp(-i\Omega t_1) \hat{I}_- \} \\ \xrightarrow{\Omega I_z t_2} -\frac{1}{2} \{ \exp(-i\Omega t_1) \exp(i\Omega t_2) \hat{I}_- \}$$

$$\begin{aligned}
 S_{\text{obs}}(t_1, t_2) &= -\frac{1}{2} \{ \exp(-i\Omega t_1) \exp(i\Omega t_2) \} \underbrace{\text{Tr}(\hat{I}_+ \hat{I}_-)}_1 \\
 &= -\frac{1}{2} \{ \exp(-i\Omega t_1) \exp(i\Omega t_2) \}
 \end{aligned}$$

The resulted operator which has an opposite sign of coherence order is the N-*type* or echo spectrum in the two-dimensional NMR acquisition scheme.

Conversely, omitting of rotation or  $2k\pi$ -rotation along the  $x$ -axis give the P-*type* spectrum.

## 2.6 Adiabatic fast passage

A spin-inversion is important element in modern NMR experiment. For the spin-inversion, in lieu of applying the radio-frequency pulse, an adiabatic inversion has been employed for spin-inversion of nuclei which has a wide-range of chemical shift such as  $^{13}\text{C}$  nucleus<sup>22,23,24,25,26,27</sup>.

### 2.6.1 Adiabatic condition

If one sweeping a continuous radio-frequency field  $B_1$  through resonance, from positive offset to negative offset, then the effective field  $B_{\text{eff}}$  moves along the arc in the  $xz$ -plane from  $z$ -axis to  $-z$ -axis.

Let us consider a magnetization aligned with  $z$ -axis. Since the spin only undergoes  $B_{\text{eff}}$ , at equilibrium the spin aligned with  $B_{\text{eff}}$ . When an adiabatic condition is satisfied, the spin continuously aligned with  $B_{\text{eff}}$  in spite of the  $B_1$  field sweeping

Adiabatic condition is defined as<sup>19</sup>

$$\left| \frac{d\theta}{dt} \right| \ll \omega_{\text{eff}} = \gamma B_{\text{eff}}$$

where  $B_{\text{eff}}$  is an effective field,  $\omega_{\text{eff}}$  is the *effective larmor frequency* and  $\theta$  is an inclination of  $B_{\text{eff}}$  with respect to the  $x$ -axis. If the sweep rate is fast enough to compare with  $T_1$  and  $T_2$  time of the spin (Adiabatic fast passage), then a complete spin inversion could be obtained.

One can define the adiabatic condition as an adiabaticity factor  $Q$

$$Q = \frac{\omega_{\text{eff}}}{\left| \frac{d\theta}{dt} \right|}$$

### **2.6.2 Pros of the adiabatic fast passage**

The spin-inversion by the adiabatic fast passage has an advantage respect to RF-pulse. It can achieve a wideband spin-inversion effectively with a limited  $B_1$  field strength. Thus, it is especially useful for nuclei with a wide-range of the chemical shift at modern high-field NMR spectrometer. Furthermore, since the adiabatic pulses can tolerate a wide-range of  $B_1$ , it is quite insensitive to spatial inhomogeneity<sup>25,28,29,30,31,32,33,34,35,36</sup> in  $B_1$  or  $B_0$ . It is widely used in broadband decoupling pulse sequence.

### **2.6.3 Cons of the adiabatic fast passage**

Although the adiabatic fast passage can invert wide-range of bandwidth and has higher tolerance to the field inhomogeneity than even compare to best composite pulses, it requires much more duration (milliseconds) to perform than simple rectangular pulse or composite pulses. Thus, during the relatively long adiabatic passage, the coherence of spins which has very short  $T_2$  times, could be attenuated severely. In addition, the adiabatic passage inverts spins of different chemical shift values at different time, it gives rise to cumulative phase errors in case of plane rotations of magnetization (i.e. the spin-echo pulse sequence of transverse magnetization)<sup>26,27</sup>.

## **Chapter 3**

### **3 DECODE procedure for spectral deconvolution**

### 3.1 Introduction

NMR has been widely used in studying molecular structures of organic compounds. Thus, various pulse sequences have been developed for structure elucidation of small molecules so far<sup>37,38,39,40,41,42,43,44</sup>. Among those, the spectrum which has a direct correlation information of  $^{13}\text{C}$ - $^{13}\text{C}$  connectivity may be the most useful and intuitive type of spectrum for structure analysis of organic compounds; Such as  $^{13}\text{C}$ - $^{13}\text{C}$  COSY<sup>45</sup>,  $^{13}\text{C}$ - $^{13}\text{C}$  TOCSY<sup>46</sup> or INADEQUATE<sup>47</sup>. But, this is inherently not possible, in general, on account of the low natural abundance (0.01%) of NMR-active  $^{13}\text{C}$  nucleus. Therefore, it has been required a great deal of effort to elucidation of the structures of complex natural products (NP). Currently, proton-detected experiments, such as  $^1\text{H}$ - $^{13}\text{C}$  HMBC<sup>48</sup>, are mostly employed in the  $^{13}\text{C}$  information as an indirect manner. However, some inefficiencies of the pulse sequence, heterogeneous  $J_{\text{CH}}$  values<sup>49</sup>, and the poor resolution of indirect domain ( $F_1$ ) in HMBC deteriorate a quality of the spectrum. Furthermore, less intuitive type of information comparing to correlation spectroscopy (COSY) or total-correlation spectroscopy (TOCSY)<sup>5</sup> have been difficulties for interpretation of the HMBC spectrum. Alternatively, indirect covariance (iCov) operation on  $^1\text{H}$ - $^{13}\text{C}$  HSQC-TOCSY<sup>50</sup> has been proposed to yield a synthetic direct  $^{13}\text{C}$ - $^{13}\text{C}$  correlation spectrum. However, the inherent problems of proton TOCSY have limited its application to molecules with a single proton spin system without quaternary carbons. iCov operation on HMBC also has been proposed<sup>51</sup>, but the above-noted problems of HMBC are all inherited, and, therefore, its use is currently impractical for complex NP molecules.

Another important issue in NMR analysis is related to the difficulty in obtaining a purely single compound. As NMR signals, in principle, reflect all spins in sample simultaneously, undesired or unexpected impurities also present resulted spectrum.

Thus, in case of spectra even more than two-dimension also suffer a signal overlap problem which interferes extracting true information of chemical species. Therefore, to obtain an unambiguous structural information with NMR spectra a physical purification process prior to analysis has been regarded as an inevitable step. Often, however, an isolation and purification process require not only laborious and time-consuming process but also gives rise to loss of chemical component itself. Several approaches, hence, to extract individual signals from mixed spectrum as is, have been considered<sup>1,2,3,4</sup>. Commonly, previous studies have exploited a proton *J*-coupling network of a mixed  $^1\text{H}$ - $^1\text{H}$  TOCSY or  $^1\text{H}$ - $^{13}\text{C}$  HSQC-TOCSY spectra to classify same group of spins, but have several limitations; it is prone to result in spurious data due to a signal overlap ( $^1\text{H}$ - $^1\text{H}$  TOCSY) and only shows part of information on account of lack of quaternary carbon information even in  $^1\text{H}$ - $^{13}\text{C}$  HSQC-TOCSY spectrum. This fragmented spin information, especially, is a crucial problem in NPs which in general consist of several discrete proton spin systems. In case of the structure elucidation of NPs, furthermore, possessing a high-structure complexity, it requires information of chemical shift and correlation with high-fidelity than an ordinary metabolite analysis. However, if one switches point of view characterizing a single chemical species from between proton spins correlation to proton and carbon spin correlation many problems can be solved. In most of organic compounds, the information inherent in type of HMBC spectrum can be translated into nearly complete  $^{13}\text{C}$ - $^{13}\text{C}$  correlation the cluster of  $^{13}\text{C}$  signals of single chemical species regardless of fractional proton spin systems.

Hence, through choosing a proper deconvolution method one can expect an extraction of overall carbon spin information of individual species from the mixed spectrum. This is because of spectral features of HMBC correlations which provides  $^1\text{H}$ - $^{13}\text{C}$  correlations including the quaternary carbon which is never appeared other type of spectrum (e.g., TOCSY, HSQC-TOCSY). In a carbon dimension,



furthermore, its wider spectral range than a proton can take advantage in terms of spectral resolution. Thereby, one can reasoned that new approaches might be built on the old HMBC principle. The remained problem is from the HMBC-type spectrum how can we construct the reliable  $^{13}\text{C}$ - $^{13}\text{C}$  correlation close to true  $^{13}\text{C}$ - $^{13}\text{C}$  correlation map and extract carbon information of individual compound avoiding an interference between heterogeneous species. In this study, an approach involving non-uniform sampling (NUS)<sup>52,53,54,55,56,57,58,59,60,61</sup> and novel signal processing along with iCov-eigendecomposition to address two important issues in NMR structure analysis will be discussed.

## 3.2 Theoretical and experimental backgrounds in DECODE

### 3.2.1 Covariance NMR Spectroscopy

One of the major constraints in the two-dimensional NMR spectroscopy is a multiple repetition of same pulse sequence, with a series of constant time increment  $t_1$ . Because the total experiment time of the two-dimensional NMR is proportional to the repetition number,  $N_1$ , which affects the spectral resolution of the indirect  $t_1$  domain signal,  $N_1$  is typically smaller than actual sampling points in the time domain  $t_2$  and it gives rise to a poor-resolution of  $t_1$  domain signal than the  $t_2$  time-domain signal. In 2004, brüschweiler *et al.*<sup>62</sup> reported an alternative two-dimensional NMR processing method called, Covariance NMR spectroscopy. Since, in the covariance NMR spectrum, the spectral resolution of the indirect domain,  $F_1$ , is identical to the direct domain  $F_2$  regardless of  $N_1$ . Thereby, the covariance method can obtain high-resolution two-dimensional spectrum without the number of sampling of points in the indirect  $t_1$  domain.

### 3.2.2 Theory of the covariance NMR spectroscopy

Consider a set of 1D spectra with varying the evolution time  $t_1$  between every free induction decays (FIDs). Then, a time-domain matrix  $s(k_1, t_2)$ , where,  $k_1 = 1, \dots, N_1$  is the number of the experiment with evolution time  $t_1 = k_1 \cdot \Delta t_1$ , can be constructed. After Fourier transformation along  $t_2$  yields a data matrix containing the 1D absorption spectra as below

$$S(k_1, \omega_2) = \text{Re} \int_0^{t_{2,\max}} dt_2 \exp(-i\omega_2 t_2) s(k_1, t_2)$$

Since the FID is sampled digitally, the actual frequency domain,  $t_2$ , spectrum is calculated by discrete Fourier transformation

$$\begin{aligned} \sum_{j=0}^{N_2-1} s(k_1, j\Delta t_2) \exp(-i \frac{2\pi j k_2}{N_2}) &= S(k_1, 2\pi k_2/N_2 \Delta t_2) \\ &= S(k_1, \omega_2(l)) \end{aligned}$$

...  $\omega = k_2 \cdot \omega_0$ ,  $\omega_0$ ; increment of angular frequency  $= \frac{2\pi}{N}$

where,  $N_2$  is the number of data points in the frequency domain,  $t_2$ ,  $\Delta t_2$  is the sampling interval,  $k_2 = -N_2/2, \dots, N_2/2$  and  $l = 1, \dots, N_2$ .

Then, a mathematical covariance between two data arrays is given by

$$C_{ij} = \frac{1}{N_1 - 1} \sum_{k_1=1}^{N_1} \{S(k_1, i) - \langle S(i) \rangle\} \{S(k_1, j) - \langle S(j) \rangle\}$$

where  $S(k_1, i) = S(k_1, \tau_m, \omega_2(l))$  and the average spectrum  $\langle S(i) \rangle$  is given by

$$\langle S(i) \rangle = \frac{1}{N_1} \sum_{k=1}^{N_1} S(k, i)$$

### 3.2.3 Relationship between 2D NMR and Covariance NMR

In practical case such as  $S(k_1, \omega_2(l))$  is zero/near zero or  $\omega_2(l)$  is far from the on-resonance frequency (rapidly oscillating function),  $\langle S(k_1, \omega_2(l)) \rangle \cong 0$ . Then, the covariance calculation can be expressed as

$$C_{ij} = \sum_{k_1=1}^{N_1} \langle S(k_1, i) S(k_1, j) \rangle$$

and  $S(k_1, i)$  is real valued function. Thus, from the well-known Parseval's theorem as bellow

$$\int_{-\infty}^{\infty} f(t) g^*(t) dt = \frac{1}{2\pi} \int_{-\infty}^{\infty} F(\omega) G^*(\omega) d\omega$$

where  $F(\omega)$  and  $G^*(\omega)$  are the complex Fourier transforms of  $f(t)$  and  $g^*(t)$ .

A following relationship is deduced

$$C_{ij} = C_{\omega_i \omega_j} \propto \sum_{k_1=1}^{N_1} S(k_1, \omega_i) S(k_1, \omega_j)$$

Thus, the inner product of two columns of two-dimensional NMR data matrix,  $S(k_1, \omega_i)$ , is proportional to the covariance of time-domain signals of  $S(k_1, i)$ . Thereby, the covariance matrix  $\mathbf{C}$  can be expressed as a matrix operation of the signal data matrix  $S(k_1, \omega_i)$  and is given by

$$\mathbf{C} \propto \mathbf{S}^T \mathbf{S}$$

From the  $N_1 \times N_1$  covariance matrix  $\mathbf{C}$ , a symmetric two-dimensional like spectrum can be acquired from following operation<sup>63</sup>

$$\mathbf{S}_{sym} = \mathbf{C}^{1/2}$$

And the square root operation of covariance matrix  $\mathbf{S}_{sym} = \mathbf{C}^{1/2}$ , can be obtained by a following matrix diagonalization operation (=eigen-decomposition)

$$\mathbf{C} = \mathbf{U} \mathbf{\Lambda} \mathbf{U}^{-1}$$

Thus, the  $n^{\text{th}}$  power of  $\mathbf{C}$  is calculated as,

$$\begin{aligned} \mathbf{C}^n &= (\mathbf{U} \mathbf{\Lambda} \mathbf{U}^{-1})^n \\ &= \underbrace{(\mathbf{U} \mathbf{\Lambda} \mathbf{U}^{-1}) \dots (\mathbf{U} \mathbf{\Lambda} \mathbf{U}^{-1})}_n \end{aligned}$$

Since,  $\mathbf{U}^{-1} \mathbf{U} = \mathbf{I}$ , the square-root of  $\mathbf{C}$  is

$$\mathbf{C}^{1/2} = \mathbf{U} \mathbf{\Lambda}^{1/2} \mathbf{U}^{-1}$$

where  $\mathbf{U}$  is the eigenvector matrix of  $\mathbf{C}$  and  $\mathbf{\Lambda}$  is the diagonal eigenvalue matrix of  $\mathbf{C}$ .

### 3.2.4 Speeding up the eigen-decomposition by SVD

While the computation of covariance operation requires  $O(N_1 N_2^2/2)$  operations, for the square-root operation during the matrix diagonalization process it requires  $O(N_2^3)$  operations. Therefore, the number of sampling point,  $N_2$  is linearly increased, whereas the required operation will be increased exponentially. Trbovic *et al.*<sup>64</sup> reported a more time-efficient computational operation method based on singular value decomposition method.

For an any matrix  $\mathbf{S}^T$ , the singular value decomposition is given by

$$\mathbf{S}^T = \mathbf{U}\mathbf{\Sigma}\mathbf{V}^T$$

where both of  $\mathbf{U}$  and  $\mathbf{V}$  are orthogonal matrix and  $\mathbf{\Sigma}$  is a diagonal matrix with non-negative valued elements.

The covariance matrix  $\mathbf{C}$  of the matrix  $\mathbf{S}^T$  is defined as

$$\begin{aligned}\mathbf{C} &= \mathbf{S}^T \mathbf{S} = \mathbf{U}\mathbf{\Sigma}\mathbf{V}^T (\mathbf{U}\mathbf{\Sigma}\mathbf{V}^T)^T \\ &= \mathbf{U}\mathbf{\Sigma} \underbrace{\mathbf{V}^T \mathbf{V}}_{\mathbf{I}} \mathbf{\Sigma} \mathbf{U}^T \\ &= \mathbf{U}\mathbf{\Sigma}^2 \mathbf{U}^T\end{aligned}$$

Consequently, the symmetric matrix  $\mathbf{S}_{sym}$  can be express as

$$\mathbf{S}_{sym} = \mathbf{C}^{1/2} = \mathbf{U}\mathbf{\Sigma}\mathbf{U}^T$$

The principal advantage of SVD over the eigendecomposition method is that it only requires  $O(N_1^2 N_2)$  operations. In practice, the number of  $N_1$  (sampling points of the  $t_1$ -time domain) is typically smaller than  $N_2$  (sampling points of the  $t_2$ -time domain). Thus, for most of the square-roots operation can benefit from time-efficient of SVD operation.

### 3.2.5 Indirect Covariance NMR spectroscopy

According to *Parserval's* theorem in 2.2.3, the covariance calculation also applicable for between the frequency domain signal,  $S(\omega)$ , rather than the time-domain signal,  $s(t)$ . Moreover, if one interchange order of the matrix calculation ( $\mathbf{F}^T \mathbf{F} \rightarrow \mathbf{F} \mathbf{F}^T$ ), it results in a '*indirect*' covariance spectrum in which both axes consist of the indirect domain ( $\Omega_C$ ) of spectrum  $\mathbf{F}$ . Thus, for example, the covariance calculation of a hetero-nuclear correlation spectrum such as  $^1\text{H}$ - $^{13}\text{C}$  HSQC-TOCSY or  $^1\text{H}$ - $^{13}\text{C}$  HMBC spectrum also can be performed. Because the  $J$ -coupling correlation between low natural abundance nuclei ( $^{13}\text{C}$ ,  $^{15}\text{N}$  etc.) is hard to acquire, it has an enormous advantage in aspect to sensitivity. *Zhang et al.*<sup>50</sup> reported this alternative covariance NMR paper where they showed indirect-covariance of the several  $^1\text{H}$ - $^{13}\text{C}$  HSQC-TOCSY spectra of oligo-peptides can yield thereof  $^{13}\text{C}$ - $^{13}\text{C}$  TOCSY spectra. Since the spectral resolution of the indirect covariance of  $^1\text{H}$ - $^{13}\text{C}$  correlation spectrum is determined by the spectral resolution of the  $F_1\{^{13}\text{C}\}$  domain, it is important to set-up the number of  $t_1$  increments proper to desired spectral resolution of the indirect covariance spectrum.

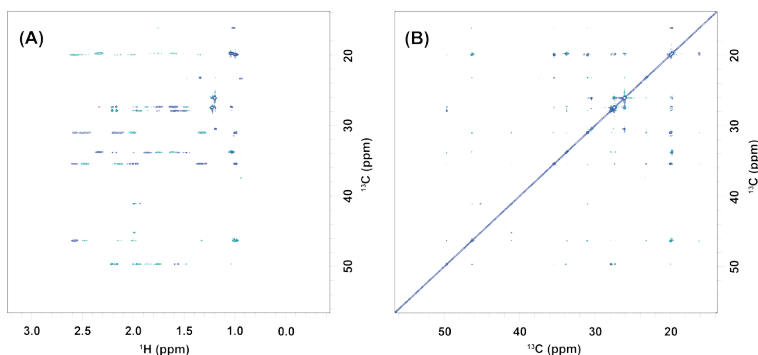


**Figure 3.1 Comparison of 2D NMR and its indirect covariance spectrum**

(A)  $^1\text{H}$ - $^{13}\text{C}$  HSQC-TOCSY spectrum of cyclosporine and (B) its indirect covariance spectrum

### 3.3 Spectral deconvolution of mixture using Covariance NMR

#### 3.3.1 Relationship between PCA and Covariance NMR

Principal Component Analysis (PCA)<sup>65</sup> is the multivariate analysis technique where it can give an information best explaining the

PCA of certain data matrix  $\mathbf{X}$ , can be done by following two-step operations.

1. Calculating the covariance matrix,  $\mathbf{C}$ , of the data matrix  $\mathbf{X}$
2. Eigen-decomposition of the matrix  $\mathbf{C} = \mathbf{S}\mathbf{\Lambda}\mathbf{S}^{-1}$

where,  $\mathbf{S}$  is the eigenvector matrix and  $\mathbf{\Lambda}$  is the eigenvalue matrix of  $\mathbf{C}$  respectively which satisfy  $\mathbf{C}\mathbf{S}_n = \lambda_n$  and the vectors thus obtained are then ordered such that  $\lambda_1 \geq \lambda_2 \dots \geq 0$ .

Back to the covariance NMR, the indirect/direct-covariance calculation of certain type of spin-spin correlation spectra (i.e.  $^1\text{H}$ - $^1\text{H}$  TOCSY,  $^1\text{H}$ - $^{13}\text{C}$  HSQC-TOCSY) is can be regarded as an intermediate form of PCA calculation. Therefore, the eigen-decomposition of covariance NMR spectrum can give an eigenvector matrix which contains eigenvector,  $\mathbf{S}_1$ , which best explains the its original form of one-dimensional NMR spectrum.

#### 3.3.2 NMR mixture analysis using PCA

In case of a chemical species mixture, the eigenvectors of covariance NMR matrix which correspond to dominant eigenvalues can be depicted as their individual one-dimensional NMR spectra. Considering mixture samples with  $n$ -chemical species, one can select  $n$ -eigenvectors in order of their corresponding eigenvalues. It is

demonstrated that using model mixture containing some amino acids every individual  $^1\text{H}$  NMR spectra were extracted from the covariance matrix of  $^1\text{H}$ - $^1\text{H}$  TOCSY spectra with varying mixing times<sup>4</sup>.



### 3.4 High-quality HMBC spectra using NUS-mHMBC

Though the  $^1\text{H}$ - $^{13}\text{C}$  HMBC spectrum provides wide-range of connectivity between proton and carbon spins including quaternary carbons, however, it remains several limitations which hampers constructing the  $^{13}\text{C}$ - $^{13}\text{C}$  correlation spectrum by indirect covariance operation. The following description discusses the problems of HMBC measurement sequences that impede the creation of desirable  $^{13}\text{C}$ - $^{13}\text{C}$  correlation spectra by the indirect covariance operation, and to address the design of modified HMBC pulse sequence and their application to actual natural compound.

#### 3.4.1 Resolution enhancement of the indirect domain

The line-shape of indirect covariance spectrum is similar to general two-dimensional Fourier Transform spectrum and can be expressed as

$$C_{m,\Omega} \propto \sum_{k=1}^{N_1} S(m, k) \cdot S(\Omega, k)$$

Assume  $N_1 = 1$ , then  $C_{m,\Omega} = S(m) \cdot S^T(\Omega)$  where  $S(m) = \delta > 0$  and  $S(\Omega) \geq 0$

Therefore, the actual line shape of  $C^\Omega$  ( $\Omega^{\text{th}}$  row vector of the matrix  $\mathbf{C}$ ) is proportional to distribution of non-zero entities ( $\approx$  line width) of  $S(\Omega)$ .

$$C^\Omega = \delta \cdot S(\Omega)$$

Thus, the actual line-shape along the  $F_2$  domain of covariance signal  $C_{m,n}$  ( $C^m$ ;  $m^{\text{th}}$  row vector of the matrix  $\mathbf{C}$ ) follows line-shape of cross peak at  $S(k, n)$  along the  $F_1$  domain vice versa. Likewise, both line-shape of the indirect covariance signal is related to the line-shape of the indirect domain of the template spectrum. In other words, the symmetric indirect covariance operation using the  $^1\text{H}$ - $^{13}\text{C}$  HMBC spectrum yields  $^{13}\text{C}$ - $^{13}\text{C}$  correlation spectrum where both of frequency domain features were originated from the indirect domain ( $F_1$ ) of template spectrum. In general,

however, the indirect domain has a poor spectral resolution due to the limited number of  $t_1$  increments. The truncation of FID due to limited  $t_1$  sampling points gives undesired ripples around signal the peak after Fourier transformation, thus a convolution of the truncated signal with the several types of window function performed which eventually induce severe line broadening. To alleviate truncate effect and related line-broadening, the acquisition time,  $t_{1,max}$ , should be increased. But, the sampling points in the indirect domain are typically limited small than thereof  $t_2$  time domain. To improve the spectral resolution of the indirect domain, therefore, NUS acquisition was employed instead of the uniform sampling. Yet, reduced total number of  $t_1$  sampling points also decrease the total volume of the signal envelope, for many cases in dealt with small molecule, it provides a reasonable sensitivity in resulted NUS spectrum.

### 3.4.2 Modification of the HMBC pulse sequence

Pulse sequence for the modified HMBC (mHMBC) is shown in Figure 2.2. In case of the usual HMBC pulse sequence, it gives a phase-twisted line shape due an absence of reverse INEPT<sup>66</sup> and  $^{13}\text{C}$  decoupling pulse sequence.

Assume that the density operator at a beginning of an acquisition in the conventional HMBC pulse sequence has a form of

$$\hat{\rho}(t_1, 0) = \sum_k A_k \hat{I}_- \hat{S}_z \cos(\Omega_{k,s} t_1)$$

where a Hamiltonian  $\hat{H}_0 = \sum_k 2\pi J_{IS_k} \hat{I}_z \hat{S}_{k,z}$  and  $J_{IS_k}$  is a  $J$ -coupling constant between proton-spin ( $I$ ) and carbon-spins ( $S_k$ ) and  $A_k$  is a polarization transfer efficiency from  $I$  to  $S_k$  according to  $\sin(\pi J_{IS_k} \tau)$ .

During the acquisition,  $t_2$ , the evolution of density operator is given by

$$\hat{\rho}(t_1, t_2) = \sum_k A_k \hat{I}_- \hat{S}_z \cos(\Omega_{k,s} t_1) \cos(\pi J_{\text{IS}_k} t_2) + i \sum_k A_k \hat{I}_- \cos(\Omega_{k,s} t_1) \sin(\pi J_{\text{IS}_k} t_2)$$

And the observable magnetization is computed by

$$M_+(t_1, t_2) \propto \text{Tr}(I_+ \hat{\rho}(t_1, t_2))$$

Since the trace of  $\hat{I}_- \hat{S}_z = 0$

$$\begin{aligned} M_+(t_1, t_2) &\propto \text{Tr}(I_+ \hat{\rho}(t_1, t_2)) \\ &\propto i \sum_k A_k \cos(\Omega_{k,s} t_1) \sin(\pi J_{\text{IS}_k} t_2) \end{aligned}$$

Thus, each of HMBC peaks exhibits the anti-phase  $^n J_{\text{CH}}$  modulation along the  $F_2$  domain according to its  $^1\text{H}$ - $^{13}\text{C}$  correlations. It turns out that additional  $^n J_{\text{CH}}$  splitting and different  $J$ -splitting patterns of HMBC peaks stem from identical proton are undesirable for the latter spectral deconvolution processing procedure. Thereby, decoupled-HMBC<sup>67</sup> type pulse sequence was chosen to template pulse sequence. As stated above, the line width of the indirect covariance spectrum depends on the line width of the indirect domain of template spectrum. Since the magnitude processing along the indirect domain will broaden the line width, absorptive Lorentzian line shape was retained by employing the echo-antiecho<sup>68,69</sup> type acquisition mode. On the other hands, in general, to remove undesired one-bond correlation,  $^1 J_{\text{CH}}$ , peak from the HMBC spectrum the Low-Pass  $J$  filter (LPJF)<sup>70</sup> has been included in the pulse sequence of HMBC. Conversely, LPJF was omitted in modified HMBC pulse sequence to preserve one-bond correlation peak. The one-bond C-H correlation peak was found to be useful for constructing a  $^{13}\text{C}$ - $^{13}\text{C}$  correlation through covariance calculations while its incomplete suppression by LPJF, in the absence of  $^{13}\text{C}$ -decoupling sequence, can result in a spurious correlation during the indirect covariance operation.

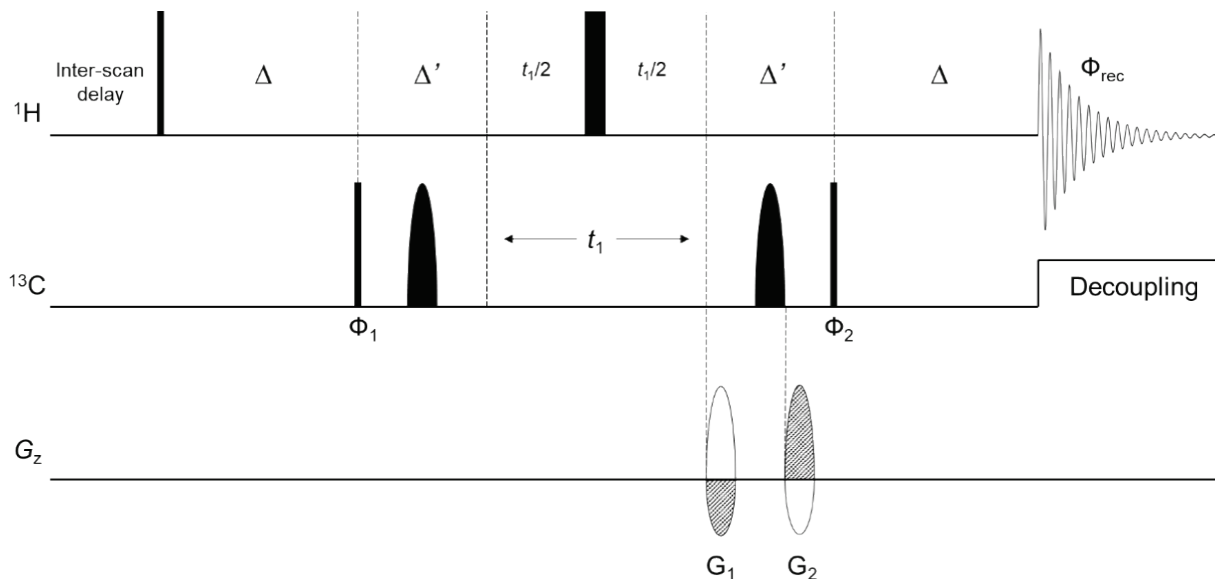


**Figure 3.2** Pulse sequence for mHMBC

For rotenone,  $\Delta$  was 62.5 ms ( $^nJ_{\text{CH}} = 8$  Hz). For rotenone and brucine mixture, (A) with  $\Delta$  of 62.5 ms ( $^nJ_{\text{CH}} = 8$  Hz) and  $\Delta$  of 125 ms ( $^nJ_{\text{CH}} = 4$  Hz) were used. The semi-ellipsoid boxes represent  $180^\circ$  shaped pulses for inversion or refocusing of  $^{13}\text{C}$  magnetization. Narrow and wide bars represent  $90^\circ$  and  $180^\circ$  hard pulses, respectively. For the phase-sensitive acquisition in the indirect domain, an echo-antiecho detection mode was employed. Phases of  $\Phi_1$  and  $\Phi_{\text{rec}}$  were shifted by  $180^\circ$  at every even-numbered increment. Blank semi-ellipse boxes in the gradient channel represent gradient pulses for odd-numbered increments and gray semi-ellipse boxes for even-numbered increments. All pulses are of phase, x unless otherwise indicated. The phase cycling is as follows.  $\Phi_1 = x, -x$ ;  $\Phi_2 = -x, -x, x, x$ ;  $\Phi_{\text{rec}} = -x, x, x, -x$ . Gradient ratios:  $G_1 : G_2 = 5 : -3$  (odd-numbered) and  $-3 : 5$  (even-numbered).

## 3.5 Experimental section

### 3.5.1 NMR measurements

All NMR spectra were measured at 298 K with 850 or 800 MHz Bruker Avance III HD spectrometers equipped with 5 mm CPTCI CryoProbes (Bruker BioSpin, Germany). For the rotenone sample, 2 mg of rotenone (Sigma-Aldrich, MO, USA) was dissolved in 600  $\mu$ L of chloroform-*d*. For 2D NMR experiments, the pulse sequence in Figure-2.2 was used. For apodization, cosine-squared function ( $F_1$ ) and cosine function ( $F_2$ ) were employed and zero-filling was applied to both dimensions. All spectra were processed in phased mode along the  $F_1$  domain, while  $F_2$  domain was processed in either phased or magnitude mode as necessary. For the HMBC of rotenone with NUS, the actual time-domain points were  $2048 \times 72$  ( $t_2 \times t_1$ ) complex points with the final  $4096 \times 4096$  ( $t_2 \times t_1$ ) complex points after NUS reconstruction and zero-filling. The spectral width was  $9615 \times 46280$  Hz ( $F_2 \times F_1$ ) and the frequency offsets were 4001 Hz and 22133 Hz for  $^1\text{H}$  and  $^{13}\text{C}$  nuclei respectively. For mHMBC ( $^nJ_{\text{CH}} = 8$  Hz; delay  $\Delta$ : 62.5 ms), the number of scans was 32 and the total experiment time was about 1 hr 46 min. For US-mHMBC, actual time-domain points were  $2048 \times 72$  ( $t_2 \times t_1$ ) complex points with the final  $4096 \times 4096$  ( $t_2 \times t_1$ ) complex points after zero-filling and linear prediction. For 1, *n*-ADEQUATE<sup>71</sup>, ‘adeq1netgp’ in the Bruker pulse library was used with standard parameters. The inter-scan delay was 1.0 s, the number of scans was 32, and the actual time-domain points were  $1024 \times 72$  ( $t_2 \times t_1$ ) complex points. The spectral width was  $11904 \times 51314$  Hz and the total experiment time of the 1, *n*-ADEQUATE was about 1 hr 40 min.

### 3.5.2 NUS sampling schedule.

The NUS sampling schedule was generated by Schedule Generator Version 3.0 (available at [http://gwagner.med.harvard.edu/intranet/hmsIST/gensched\\_new.html](http://gwagner.med.harvard.edu/intranet/hmsIST/gensched_new.html))

with 7% sampling density. A total of 72 NUS sampling points was used to give final 1024 complex points in the indirect dimension. The data were processed with nmrPipe<sup>72</sup> on CentOS 6.5 with the NUS data reconstruction performed by hmsIST<sup>73</sup> script provided by the above site.

## 3.6 Results and discussion

### 3.6.1 High-resolution mHMBC spectrum with NUS acquisition

Figure 2.3 compares the effect of NUS acquisition and pulse modification. Each spectrum was obtained with rotenone (Figure 2.3A and B), a complex natural product consisting of 23 carbons with 10 quaternary carbons<sup>74</sup>. For NUS acquisition the sampling schedule was obtained using the hmsIST algorithm<sup>73</sup> and featured a 7% sampling rate with 72  $t_1$  complex points corresponding to 1024  $t_1$  complex points in US acquisition scheme. For the uniform sampling,  $t_1$  complex points were identical to NUS acquisition (72 complex points). Visually, the peaks were not resolved in the US spectrum were baseline-resolved in the NUS spectrum. The removal of splitting sideband by mHMBC pulse sequence is also shown in Figure 2.3C and D, which should be helpful in suppressing artifacts during thereof downstream covariance operation.

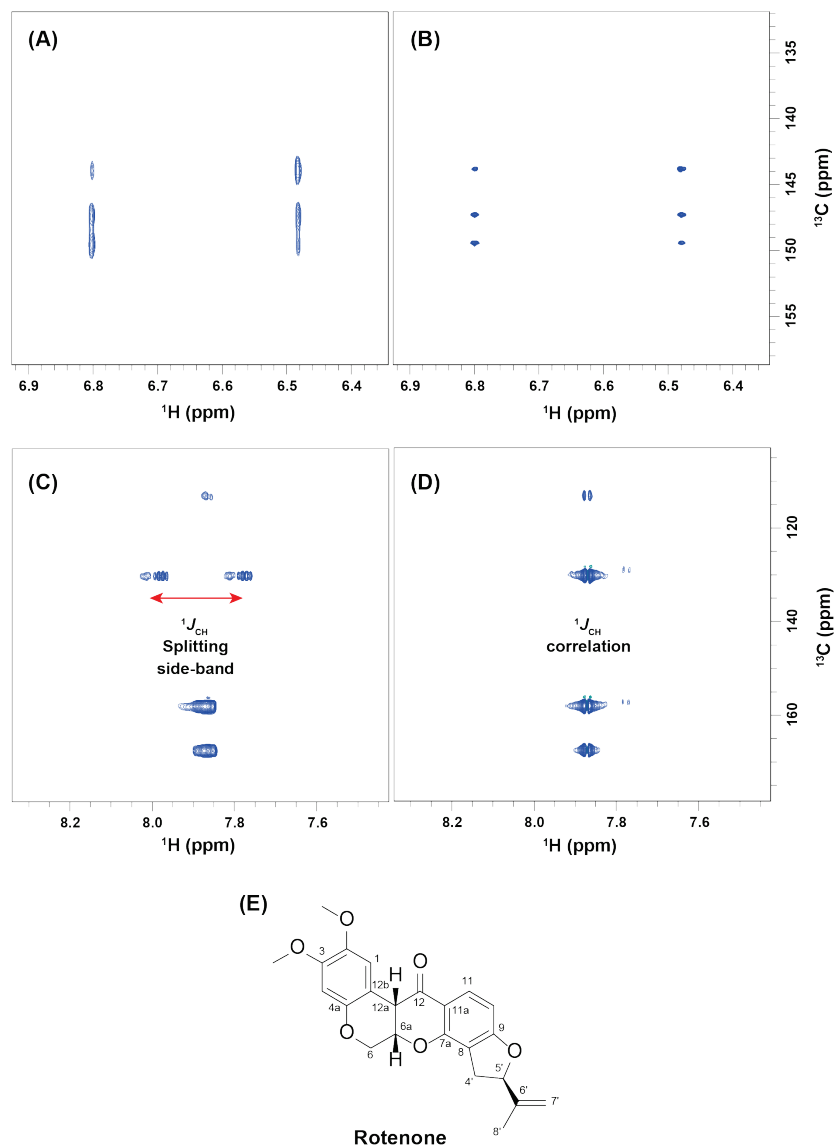


**Figure 3.3** The effect of mHMBC and NUS on rotenone.

(A and B) Comparison of mHMBC spectra using NUS sampling (A) and conventional US-sampling (B). FWHHs of the carbon signals were obtained from each trace at 188.02 ppm by a positive projection along  $F_1$  (Dashed rectangles). (C and D) Comparison of undesired  $^1J_{\text{CH}}$  splitting on cHMBC (C) and mHMBC (D) spectra. (E) Structure of rotenone.



### 3.6.2 iCov on NUS-mHMBC for $^{13}\text{C}$ - $^{13}\text{C}$ correlation spectrum

The high-resolution HMBC spectrum thus obtained followed by indirect covariance operation to acquire direct  $^{13}\text{C}$ - $^{13}\text{C}$  connectivity information. As stated, the resolution of the original spectrum is crucial for an indirect covariance (iCov) operation, as an overlap can give rise to a spurious correlation. As shown in Figure 2.4A and B, the iCov on the NUS spectrum clearly gave much high-resolution iCov spectrum and more resolved peaks than that of US spectrum. Three successive carbon off-diagonal peaks around the diagonal region just spaced by 0.36 and 0.39 ppm (ca. 78 and 84 Hz), were clearly resolved in the iCov spectrum using NUS spectrum. However, they were shown as converged single peak in the iCov spectrum using US spectrum. The superiority of NUS approach in peak assignment for the structure elucidation was proved in Figure 2.5 as an example with rotenone. Two carbon signals showed very small chemical shift difference ( $\Delta\delta_c=0.09$  ppm, 20 Hz), but correlated thereof signals were clearly identifiable as an individual peak, thereby removing ambiguity in NMR assignment of complex natural product, rotenone. On the other hands, there are different types of NMR experiment which can give direct  $^{13}\text{C}$ - $^{13}\text{C}$  correlation information such as 1, $n$ -ADEQUATE<sup>71</sup>. It should be note that such experiment did not provide any signals from the same sample within the same experimental time (Figure 2.6). In summary, NUS-mHMBC approach should be useful in signal assignment between adjacent peaks frequently encountered in natural product structure analysis.

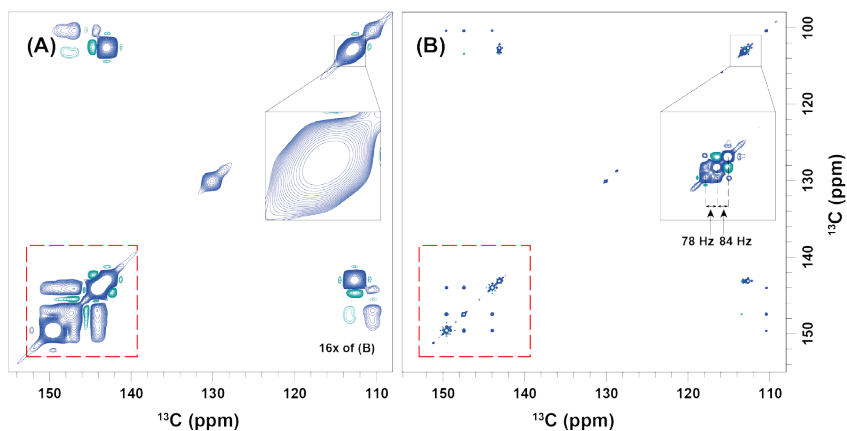


**Figure 3.4 Comparison of iCov spectra of rotenone**

(A) NUS-mHMBC and (B) US-mHMBC.

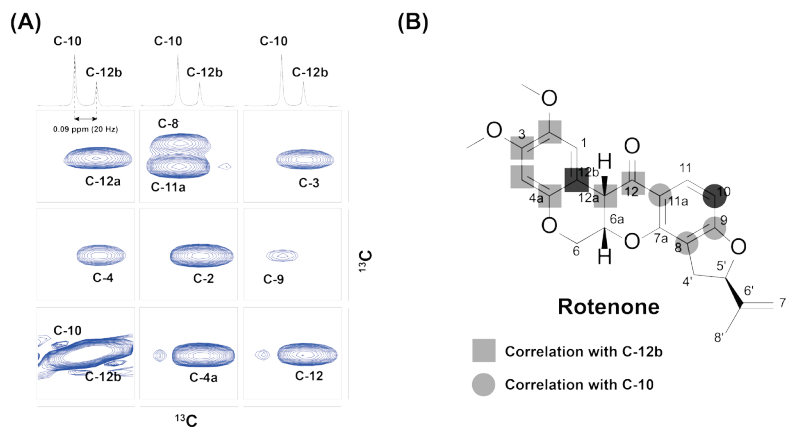


**Figure 3.5 Application of iCov spectrum for the structural assignment**

(A) Enlarged regions of NUS-mHMBC-iCov spectrum showing cross-peaks of C-10 and C-12b of rotenone. (B) The position of each carbon on rotenone correlated with C-10 and C-12b identified in (A).

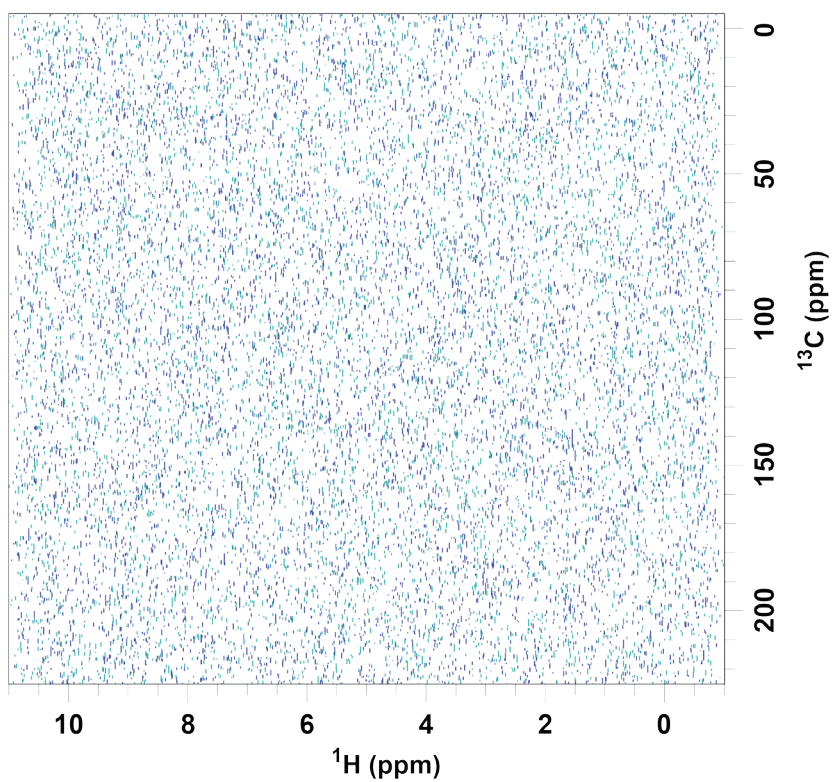


**Figure 3.6** An 1,  $n$ -ADEQUATE spectrum of rotenone

(2 mg in 600  $\mu\text{L}$  of  $\text{CDCl}_3$ )

### **3.7 Mixture analysis with iCov-NUS-mHMBC spectrum**

#### **3.7.1 Limitations of iCov for the spectral deconvolution**

Then, the obtained high-quality  $^{13}\text{C}$ - $^{13}\text{C}$  correlation spectrum was applied to other issue in NMR studies, which is mixture analysis. A model mixture of 1:1 ratio of rotenone and brucine<sup>75</sup> totaling 46 carbons (including 17 quaternary carbons) was prepared. First of all, to verify whether the constructed  $^{13}\text{C}$ - $^{13}\text{C}$  spectrum can provide all of the peaks of the actual 1D carbon spectrum of mixture, from the covariance spectrum its one-dimensional projection spectrum was obtained. Regretfully, the projection spectrum did not provide all of the peak of the actual 1D carbon spectrum of mixture. This means that the NUS-mHMBC-iCov approach, although useful in construction of reliable  $^{13}\text{C}$ - $^{13}\text{C}$  correlation map of single compound, is yet not adequate enough to give the complete molecule-wide connectivity information. Moreover, spurious intermolecular connectivity between rotenone and brucine also was exist. (Figure 2.7). Thereby, in following descriptions, consideration for the spectral deconvolution using iCov-NUS-mHMBC spectrum in aspect of NMR data acquisition and processing methods will be discussed.

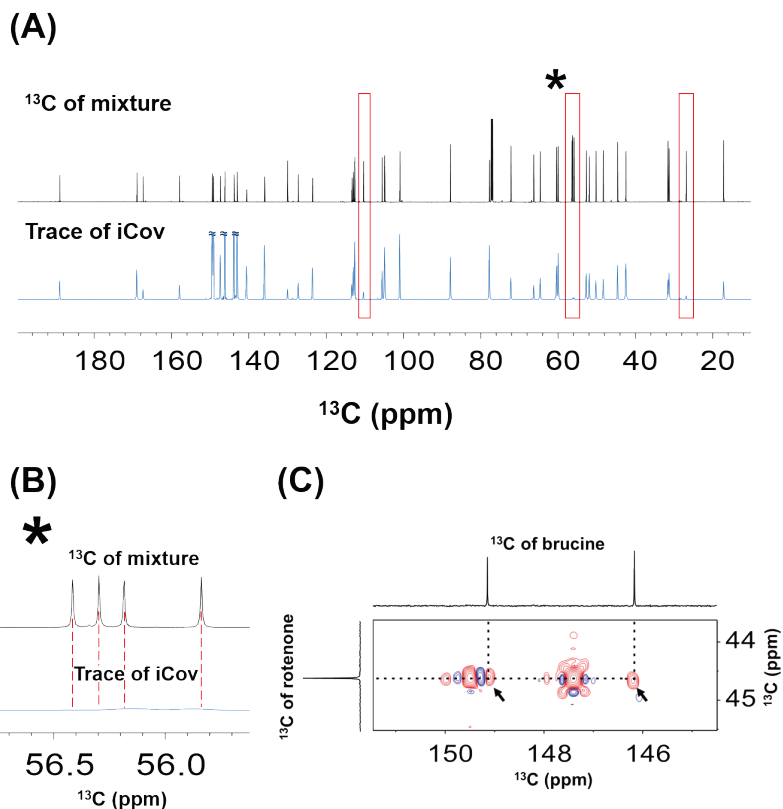


**Figure 3.7** iCov-NUS-mHMBC spectrum of mixture

(A)  $^{13}\text{C}$  spectrum of mixture of rotenone and brucine (Black, upper) and the trace of the iCov spectrum (Blue, lower). (B) Expansion of the 56 ppm region of (A). The missing signals are indicated by dashed lines. (C) False positive intermolecular correlations on the iCov spectrum (arrows).

### 3.7.2 The heterogeneity of HMBC correlation information.

With neglecting the relaxation term and  $J$ -coupling interaction between proton spins, the  $^{13}\text{C}$  decoupled-HMBC signal is expressed as

$$M_+(t_1, t_2) \propto \text{Tr}(I_+ \hat{\rho}(t_2))$$

$$\propto i \sum_{k=1}^{N_1} \sum_{l=1}^{N_2} A_{kl} \cos(\Omega_{k,s} t_1) B_l \exp(i\Omega_l t_2)$$

where  $A_{kl}$  is the polarization transfer efficiency between proton spin  $I_l$  and carbon spin  $S_k$  and  $B_l$  is amplitude of spin  $I_l$ .

Thus, the resulted signal matrix  $S$  is given by

$$S_{kl} \propto A_{kl} D_{ll}$$

Hence, the off-diagonal signal (cross peak) in the indirect covariance  $C_{m,n}$  ( $m \neq n$ ) can be expressed in

$$C_{m,n} \propto \sum_{l=1}^{N_2} S_{ml} S_{nl}$$

$$\propto \sum_{l=1}^{N_2} A_{ml} D_{ll} A_{nl} D_{ll} = \sum_{l=1}^{N_2} A_{ml} A_{nl} D_{ll}^2$$

where  $m \neq n$  and  $D$  is a  $l \times l$  diagonal matrix.

Therefore, to get an off-diagonal signal in the indirect covariance spectrum it requires at least two non-zero  $^nJ_{CH}$  correlation signals in the HMBC spectrum. As isolated protons (such as methoxy group) correlate with very few carbons on HMBC, often with just one, the peaks for these  $^1H$ - $^{13}C$  pair are likely to be very weak, if ever present, one the resulting NUS-mHMBC-iCov spectrum. In other words, the polarization transfer efficiency is an important factor in mHMBC-iCov spectrum. In the mHMBC pulse sequence efficient coefficient  $A_{kl}$  is given by

$$A_{kl} = \sin(\pi J_{lk} \tau)^2$$

where  $J_{lk}$  is  $J$ -coupling constant between proton spin ( $I_l$ ) and carbon spin ( $S_l$ ) and  $\tau$  is the delay in INEPT<sup>76</sup> and reverse INEPT sequence.

If the  $^1\text{H}$ - $^{13}\text{C}$  correlation pair shows  $J_{lk}$  value close to the integer multiple of the  $1/\tau$ , (0, 1, 2 ... ; which is also frequently appeared in one-bond  $^{13}\text{C}$ - $^1\text{H}$  correlation pair) then the transfer efficiency  $A_{kl}$  falls into null making the peak invisible.

### 3.7.3 Signal overlap on the $F_2$ projection domain

Any partial signal overlaps between different protons, not the identical one, give rise to spurious intra/intermolecular correlations on the indirect covariance spectrum, resulting an entanglement of spectrum of individual chemical species.

Suppose that  $\mathbf{S}^k$  which is the HMBC correlation group originated from  $^1\text{H}$  spin on the certain single carbon nucleus. Then HMBC spectrum can be expressed as sum of the HMBC correlation group  $\mathbf{S}^\Sigma$ .

$$\mathbf{S}^\Sigma = \sum_{k=1}^N \mathbf{S}^k$$

Since the covariance of two NMR signal array  $S_{ml}$  and  $S_{nl}$  is defined as

$$C_{m,n} \propto \sum_{l=1}^{N_2} S_{ml} S_{nl}$$

Considering the sum of two different HMBC correlation group

$$C^{\mathbf{S}^1 + \mathbf{S}^2}_{m,n} \propto \sum_{l=1}^{N_2} \{S_{ml}^1 S_{nl}^1 + S_{ml}^2 S_{nl}^2 + (S_{ml}^1 S_{nl}^2 + S_{ml}^2 S_{nl}^1)\}$$

If  $S_{ml}^1 S_{nl}^2 \cdot S_{ml}^2 S_{nl}^1 \neq 0$ , the false covariance correlation due to the partial proton signal overlap is generated as

$$\sum_{l=1}^{N_2} A_{ml}^1 A_{nl}^2 D_{ll}^1 D_{ll}^2 + A_{ml}^2 A_{nl}^1 D_{ll}^1 D_{ll}^2$$

General form of the covariance signal is given by

$$\begin{aligned}
 C_{m,n}^{\Sigma} &\propto \sum_{i=1}^N \sum_{j=1}^N \sum_{l=1}^{N_2} S_{ml}^i S_{nl}^j \\
 &\propto \sum_{i=1}^N \sum_{j=1}^N \sum_{l=1}^{N_2} A_{ml}^i A_{nl}^j D_{ml}^i D_{nl}^j
 \end{aligned}$$

$$\text{where } \begin{cases} i = j & \text{True correlation} \\ i \neq j & \text{False correlation} \end{cases}$$

### 3.7.4 Disproportion of the signal intensity

In the theory of covariance NMR (2.2.2), it is assume that in case such as  $S(k_1, \omega_2(l))$  is zero/near zero or  $\omega_2(l)$  is far from the on-resonance frequency (rapidly oscillating function),  $\langle S(k_1, \omega_2(l)) \rangle \cong 0$ . The indirect covariance operation, however, dealt with indirect domain signal whose mean value  $\langle S(t_1, k_2) \rangle$  is not generally zero. This is because of relatively small sampling points and sometimes its small off-resonance frequency<sup>77</sup>. Thus, the normalization of signal can pose a different non-zero mean value,  $\mu$ , to every indirect domain signal,  $S(t_1, k_2)$ .

The covariance between two variables  $X$  and  $Y$  is defined as

$$\begin{aligned}
 \text{Cov}(X, Y) &= \frac{1}{M} \sum_{i=1}^M (X_i - \bar{a}) \cdot (Y_i - \bar{b}) \\
 &= \frac{1}{M} \sum_{i=1}^M (X_i Y_i - \bar{b} X_i - \bar{a} Y_i + \bar{a} \bar{b}) \\
 &= \frac{1}{M} \left( \sum_{i=1}^M X_i Y_i - \bar{b} \sum_{i=1}^M X_i - \bar{a} \sum_{i=1}^M Y_i + \sum_{i=1}^M \bar{a} \bar{b} \right) \\
 &= \frac{1}{M} \sum_{i=1}^M X_i Y_i - \bar{a} \bar{b}
 \end{aligned}$$

where,  $\bar{a}$  and  $\bar{b}$  are the mean value of  $X$  and  $Y$  respectively.



Thus, for the signals with non-zero mean value, their covariance has an additional value,  $\mu_a \cdot \mu_b$ , than the covariance between signals with zero mean value which is computation form assumed in the general Covariance NMR spectroscopy.

Moreover, the linear combination of covariance follows

$$ab \cdot \text{Cov}(X, Y) = \text{Cov}(aX, bY)$$

and

$$\text{Cov}(V + W, X + Y) = \text{Cov}(V, X) + \text{Cov}(V, Y) + \text{Cov}(W, X) + \text{Cov}(W, Y)$$

Note that the most of covariance from the HMBC signal show the positive covariance correlation which means an additive covariance and the intensity of HMBC signal is proportional to the transfer efficiency  $A_{ml}$  which is depends on the molecular environment. Since the value of covariance  $C_{mn}$  between two array  $S_{ml}$  and  $S_{nl}$  is proportional to  $\sum_l A_{ml} A_{nl} D_{ll}^2$ , thereby each transfer efficiency, initial intensity of proton spin and the number of non-zero element of  $D_{ll}$  (which account for the number of cross correlation signals between two carbons) are contribute to the intensity of covariance signal together. Thus, among the carbon spins in mixture sample, the carbon spins correlated with many proton / high intensity proton ( $\sum_l D_{ll}^2$ ) or has high transfer efficiency ( $A_{kl}$ ) will have disproportionately large signals on the covariance spectrum, dwarfing other signals in the indirect covariance spectrum.

### 3.7.5 Undesirable covariance signal line shape

Though the increase of  $t_{1,max}$  such as NUS acquisition in the indirect domain can reduce FID truncation artefacts and also alleviate the line-broadening accompanied apodization processing<sup>78</sup>, in the peak shape of strong signal shows cross-shaped ridges that can overlap with the projections of other peaks. In terms of computing of PCA this kind of spatial signal overlap between peak ridges and true signal/ridges

will be regarded also as correlation of certain carbons and this will lead to the spurious intra/intermolecular peaks.

### 3.8 Signal processing tailored to iCov-eigendecomposition

The processing procedure termed DECODE (DEconvolution of mixed spectrum from carbon carbon COrrrelation spectrum using enhanced DEMix), which tailored to the indirect covariance-eigendecomposition, was devised. Since the NUS-mHMBC-iCov approach did not provide satisfactory results for mixture deconvolution, a stepwise operation has been devised to make it better suited for providing molecule-wide spin network information.

#### 3.8.1 Spectral merging

The first consideration was that a single HMBC focusing on typical  ${}^{2-3}J_{\text{CH}}$  of 8 Hz may not give all the carbon correlation information on the HMBC-iCov spectra, because some carbon-proton pairs have lower coupling constants. Therefore, two HMBC spectra with delays optimized for 8 and 4 Hz were obtained separately and merged in the frequency domain. On top of this, an HSQC spectrum was also merged so that much-isolated carbons, i.e. methoxy carbons, can also appear on HMBC-iCov spectrum at its own chemical shift position. In the merging process, the maximum intensities were taken as the final values to avoid repetitive addition of the same peak on different spectra.

The spectral merging step constructs  $n \times n$  matrix  $\mathbf{H}$ , which takes the maximum magnitude from the individual spectrum,

$$H_{ij} = \max(S_{ij}^1, S_{ij}^2, \dots, S_{ij}^k)$$

where,  $\mathbf{S}^k$  is an  $n \times n$  matrix which represent the individual spectrum and  $\max(x, y, \dots, z)$  returns a maximum magnitude value among variables.

### 3.8.2 Calculation of the first moment for the spectral moment filtering

Second, as stated above the partial proton overlap on the  $F_2$  projections of HMBC peaks may generate false positive intermolecular correlation on the iCov spectrum, they were addressed by the spectral moment filter<sup>79</sup> (here, the first moment filter) before the iCov operation. The principle of the first moment filter was demonstrated before and conceptually similar to peak centroiding in mass spectrometry. Every signal on the spectrum were associated with the mean position value of the corresponding peak. When performing the iCov operation, the mean position values of each element of the two vectors were considered. If they differ by a certain margin, i.e. elements from different peaks, the products of the two elements were multiplied by 0 (filtered). Therefore, this filter prevents the false positive correlation due to proton projection overlaps on the HMBC spectrum.

The first moment matrix  $\mu$  is calculated as follows. Here, the power spectrum  $\mathbf{P}$  instead of the original spectral matrix  $\mathbf{H}$  to construct the first moment matrix ( $P_{ij} = H_{ij}^2$ )

$$\mu_{ij} = \sum_{k=-M}^M (j+k) P_{i,j+k} / \sum_{k=-M}^M P_{i,j+k}$$

where  $M = 7$  (15 points;  $2M + 1$ ) in 4096 points correspond to *ca.* 37 Hz for 12 ppm spectral width at 850 MHz. This first moment was used during the covariance calculation as an argument for the filter function.

### 3.8.3 iCov calculation with the spectral moment filtering function

Then, the indirect covariance matrix  $\mathbf{C}$  was obtained as below

$$W_{ij} = \sum_{k=1}^n \text{abs}(H_{ik}) \cdot \text{abs}(H_{jk}) \cdot f(\mu_{ik} - \mu_{jk})$$

$$\mathbf{C} = \mathbf{W}^{1/2}$$

where  $\mathbf{H}$  is the merged spectral matrix,  $\boldsymbol{\mu}$  is the first spectral moment obtained above, and  $n$  is the number of columns in  $\mathbf{H}$ .  $\text{abs}(\mathbf{H})$  returns the absolute values of the matrix  $\mathbf{H}$  and the filter function  $f$  is defined as

$$f(x) = \frac{1}{1 + \exp\{-10(1.4 - x)\}}$$

### 3.8.4 Dataset normalization

The third consideration is about the disproportionately large signals dwarfing others in the iCov spectrum. As stated in 2.7.4, it is not proper that the applying of the usual normalization for the iCov of two-dimensional NMR spectrum. Since the dynamic range of iCov signal can be affected by several factors (A *relative weight ratio* of mixture molecules and *intensities* of individual HMBC correlation signal etc.) this intensity disproportion was addressed by the intensity normalization using a sigmoid function.

The elements of the covariance matrix were normalized with a sigmoid function as below

$$L_{ij} = \frac{1}{1 + \exp\{-30(\log C_{ij} / \log C_{max}) + \delta\}}$$

where  $C_{max}$  and  $\delta$  were the maximum value of the matrix  $\mathbf{C}$  and the inflection point of the sigmoid function (customizable), respectively. For the logarithm calculation, if  $C_{ij} < 1$  then,  $C_{ij} = 1$  Note that a value of the inflection-point in the sigmoid function is user-customizable.

### 3.8.5 Peak-digitization

The fourth consideration is about the overlaps between peak projections in the carbon dimension on the iCov spectrum due to cross-shaped ridges. This issue was addressed by peak digitization based on the peak position information from the one-dimensional (1D) carbon spectrum of the mixture. Usually, one can simply use the diagonal slice of the NUS-mHMBC-iCov which is essentially the  $^{13}\text{C}$  spectrum of the mixture with reasonable resolution. For compounds with high carbon overlaps, as in the rotenone and brucine mixture, one can obtain the actual  $^{13}\text{C}$  spectrum of the mixture with higher resolution. Even for this case, the diagonal slice of the NUS-mHMBC-iCov gave well-separated individual spectra except for a total of 4 unresolved peaks (data not shown) which could be resolved by the use of the actual 1D spectrum of the mixture. It should be noted that the spectra of the individual compounds are never needed. From the 1D spectrum, one can tabulate every peak position by peak-picking and use them to represent all the iCov spectral peaks with three adjacent points centered on the peak position. The spectrum will have positive values at the picked position and the positions offset by one point from the peak-picked position, and all other regions will have zero values. This takes advantage of the ridge-free sharp lines of  $^{13}\text{C}$  spectra, and effectively removes spectral ridges on the resulting 2D spectrum. This digitized spectrum is then used as the input for the eigen-decomposition for spectral deconvolution at the final step of the DECODE procedure.

#### Step 1.

**Define** an array **P** with positional indices of valid peaks\* over a user defined threshold in  $^{13}\text{C}$  spectrum

Next, define a binary array **B** and its diagonal matrix **D** ( $=\text{diag}(\mathbf{B})$ ) such that

**for** all  $x$ , the positional indices of the  $^{13}\text{C}$  spectrum

$$B[x] = \begin{cases} 1, & \text{if } x \vee x \pm 1 \in \text{array } \mathbf{P} \\ 0, & \text{otherwise} \end{cases}$$

$$\mathbf{D} = \text{diag}(\mathbf{B})$$

**Step 2.**

**for** all  $k$ , the indices of non-zero elements of  $\mathbf{B}$

**Define** an array  $\mathbf{M}$  with the positional indices of valid peaks\*

over 0.01 threshold in  $L_k$  ( $L_k$  is the  $k^{\text{th}}$  1D slice (row/column) of the matrix  $\mathbf{L}$ )

**for** all  $i$ , index of 1D spectrum array of  $L_k$

$$L_k[i] = \begin{cases} L_k[i], & \text{if } i \in \text{array } \mathbf{M} \\ 0, & \text{otherwise} \end{cases}$$

**Step 3.**

Constructing the ridge-free matrix  $\mathbf{F}$  by following matrix operation

$$\mathbf{F} = \mathbf{D}\mathbf{L}\mathbf{D}$$

\* Throughout the pick-digitization process a function ‘scipy.signal.find\_peak’ from the SciPy library from python was used for the peak-detection.

### **3.8.6 Extracting eigenmodes; individual 1D spectra**

An eigendecomposition of the matrix  $\mathbf{F}$  ( $\mathbf{F} = \mathbf{V}\mathbf{\Lambda}\mathbf{V}^{-1}$ ) yields eigenmodes. Here, each eigenmode is  $V_k$  where  $V_k$  is the column vector (the eigenvector of the matrix  $\mathbf{F}$ ) of  $\mathbf{V}$ . The number of the desired eigenvectors (1D spectra) can be specified. The eigenvectors are calculated in descending order of the associated eigenvalues.

### 3.8.7 An optional $J$ -modulation-based overlap filter

Except for singlet type protons, every cross peaks generated in mHMBC spectrum used here, if did not undergo magnitude calculation along the  $F_2$  domain, have its own proton multiplet structures on account of the  $J_{\text{HH}}$ -modulation generated during the pulse sequence. Thus, one can further exploit this feature to avoid generating false covariance peaks. For example, an inner product between a pair of array consisting of non-negative signals (the magnitude processing signals) always results positive values even with their partial overlaps. This depicts the generation of false covariance correlation encountered in HMBC or HSQC spectra in magnitude mode. On the other hands, the phase-sensitive multiplet structure of mHMBC along the  $F_2$  domain can be expressed by

$$S(t_2, \Delta) = \exp(-R_{2,a}t_2) \cdot \prod_{k=1}^N \{ \cos(\pi J_{ak}2\Delta) \cos(\pi J_{ak}t_2) + \sin(\pi J_{ak}2\Delta) \sin(\pi J_{ak}t_2) \}$$

where  $J_{ak}$  is the  $J$ -coupling constant between proton spin  $I_a$  and  $I_k$

$$\hat{H}_0 = 2\pi J_{ak} \sum_{k=1}^N \hat{I}_{z,a} \hat{I}_{z,k} \quad \text{and} \quad \frac{d\langle \hat{I}_- \rangle}{dt} = -i[\hat{I}_-, \hat{H}_0]$$

Then, the real part of the Fourier transformation of  $S(t_2, \Delta)$  is given by

$$S_{\text{Real}}(\omega, \Delta) = S_{\text{Real}}^1 * S_{\text{Real}}^2 * \dots * S_{\text{Real}}^N$$

where  $S^1 * S^2$  is the convolution of  $S^1$  and  $S^2$

and

$$S_{\text{Real}}^k(\omega, \Delta) = \underbrace{\frac{\cos(\pi J_{ak}2\Delta) \cdot R_{2(a)}^2}{(\pi J_{ak} \mp \omega)^2 + R_{2,a}^2}}_{\text{Absorptive in-phase}} - \underbrace{\frac{\sin(\pi J_{ak}2\Delta) \cdot (\pi J_{ak} \mp \omega)}{(\pi J_{ak} \mp \omega)^2 + R_{2,a}^2}}_{\text{Dispersive anti-phase}}$$



Since  $J_{\text{CH}}$ -modulation had been removed in the mHMBC spectrum, the equation shows that each the multiplet structure on  $F_2$  domain of mHMBC spectrum is the product of sequence which is combination of absorptive in-phase and dispersive anti-phase only according to  $J_{\text{HH}}$  constant and their ratio is roughly depends on the total length of HMBC pulse sequence. Even though the chemical shift of two proton signals of different molecules, therefore, are completely overlapped, each  $J$ -coupling components may differ depends on chemical environment in molecules. In summary, the phase-sensitive processing on mHMBC conserved the mixed-phase multiple signals in the  $F_2$  domain arising from the  $J_{\text{HH}}$  that is active throughout of the pulse sequence. Thus, an inner product between signal arrays whose multiplet structures are identical will give always positive values, whereas signal arrays have different multiplet structure will lead to near-zero values depending on relative patterns thereof. For singlet protons which do not interact with other protons and shows only absorptive in-phase signal, the spectral derivative<sup>80</sup> or the phase correction of  $F_2$  domain out-of-90° also yield similar phase factors. The partial derivative (spectral derivative) of absorptive in-phase signals is similar to the form of dispersive anti-phase signals shown as below

$$\frac{\partial}{\partial \omega} \left( \frac{R_{2,a}}{\omega^2 + R_{2,a}^2} \right) = - \frac{2 \cdot R_{2,a}^2 \cdot \omega}{(\omega^2 + R_{2,a}^2)^2}$$

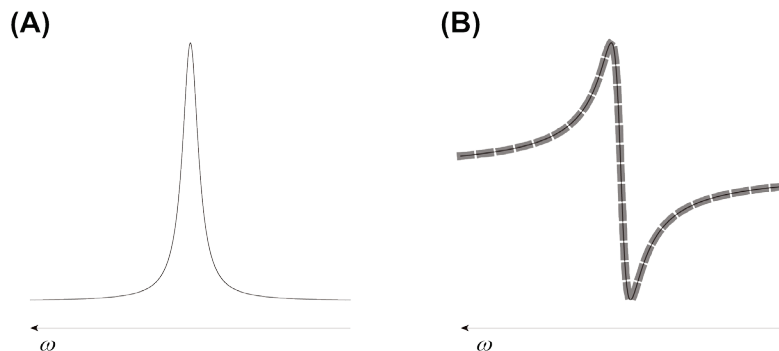


**Figure 3.8 Comparison of 1D NMR signal and its spectral derivative**

(A) Absorptive Lorentzian line shape. (B) Solid line: the spectral derivative of (A), Dashed line: dispersive Lorentzian line shape. Solid line:  $-90^\circ$ -phase shift of (A).

Moreover, any partial derivative in the direction  $\omega$ , does not affect homogeneity of multiplet structures within the same group and preserves their relative first spectral moments. Thus, a group of HMBc cross peaks correlated with a particular proton will inherit the same multiplet structure of proton signal. This can essentially suppress spurious correlation peaks between exactly overlapping protons with different mixed-phase multiplets. Note that the important constraint of this approach is the total length of each pulse sequence  $\Delta$  should be identical each other. In case of the  $J$ -modulation based overlap filter, the spectral derivative of  $\mathbf{H}$ , instead of the absolute value matrix in 2.8.2, should be used as below

$$W_{ij} = \sum_{k=1}^n D_{ik} \cdot D_{jk} \cdot f(\mu_{ik} - \mu_{jk})$$

where  $\mathbf{D}$  is the spectral derivative of  $\mathbf{H}$  along the  $F_2$  domain.

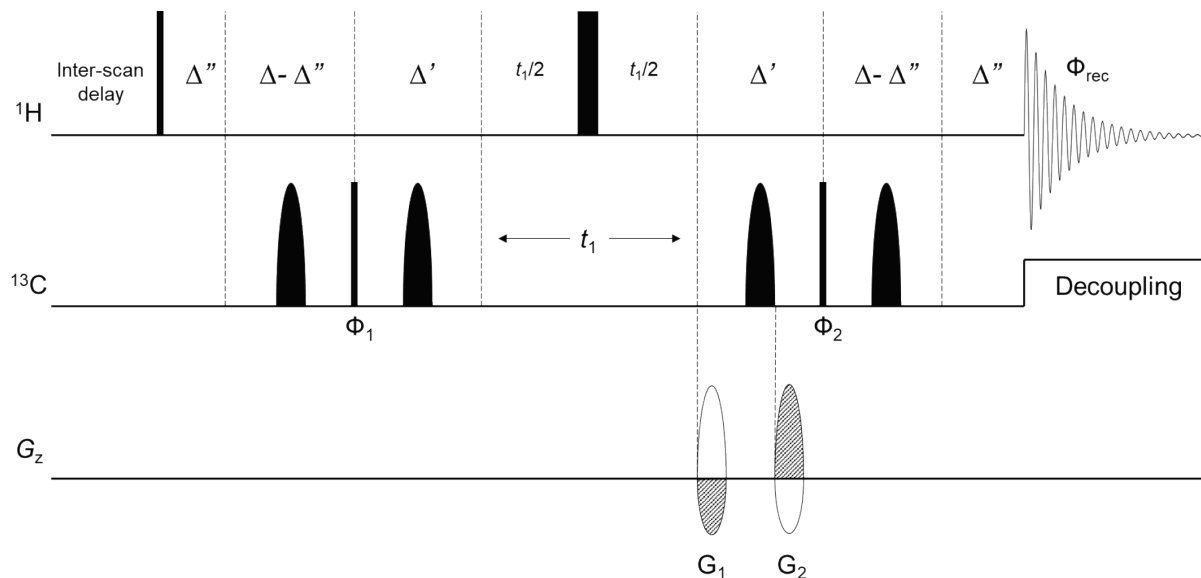


**Figure 3.9** Pulse sequence for mHMBC with  $J$ -modulation filter

Pulse sequences for mHMBC for multiple bond correlation which has the same  $J_{\text{HH}}$  modulation as mHMBC. For sucrose/quinic acid mixture for  $J$ -modulation filter. The delay  $\Delta''$  was set to 3.45 ms for HSQC-type one-bond correlation. The semi-ellipsoid boxes represent  $180^\circ$  shaped pulses for inversion or refocusing of  $^{13}\text{C}$  magnetization. Narrow and wide bars represent  $90^\circ$  and  $180^\circ$  hard pulses, respectively. For the phase-sensitive acquisition in the indirect domain, an echo-antiecho detection mode was employed. Phases of  $\Phi_1$  and  $\Phi_{\text{rec}}$  were shifted by  $180^\circ$  at every even-numbered increment. Blank semi-ellipsoid boxes in the gradient channel represent gradient pulses for odd-numbered increments and gray semi-ellipsoid boxes for even-numbered increments. All pulses are of phase,  $x$  unless otherwise indicated. The phase cycling is as follows.  $\Phi_1 = x, -x$ ;  $\Phi_2 = -x, -x, x, x$ ;  $\Phi_{\text{rec}} = -x, x, x, -x$ . Gradient ratios:  $G_1 : G_2 = 5 : -3$  (odd-numbered) and  $-3 : 5$  (even-numbered).

## 3.9 Experimental section

### 3.9.1 NMR measurements

For NUS, the actual time-domain points were  $2048 \times 72$  ( $t_2 \times t_1$ ) complex points with the final  $4096 \times 8192$  ( $t_2 \times t_1$ ) complex points after NUS reconstruction and zero-filling processing. The spectral width was  $10204 \times 49174$  Hz ( $F_2 \times F_1$ ) and frequency offsets were 4251 Hz and 23516 Hz for  $^1\text{H}$  and  $^{13}\text{C}$  nuclei, respectively. For the mHMBC (delay  $\Delta$ : 62.5 ms) of the mixture of brucine and rotenone, the number of scans was 4 and the total experiment time was about 13 min. For the long-range mHMBC ( $^nJ_{\text{CH}} = 4$  Hz; delay  $\Delta$ : 125 ms), the number of scans was 8 and the total experiment time was 29 min. For the HSQC experiment, all the parameters, except for the pulse sequence specific parameters and the number of scans (2 scans), were matched with those for the HMBC experiment and the total experiment time was 9 min. For the mHMBC (delay  $\Delta$ : 62.5 ms) of the mixture of sucrose and quinic acid, the number of scans was 32 and the total experiment time was about 1 hr 46 min. For the one-bond correlation spectrum, equivalent to HSQC, the pulse sequence in Figure-S1B was used to get the same  $J_{\text{HH}}$  modulation as in mHMBC. There, the delay  $\Delta''$  was set to 3.45 ms, identical to the evolution delay of HSQC experiment. The number of scans and the total experiment time was the same as above.

### 3.9.2 DECODE processing

For the DECODE processing, a home-built processing script base on python 3.6 was developed. A module for python nmrglue<sup>81</sup> was used for input and output of nmripe format data.

### 3.10 Results and discussion

The first step is the combining of two-type of mHMBC and HSQC spectra to compensate inhomogeneity of polarization transfer efficiency attributed to fixed INEPT delay of in a single pulse sequence. INEPT delays  $\Delta$  were chosen to 62.5, 125 and 3.45 ms which were optimized for 8, 4 and 145 Hz of  $^nJ_{CH}$  coupling constant value respectively. As shown in Figure 2.10A and B, this spectral merging gives rise to more expected correlation signals on the indirect covariance spectrum, especially those for the isolated spin groups such as methoxy carbon signals. Figure 2.10C and D shows the effect of the spectral moment filtering to avoid a generation of spurious intra/intermolecular peak from covariance operation between false overlapped signal arrays. The spurious intermolecular correlation peaks between rotenone and brucine were suppressed (Figure 2.10D; around 45 ppm) after employing first-moment filter. After third and fourth processing steps, the dataset normalization and peak digitization, undesirable peak ridge around the strong peaks was removed and the disproportionality of covariance signal intensity was also improved (Figure 2.11A-C). Figure 2.12 shows complete spectral deconvolution and extraction of pure  $^{13}\text{C}$  spectra from mixture of rotenone and brucine. All the 23 carbon signals were identified in each extracted  $^{13}\text{C}$  spectrum without any entanglement from the other compound. whereas the previous PCA-based Demix<sup>4</sup> approach failed to extract genuine  $^{13}\text{C}$  spectrum of each. Of note, DECODE processing also enabled a separation of carbon signals spaced at just 0.06 ppm interval. (Figure 2.13) It is because of the sufficient signal resolution of template NUS-iCov spectrum and the peak digitization processing with the mixture  $^{13}\text{C}$  spectrum as a reference spectrum. Note that the spectral resolution (SW/TD) of the iCov spectrum should be adjusted according to minimum frequency difference carbon signals. Fortunately, one can easily estimate it prior to DECODE processing by analyzing the  $^{13}\text{C}$  spectrum of mixture sample. In addition,

the effect of  $J$ -modulation filter was demonstrated on a mixture of sucrose and quinic acid (Figure 2.14 and 15), with the former having notoriously congested proton signals in the 4.2 to 3.2 ppm region. In addition, its two signals at  $\delta_{\text{H}}$  3.95 and 3.45 completely overlapped with the proton signals of quinic acid (Figure 2.14A). Without the  $J$ -modulation filter, the carbon peaks from sucrose spilled into the quinic acid spectrum upon the DECODE procedure (Figure 2.15A), which was effectively suppressed by the use of  $J$ -modulation (Figure 2.15B). Therefore, this optional  $J$ -modulation-based filter can be used where proton overlap is severe. In terms of the result validation, in the most of case in analysis in NPs, the number of chemical species in mixture and each of total number of carbon nuclei can be identified using the other analytical technique such as high-resolution LC-MS in advance of DECODE analysis. Since the inflection point value of sigmoid function is crucial factor of DECODE result, one can verify and improve the result, adjusting the inflection point, by comparing with the true number of carbon nuclei information.

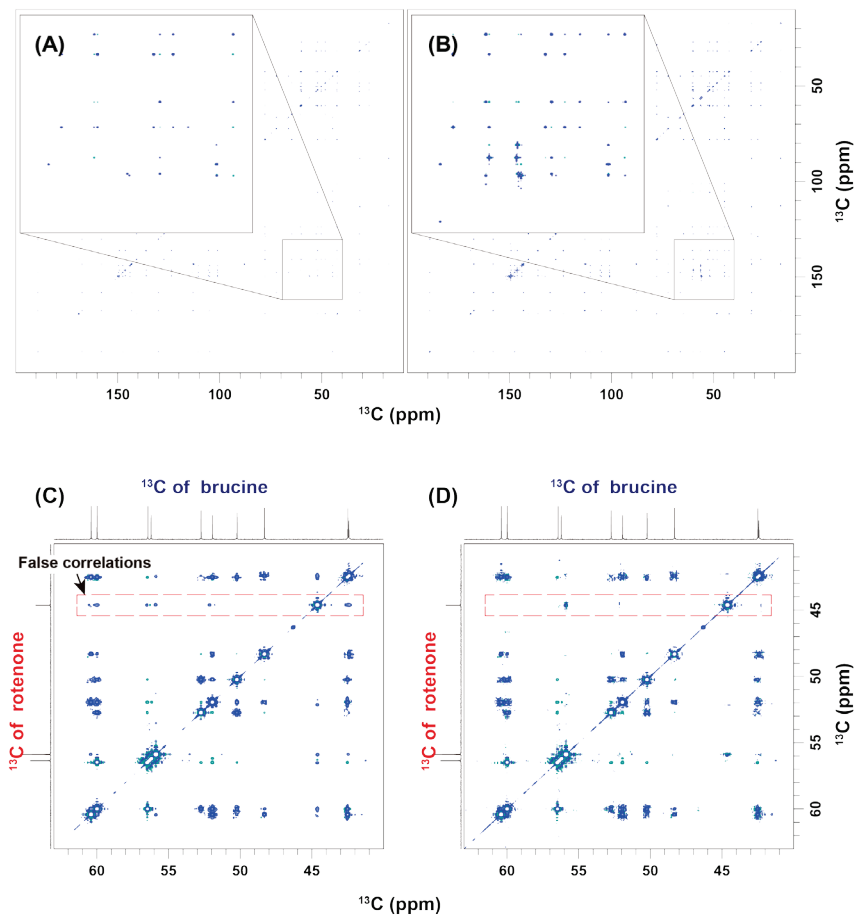


**Figure 3.10** The effects of spectral merging and spectral moment filter

The effects of the spectral merging and the first spectral moment filter on the iCov spectrum of the mixture of rotenone and brucine. (A and B) iCov spectra without (A) and with (B) the spectrum merge. (C and D) iCov spectra without (C) and with (D) the spectral-moment filter (the first moment). The vertical trace is the  $^{13}\text{C}$  spectrum of rotenone and the horizontal trace is the  $^{13}\text{C}$  spectrum of brucine. The dashed box indicates false-positive intermolecular peaks between rotenone and brucine.

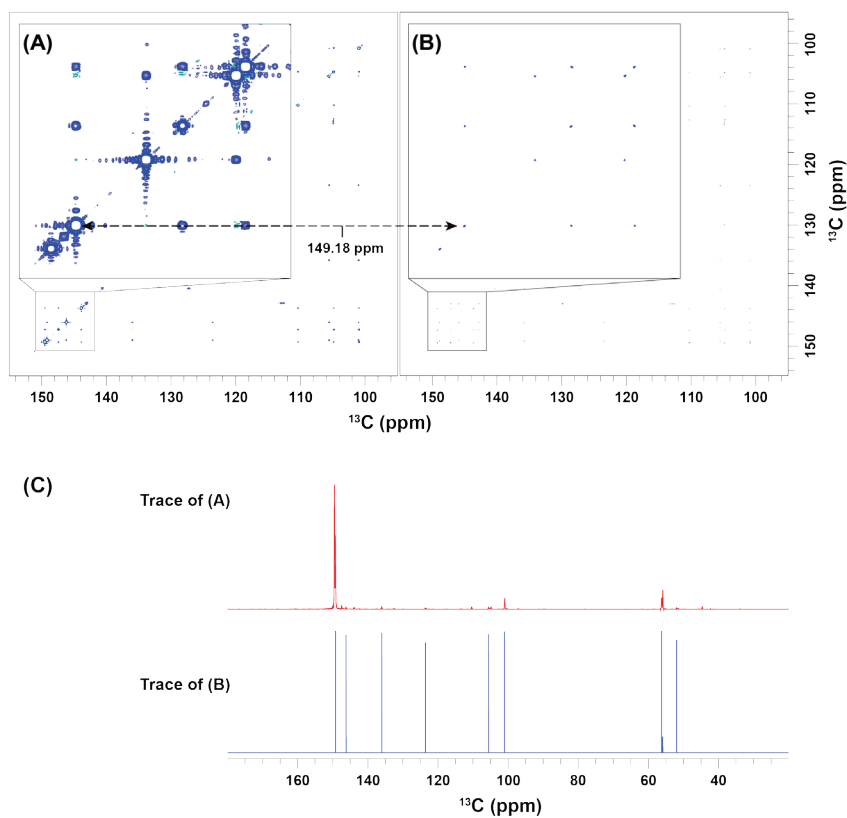


**Figure 3.11** The effects of signal normalization and peak digitization

The effects of signal normalization and peak digitization on the iCov spectrum of the mixture of rotenone and brucine. (A and B) iCov spectra without (E) and with (F) signal normalization and peak digitization. The dashed double arrow indicates peaks in each spectrum at 149.18 ppm. (C) The traces at 149.18 ppm of (A) (Top) and (B) (Bottom).



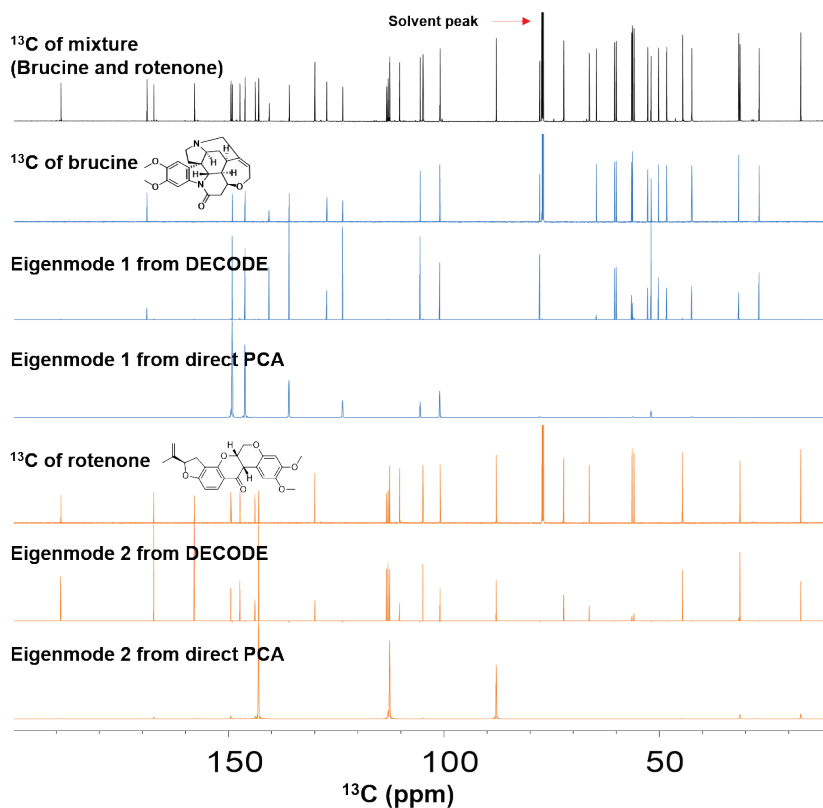


**Figure 3.12 Results of DECODE**

Extraction of the individual spectra of rotenone and brucine from the mixture by DECODE. The top spectrum is the  $^{13}\text{C}$  spectrum of the mixture. Below the  $^{13}\text{C}$  spectrum, from top to bottom: the  $^{13}\text{C}$  spectrum of the single compound, the eigenmode from the DECODE and the eigenmode of the direct PCA without DECODE, respectively. The direct PCA results are eigenvectors of the single NUS-mHMBC-iCov spectrum without DECODE. During the DECODE, the inflection point of the sigmoid function,  $\delta$ , was set to 1.58 and the threshold value of the  $^{13}\text{C}$  spectrum to  $10^7$ .

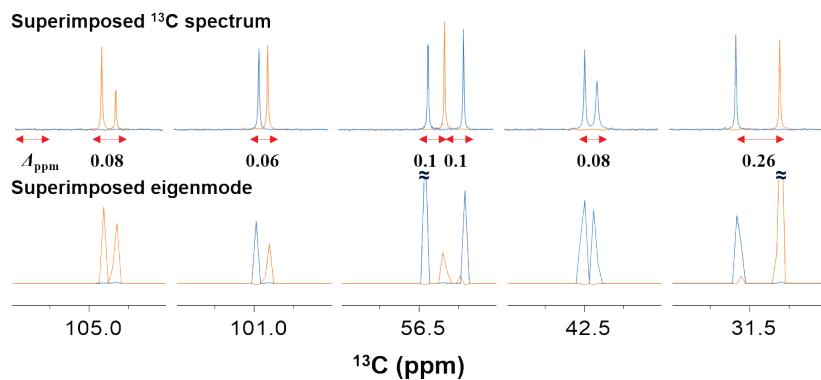


**Figure 3.13 Expansions of DECODE results**

Resolution of very close peaks by DECODE. Superimposed  $^{13}\text{C}$  spectra of brucine and rotenone (Top) and superimposed eigenmode spectra from the DECODE (Bottom).

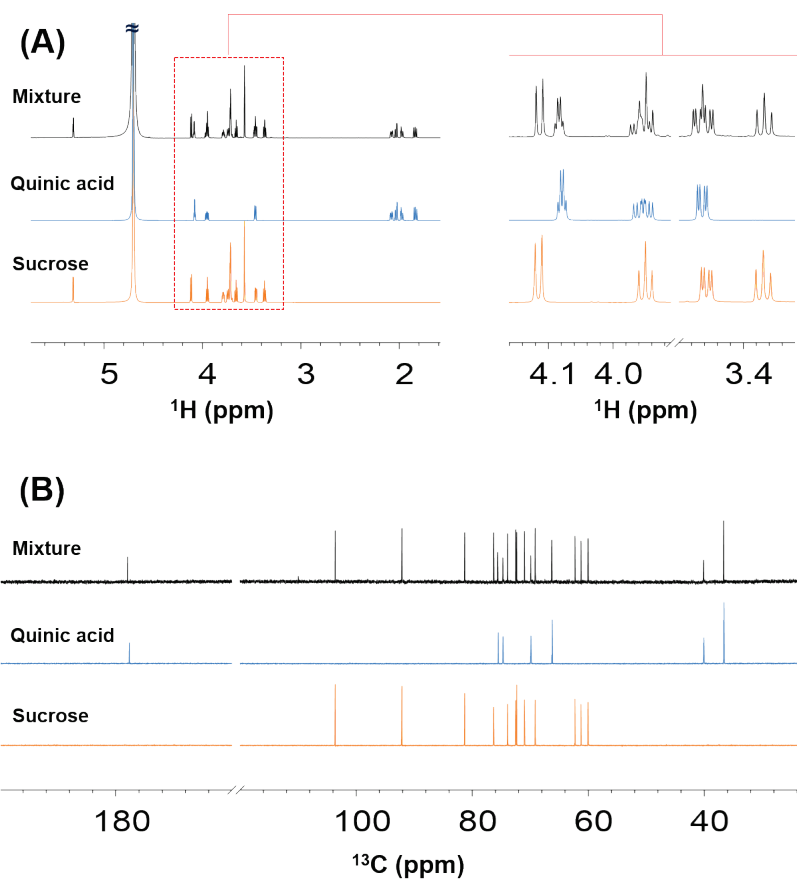


**Figure 3.14** NMR spectra of mixture of sucrose and quinic acid

(A)  $^1\text{H}$  Spectra of sucrose, (Bottom), quinic acid (Middle) and their mixture (Top). (B)  $^{13}\text{C}$  spectra of sucrose (Bottom), quinic acid (Middle) and their mixture (Top).

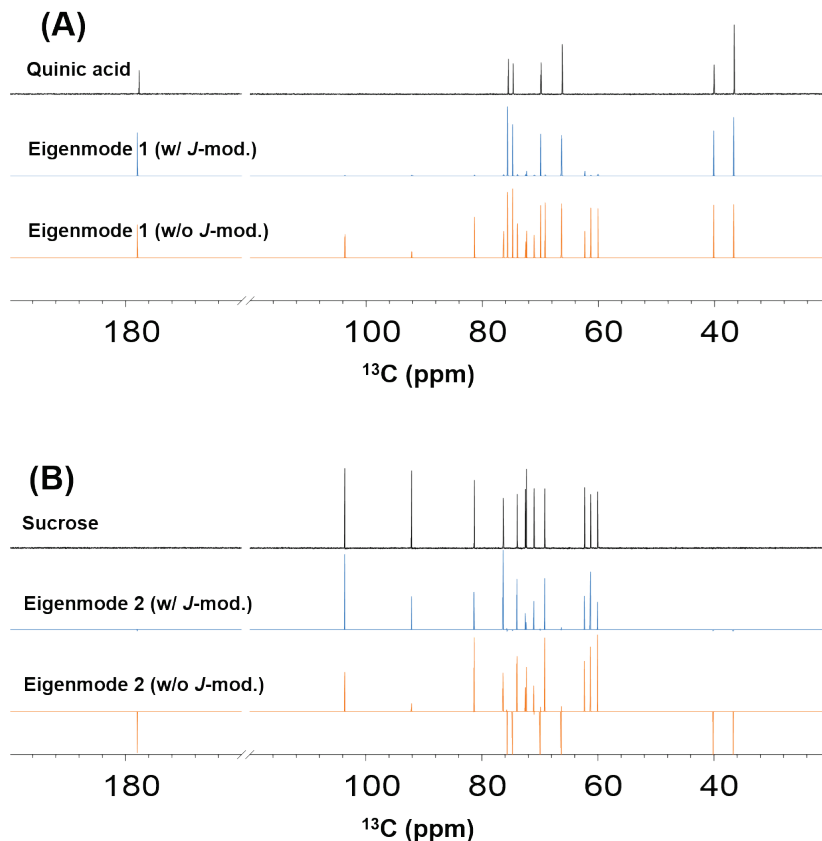


**Figure 3.15 Comparison of DECODE with/without  $J$ -modulation filter**

Comparison of the DECODE result with and without the  $J$ -modulation filter. From top to bottom, the  $^{13}\text{C}$  spectrum of the single compound, the eigenmode from the DECODE with and without the  $J$ -modulation, respectively. (A) is for quinic acid and (B) is for sucrose. For this, merging of one mHMBC ( $^nJ_{\text{CH}} = 8$  Hz) and another one bond correlation spectrum (Figure 2.9) with the same total pulse duration were enough (total of 2 experiments rather than 3). During the DECODE, the inflection point of the sigmoid function,  $\delta$ , was set to 1.37 and the threshold value of  $^{13}\text{C}$  spectrum to  $2 \times 10^6$ .

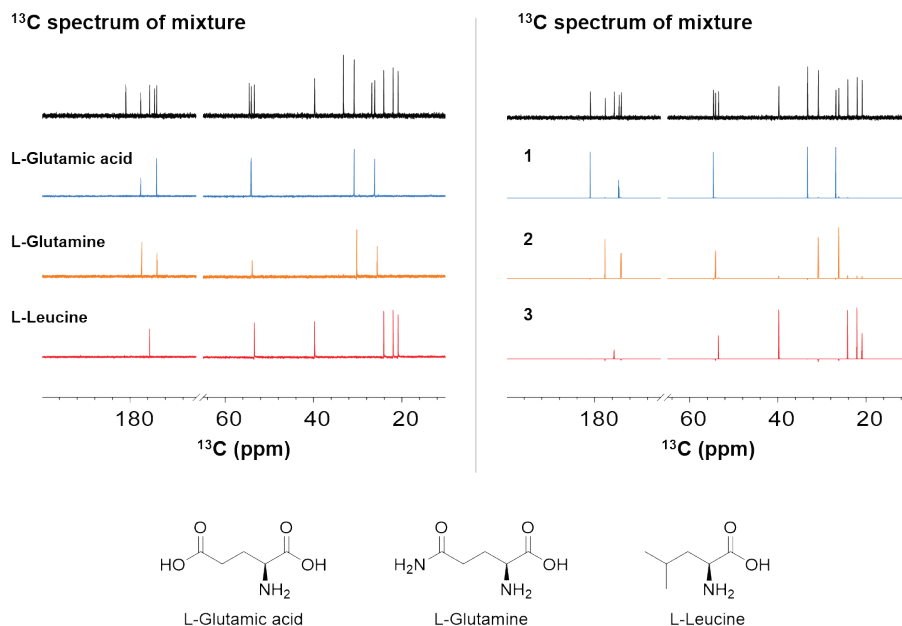


**Figure 3.16 DECODE results for three amino acids mixture**

(Left)  $^{13}\text{C}$  NMR spectrum of mixture and individual  $^{13}\text{C}$  NMR spectra. (Right)  $^{13}\text{C}$  NMR spectrum of mixture and eigenmodes from DECODE; Lower insets are structures of L-glutamic acid, L-glutamine and L-leucine.

### **3.11 Conclusion**

Herein, we showed that a high-resolution  $^{13}\text{C}$ - $^{13}\text{C}$  correlation spectrum of a compound with many quaternary carbons can be obtained with proton sensitivity using NUS-mHMBC-iCov. With the thus-obtained complete molecule-wide spin network, an optimized signal-processing procedure (DECODE) was developed for the extraction of individual carbon spectra from mixture data. We tested the performance of the deconvolution with the 1:1 mixture intentionally, as it should be the most challenging case. A mixture with a large concentration difference, for example a 1:20 mixture, should be easier to deconvolute because the signal intensity differences are correlated within a single compound and a clear distinction between signal groups that may be apparent to even to eye examination. Still, the lower-fraction component may suffer low signal to noise ratio due to the limited receiver dynamic range. For this, we incorporated the normalization step in the DECODE procedure, and it should help the analysis of the low-signal-to noise component to some extent. Essentially, our approaches can provide usable 1D carbon spectrum(a) for a single compound or individual species in a mixture from 2D  $^1\text{H}$ - $^{13}\text{C}$  correlation spectroscopy.

Our approach should be straightforwardly used with more common 500 or 600 MHz spectrometers, as long as proton overlaps are not significantly higher in those fields. As we obtained the spectrum of rotenone with a 2 mg sample for 2 hours at 800 MHz, theoretically, the same signal to noise ratio can be obtained with four times of the acquisition time (8 hours) which is a very practical time frame. Currently, there is a limitation for our approach in dealing a complex mixture with a large number of components, and at this point, it is not intended for or have not been tested with a crude extract. The benefit will be the largest at the final purification step with two or three hard-to-separate components, which actually is not very uncommon. Overall,

the described approaches should prove useful in various fields of chemistry and may be adapted to computer-assisted structure elucidation (CASE)<sup>82</sup>.

## Chapter 3

### 4 $^{13}\text{C}$ - $^{13}\text{C}$ distortion-free $J$ -scaled HSQC



## 4.1 Introduction

Recent advances in high-resolution NMR spectrometers have enabled the measurement of high-resolution NMR signals in both direct and indirect domains in many  $n$ D NMR experiments. Nevertheless, for nuclei with a wider range of chemical shift than  $^1\text{H}$ , such as  $^{13}\text{C}$ , it is still difficult to obtain signals of resolution levels of several Hz in the indirect domain. Meanwhile, regarding the reduction of experiment time in  $n$ D NMR experiments, the non-uniform sampling (NUS) technique has proven its effectiveness thereby, is widely used within the NMR community<sup>53,56</sup>. However, due to a special signal reconstruction procedure different from the conventional Fourier transform method<sup>73,83,84,85,86,87</sup>, general NUS techniques are not proper to quantitative analysis<sup>88</sup>, and these constraints limit the use of NUS techniques in the study of metabolic flux analysis. On the other hands, for the cellular metabolic analysis based on NMR spectroscopy  $^{13}\text{C}$  stable-isotope labeled compounds were widely employed to address low sensitivity problems on account of the low natural abundance and low gyromagnetic ratio of  $^{13}\text{C}$  nucleus<sup>89</sup>. Together with the obtained high-sensitivity  $^{13}\text{C}$  NMR signal, a specific  $J_{\text{CC}}$ -coupling pattern due to  $^{13}\text{C}$ - $^{13}\text{C}$  coupling interaction has been also exploited as an metabolic tracer in NMR metabolomics<sup>7,8,9</sup>. In general, the HSQC spectrum of samples treated with  $^{13}\text{C}$  isotope shows a sparse NMR signal distribution due to selective sensitivity enhancement associated with a particular metabolic pathway even at ordinary indirect domain sampling points. But, for the  $J$ -coupling analysis in HSQC, it is hard to extract coupling information such as splitting pattern or exact  $J_{\text{CC}}$  coupling constant on account of the poor resolution and the signal distortion.

Thus, the analysis of  $J_{\text{CC}}$  coupling was done mainly through the 1D  $^{13}\text{C}$  acquisition with a poor sensitivity than HSQC or the  $^1\text{H}$ - $^1\text{H}$  TOCSY indicating a complex signal distribution. Therefore,  $J$ -scaling techniques,<sup>12,13,14</sup> which only amplify the

effects of  $^{13}\text{C}$ - $^{13}\text{C}$  interactions while maintaining the total number of sample points of the indirect domain, will be highly applicable to these NMR-based metabolic analysis studies. Meanwhile, the effects of signal distortion by  $^{13}\text{C}$ - $^{13}\text{C}$  interaction on two-dimensional NMR measurements of  $^{13}\text{C}$  isotope has been discussed in several studies. Thereby, the elimination of signal distortion of HSQC signals by  $^{13}\text{C}$  isotope labeled compounds and the selective amplification of  $^{13}\text{C}$ - $^{13}\text{C}$  interaction effects through the application of  $J$ -scaling technique were considered in this study. To this end, an analytical expression of HSQC signal distortion was derived for the conventional HSQC sequence using  $^{13}\text{C}$  isotope compounds and, to address this, a novel pure-in-phase HSQC sequence for the  $^{13}\text{C}$  isotope labeled compound was proposed.

## 4.2 Origin of the HSQC signal distortion by $J_{CC}$ -coupling

It has been generally known that the undesirable signal distortion along the indirect domain of  $nD$  NMR spectrum for the  $^{13}\text{C}$ -isotope labeled compound<sup>10,11</sup>. The origins of this signal distortion can be regarded as on account of a polarization transfer of  $^{13}\text{C}$ - $^{13}\text{C}$   $J$ -coupling modulated signal  $S(t_1)$  during the  $t_1$ -evolution period.  $J$ -modulated signal has both cosine and sine modulated coupling terms and according to the combination of these two trigonometric function terms, the signal distortion will be generated along the indirect domain. In a more explicit expression, a constant delay, not the  $t_1$ -variable incremental delay, during the  $t_1$ -evolution period will generate sine modulated  $J$ -coupling term (an origin of the dispersive anti-phase signal) which can be further transferred to observable signal. For the non- $^{13}\text{C}$ -isotope labeled compound, as the natural abundance of  $^{13}\text{C}$  nucleus is very low, their  $^{13}\text{C}$ - $^{13}\text{C}$  interaction is can be neglected, as for whereas the uniformly  $^{13}\text{C}$ -labeled compounds, which are frequently employed in cellular metabolomics study then the effect from  $^{13}\text{C}$ - $^{13}\text{C}$  interaction will be arisen.

### 4.2.1 Evolution of $J$ -couplings during finite length of delays

As describe above, the dispersive anti-phase signal term along the indirect domain is originated from an additional  $J_{CC}$  evolution during the finite length of adiabatic pulses, gradient pulses and couple of delays.

Assuming two weakly coupled carbon spin  $S_1$  and  $S_2$ , at the end of  $t_1$ -evolution period, the product operator has following forms,

$$-2\hat{S}_{1y}\hat{I}_z \xrightarrow{\Omega_1(\hat{S}_{1z}+\hat{S}_{2z})t_1+2\pi J_{12}\hat{S}_{1z}\hat{S}_{2z}t_1} -2\hat{I}_z\{\hat{S}_{1y}\cos(\Omega_1 t_1)\cos(\pi J_{12} t_1) - 2\hat{S}_{1x}\hat{S}_{2z}\cos(\Omega_1 t_1)\sin(\pi J_{12} t_1) - \hat{S}_{1x}\sin(\Omega_1 t_1)\cos(\pi J_{12} t_1) - 2\hat{S}_{1y}\hat{S}_{2z}\sin(\Omega_1 t_1)\sin(\pi J_{12} t_1)\}$$

After applying a  $\pi/2$ -rotation pulse,  $F_\gamma (= \sum_k S_{k\gamma})$ , any two spin anti-phase product operator of two  $J$ -coupled carbon spins  $2\hat{S}_{1\gamma}\hat{S}_{2z}$  ( $\gamma = x$  or  $y$ ) are converted to multiple-quantum (MQ) state product operators ( $2\hat{S}_{1x}\hat{S}_{2y}$  or  $2\hat{S}_{1y}\hat{S}_{2x}$ ) and this MQ state of carbon spins cannot be contributed to observable state during the rest of the pulse sequence. Thus, only observable operator forms are cosine modulated coupling terms.

$$-2\hat{I}_z\hat{S}_{1y}\cos(\Omega_1 t_1)\cos(\pi J_{12} t_1) + 2\hat{I}_z\hat{S}_{1x}\sin(\Omega_1 t_1)\cos(\pi J_{12} t_1)$$

: Observable terms

$$+4\hat{I}_z\hat{S}_{1x}\hat{S}_{2z}\cos(\Omega_1 t_1)\sin(\pi J_{12} t_1) + 4\hat{I}_z\hat{S}_{1y}\hat{S}_{2z}\sin(\Omega_1 t_1)\sin(\pi J_{12} t_1)$$

: Unobservable terms

However, an any additional evolution of  $J_{CC}$  coupling can convert the sine modulated anti-phase operator to an in-phase operator for the  $S$  spin.

$$\begin{aligned} 2\hat{S}_{1x}\hat{S}_{2z}\sin(\pi J_{12} t_1) &\xrightarrow{2\pi J_{12}\hat{S}_{1z}\hat{S}_{2z}\Delta} 2\hat{S}_{1x}\hat{S}_{2z}\sin(\pi J_{12} t_1)\cos(\pi J_{12}\Delta) \\ &\quad + \hat{S}_{1y}\sin(\pi J_{12} t_1)\sin(\pi J_{12}\Delta) \\ 2\hat{S}_{1y}\hat{S}_{2z}\sin(\pi J_{12} t_1) &\xrightarrow{2\pi J_{12}\hat{S}_{1z}\hat{S}_{2z}\Delta} 2\hat{S}_{1y}\hat{S}_{2z}\sin(\pi J_{12} t_1)\cos(\pi J_{12}\Delta) \\ &\quad - \hat{S}_{1x}\sin(\pi J_{12} t_1)\sin(\pi J_{12}\Delta) \end{aligned}$$

Then, the second term of the right equation is further converted to observable signals. In summary, any additional  $J_{CC}$  evolution could retain sine modulated  $J_{CC}$  coupling terms in the  $F_1$  domain.

#### 4.2.2 Analysis of NMR signal: AX spin system

In order to evaluate the quantitative effect of the constant delay for the generation of sine modulated  $J_{CC}$ -coupling term during the  $t_1$ -evolution period, a density operator

analysis based on product operator formalism<sup>90</sup> for conventional HSQC pulse sequence has been performed.

Firstly, let us consider a natural abundance <sup>13</sup>C compound. Before the  $t_2$ -acquisition, observable proton spin ( $I$ ) product operators encoded with  $t_1$ -variable from the conventional preservation of equivalent pathway (PEP)<sup>91</sup>-HSQC experiment are as below, (For brevity, relaxation terms are neglected)

$$\begin{aligned} & +\hat{I}_y \cos(\Omega t_1) + \hat{I}_x \sin(\Omega t_1): \text{ Even-numbered TD} \\ & -\hat{I}_y \cos(\Omega t_1) + \hat{I}_x \sin(\Omega t_1): \text{ Odd-numbered TD} \end{aligned}$$

As shown in 3.2.1, on the other hands, for the <sup>13</sup>C-isotope labeled compound, the sine modulated  $J_{CC}$ -coupling terms which is encoded with variable  $t_1$  will be retained as an observable operator form. Since the frequency discrimination method by echo-antiecho acquisition<sup>68,69</sup> acquires two parallel indirect domain signals which has different coherence order as below

Even-numbered TD ( $P$ -type spectrum):

$$\begin{aligned} & -\hat{I}_y \cos(\Omega t_1) \cos(\pi J_{12} t_1) \cos(\pi J_{12} \Delta_t) \\ & + \hat{I}_x \sin(\Omega t_1) \cos(\pi J_{12} t_1) \cos(\pi J_{12} \Delta_t) \cos(\pi J_{12} \Delta_2) \\ & + \hat{I}_y \cos(\Omega t_1) \sin(\pi J_{12} t_1) \sin(\pi J_{12} \Delta_t) \\ & - \hat{I}_x \sin(\Omega t_1) \sin(\pi J_{12} t_1) \sin(\pi J_{12} \Delta_t) \cos(\pi J_{12} \Delta_2) \end{aligned}$$

Odd-numbered TD ( $N$ -type spectrum):

$$\begin{aligned} & +\hat{I}_y \cos(\Omega t_1) \cos(\pi J_{12} t_1) \cos(\pi J_{12} \Delta_t) \\ & + \hat{I}_x \sin(\Omega t_1) \cos(\pi J_{12} t_1) \cos(\pi J_{12} \Delta_t) \cos(\pi J_{12} \Delta_2) \\ & - \hat{I}_y \cos(\Omega t_1) \sin(\pi J_{12} t_1) \sin(\pi J_{12} \Delta_t) \\ & - \hat{I}_x \sin(\Omega t_1) \sin(\pi J_{12} t_1) \sin(\pi J_{12} \Delta_t) \cos(\pi J_{12} \Delta_2) \end{aligned}$$

Then, acquired two *P*-type (Anti-echo) and *N*-type (Echo) signals followed by “Rance-Kay”<sup>91,92</sup> processing or sum of *P*-type and complex conjugate of *N*-type<sup>68,69</sup> result in signal  $S(t_1, \Omega_2)$  consist of two types of signals, absorptive in-phase signal,  $S_{\text{AIP}}$ , and dispersive anti-phase signal,  $S_{\text{DAP}}$ .

$$\begin{aligned}
 S_{\text{AIP}}(t_1, \Omega_2) &= +A_2 \{ \exp(i\Omega t_1) \cos(\pi J_{12} t_1) \cos(\pi J_{12} \Delta_t) \\
 &\quad + \exp(i\Omega t_1) \cos(\pi J_{12} t_1) \cos(\pi J_{12} \Delta_t) \cos(\pi J_{12} \Delta_2) \} / 2 \\
 &= +A_2 [ \exp(i\Omega t_1) \cos(\pi J_{12} t_1) \cos(\pi J_{12} \Delta_t) \{ 1 + \cos(\pi J_{12} \Delta_2) \} ] / 2 \\
 &= +A_2 \exp(i\Omega t_1) \cos(\pi J_{12} t_1) \cos(\pi J_{12} \Delta_t) \cos^2(\pi J_{12} / 2 \Delta_2) \\
 &= +A_2 \exp\{ i(\Omega \pm \pi J_{12}) t_1 \} \cos(\pi J_{12} \Delta_t) \cos^2(\pi J_{12} / 2 \Delta_2) / 2 \\
 \\
 S_{\text{DAP}}(t_1, \Omega_2) &= -A_2 \{ \exp(i\Omega t_1) \sin(\pi J_{12} t_1) \sin(\pi J_{12} \Delta_t) \\
 &\quad + \exp(i\Omega t_1) \sin(\pi J_{12} t_1) \sin(\pi J_{12} \Delta_t) \cos(\pi J_{12} \Delta_2) \} / 2 \\
 &= -A_2 [ \exp(i\Omega t_1) \sin(\pi J_{12} t_1) \sin(\pi J_{12} \Delta_t) \{ 1 + \cos(\pi J_{12} \Delta_2) \} ] / 2 \\
 &= -A_2 \exp(i\Omega t_1) \sin(\pi J_{12} t_1) \sin(\pi J_{12} \Delta_t) \cos^2(\pi J_{12} / 2 \Delta_2) \\
 &= \pm i A_2 \exp\{ i(\Omega \pm \pi J_{12}) t_1 \} \sin(\pi J_{12} \Delta_t) \cos^2(\pi J_{12} / 2 \Delta_2) / 2
 \end{aligned}$$

where  $A_2$  is the absorptive real part signal of the  $^1\text{H}$  spin.

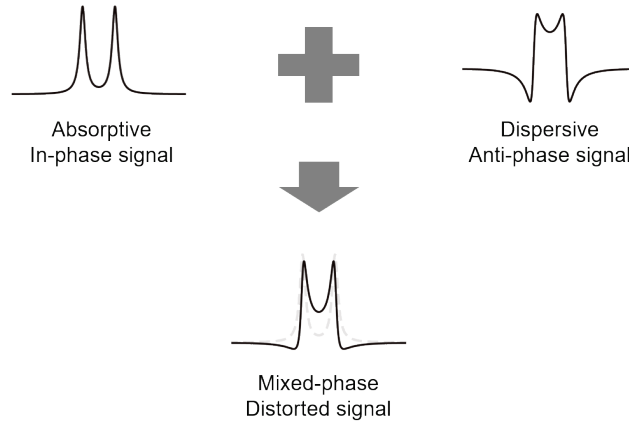


**Figure 4.1 Origin of the signal distortion**

Schematic description of signal distortion due to combination of absorptive In-phase and dispersive anti-phase signal.

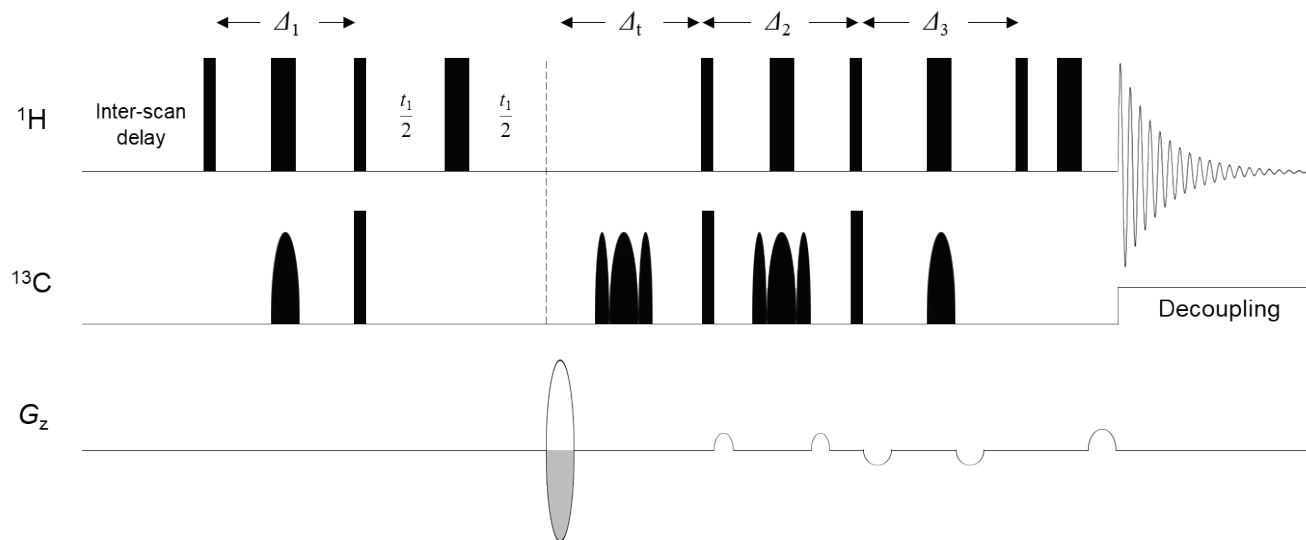


**Figure 4.2** Pulse sequence of ge-ps-PEP-HSQC

Schematic diagram of gradient enhanced phase-sensitive PEP adiabatic inversion HSQC (ge-ps-PEP-HSQC) pulse sequence (from bruker pulse sequence library 'hsqcetgpsisp2.2');  $\Delta_t$ : evolution delay sum of composite adiabatic pulse and gradient pulses and its delay during the  $t_1$ -evolution period;  $\Delta_2$ : the first reverse INEPT delay which is equivalent to the additional evolution delay during PEP pathway;  $\Omega$ : the chemical shift of carbon spin and  $J_{12}$  is the  $^{13}\text{C}$ - $^{13}\text{C}$  homonuclear scalar coupling constant of AX spins and assumed that all delays ( $\Delta_1$ ,  $\Delta_2$  and  $\Delta_3$ ) in INEPT and reverse INEPTs are identical to  $1/2J_{\text{CH}}$  which means  $\sin(\pi J_{\text{CH}}\Delta_n) = 1$ ; where  $n = 1, 2$  and  $3$ ).

### 4.2.3 Analysis of NMR signal: A general case

The general form of HSQC signal with  $n$ -spin system is given by

$$S(t_1, \omega_2) = \frac{1}{2^{n-1}} A_2 \exp(i\Omega t_1) \cdot \prod_{k=2}^n [\{1 + \cos(\pi J_{1k} \Delta_2)\} \cdot \{\cos(\pi J_{1k} t_1) \cos(\pi J_{1k} \Delta_t) - \sin(\pi J_{1k} t_1) \sin(\pi J_{1k} \Delta_t)\}]$$

Or expressed as a linear combination of AIP signal and DAP signal like as below.

$$\overrightarrow{J_{1k}} = \begin{bmatrix} \text{AIP}_{1k} \\ \text{DAP}_{1k} \end{bmatrix} = \begin{bmatrix} \cos(\pi J_{1k} t_1) \cos(\pi J_{1k} \Delta_t) \\ -\sin(\pi J_{1k} t_1) \sin(\pi J_{1k} \Delta_t) \end{bmatrix}$$

For example, assuming three <sup>13</sup>C-<sup>13</sup>C scalar coupling interactions ( $J_{12}$ ,  $J_{13}$  and  $J_{14}$ ), a general form of <sup>13</sup>C-<sup>13</sup>C scalar coupling modulation in a signal is a kronecker product of individual signal vectors,  $S_{1k}$ .

$$\vec{J} = \frac{1}{2^3} \cdot \overrightarrow{J_{12}} \otimes \overrightarrow{J_{13}} \otimes \overrightarrow{J_{14}} \cdot \prod_{k=2}^4 \{1 + \cos(\pi J_{1k} \Delta_2)\}$$

Thus, the two-dimensional HSQC signal with 4-spin system is given by,

$$\vec{S}(t_1, \omega_2) = \frac{1}{2^3} A_2 \exp(i\Omega t_1) \cdot \prod \{1 + \cos(\pi J_{1k} \Delta_2)\} \cdot \begin{bmatrix} \text{AIP}_{12} \cdot \text{AIP}_{13} \cdot \text{AIP}_{14} \\ \text{AIP}_{12} \cdot \text{DAP}_{13} \cdot \text{AIP}_{14} \\ \text{AIP}_{12} \cdot \text{DAP}_{13} \cdot \text{DAP}_{14} \\ \text{AIP}_{12} \cdot \text{AIP}_{13} \cdot \text{DAP}_{14} \\ \text{DAP}_{12} \cdot \text{AIP}_{13} \cdot \text{AIP}_{14} \\ \text{DAP}_{12} \cdot \text{DAP}_{13} \cdot \text{AIP}_{14} \\ \text{DAP}_{12} \cdot \text{DAP}_{13} \cdot \text{DAP}_{14} \\ \text{DAP}_{12} \cdot \text{AIP}_{13} \cdot \text{DAP}_{14} \end{bmatrix}$$

General form of the signal vector including the relaxation term as follows,

$$\vec{S}(t_1, \omega_2) = \frac{1}{2^{n-1}} A_2 \exp(i\Omega t_1) \cdot \vec{J} \cdot \exp(-R_2 t_1)$$

The analytical solution of HSQC signal shows two important conclusions for the signal distortion in HSQC.



1. Each signal intensity of AIP and DAP is proportional to  $\cos(\pi J_{12}\Delta_t)$  and  $\sin(\pi J_{12}\Delta_t)$  respectively.
2. The delay  $\Delta_2$  which is the first reverse INEPT delay in the PEP module can affect to the total intensity of the HSQC signal as a form of  $\left\{ \frac{1}{2^{n-1}} \Pi_2^n \{1 + \cos(\pi J_{1k}\Delta_2)\} \right\}$ .

Therefore, to acquire  $^{13}\text{C}$ - $^{13}\text{C}$  distortion-free  $F_1$ -pure in-phase HSQC signal, the constant delay,  $\Delta_t$ , should be removed from  $t_1$ -evolution period. Meanwhile, the PEP module has been employed for sensitivity enhancement by factor of  $\sqrt{2}$  in the conventional HSQC acquisition scheme<sup>91</sup>. As for the  $^{13}\text{C}$ -isotope labeled compound, however, the total signal intensity is affected by the coefficient  $\left\{ \frac{1}{2^{n-1}} \Pi_2^n \{1 + \cos(\pi J_{1k}\Delta_2)\} \right\}$ . Since the INEPT delay is usually adjusted for the optimal  $^1J_{\text{CH}}$  transfer efficiency which is generally set to 3.5 ms, a typical  $^1J_{\text{CC}}$  coupling constant value (35-55 Hz) gives rise to decrease of the total signal intensity. Suppose that, for example, AMX spin system in which each of  $J$ -coupling constant  $J_{\text{CC}}$  is 55 Hz then the coefficient is

$$[\{1 + \cos(\pi \cdot 55 \cdot 0.0035)\}/2]^2 \approx 0.8$$

Fortunately, these figures still maintain the sensitivity increase by PEP module. Even in extreme cases, such as for four spin AMPX system with a 55 Hz of  $J_{\text{CC}}$ , the signal increase effect by PEP is only offset.

### 4.3 Experimental section

#### 4.3.1 NMR measurements

All NMR spectra were measured at 298 K with 850 or 800 MHz Bruker Avance III HD spectrometers equipped with 5 mm CPTCI CryoProbes (Bruker BioSpin, Germany). For the U-<sup>13</sup>C acetate and U-<sup>13</sup>C lactate sample, each 1 mM of sample (Sigma-Aldrich, MO, USA) was dissolved in 600  $\mu$ L of deuterium oxide respectively. For conventional HSQC NMR experiments, the pulse sequence in Figure 3.1 was used. For apodization, cosine-squared function ( $F_1$ ) and cosine function ( $F_2$ ) were employed and zero-filling was applied to both dimensions. All spectra were processed in phased mode along the both  $F_1$  and  $F_2$  domain. The actual time-domain points of pulse sequence were  $2048 \times 300$  ( $t_2 \times t_1$ ) complex points with the final  $4096 \times 4096$  ( $t_2 \times t_1$ ) complex points after zero-filling. The spectral width was  $12821 \times 8049$  Hz ( $F_2 \times F_1$ ) and the frequency offsets were 3761 Hz and 5433 Hz for <sup>1</sup>H and <sup>13</sup>C nuclei respectively. For HSQC ( $^1J_{CH} = 145$  Hz; delay  $\Delta$ : 3.45 ms), the number of scans was 2 and the total experiment time was about 12 min. For the NUS acquisition, the NUS time-domain points were  $2048 \times 3000$  complex points with 10% NUS sampling density corresponding to  $2048 \times 300$  ( $t_2 \times t_1$ ) of actual time-domain points complex points and it gives final  $4096 \times 4096$  ( $t_2 \times t_1$ ) complex points after NUS reconstruction and zero-filling.

#### 4.3.2 Simulation of the HSQC signal

Simulated HSQC signal was plotted by home-built python 3.6 script. For the simulation, the equation derived from 3.2.3 was used. In simulated spectrum, <sup>13</sup>C-<sup>13</sup>C coupling constants were set to 57 Hz and 36.5 Hz respectively. Delays  $\Delta_1$  and  $\Delta_2$  were set to 4.4 ms and 4.8 ms respectively. For the Fourier transformation,  $f_{max}$  was

set to 120 Hz and time-domain points were 1024 complex points and  $R_2$  relaxation constant was set to 9.0.

## 4.4 Results

### 4.4.1 Simulation and verification of product operator analysis

It was simulated for verification of signal form derived from density operator analysis and compared by measurement of HSQC signal of actual <sup>13</sup>C isotope labeled compound. To this end, a signal was acquired using HSQC pulse sequence shown in Figure 3.2 using 1 mM of U-<sup>13</sup>C-lactate compared to the simulated signal. The analysis shows that the simulated signal is almost identical to the actual HSQC signals of U-<sup>13</sup>C lactate.

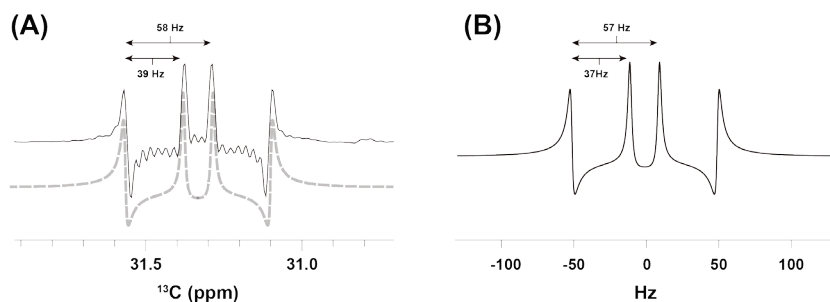


**Figure 4.3 Comparison of actual HSQC and its simulated signal**

(A) Overlay of 1D projection of actual HSQC signal (solid line) and simulated signal (dotted line).

(B) Simulated signal.

## 4.5 Considerations for <sup>13</sup>C-<sup>13</sup>C distortion-free HSQC signal

Therefore, the following sections will discuss considerations in terms of pulse sequence for obtaining HSQC signals without signal distortion due to <sup>13</sup>C-<sup>13</sup>C interaction.

### 4.5.1 Coherence selection by PFG to reduce $t_1$ -noise artefacts

An echo anti-echo frequency discrimination method which introduce a pulse field gradient for coherence selection has been widely used to many of two-dimensional NMR spectroscopic experiments. However, as stated above, any additional delays during the  $t_1$ -evolution period can induce the generation of DAPs. Most of gradient pulse and accompanied delay for avoiding *eddy currents*<sup>93</sup> require hundreds or thousands of microseconds of length. Thereby, with <sup>13</sup>C-isotope labeled samples, the frequency discrimination by PFG in HSQC spectrum is no longer valid. STATES<sup>16</sup>, TPPI<sup>17</sup> or STATE-TPPI<sup>94</sup> acquisition methods are alternative methods can be used for the frequency discrimination without additional constant delays in many two-dimensional NMR experiments. But, contrary to PFG method, those methods give rise to  $t_1$ -noise which arisen from some instrumental imperfections regarding radio-frequency (RF) pulse<sup>95,96</sup>. This  $t_1$ -noise, especially from strong signals, usually hampers analysis of weak signals in *in vivo* or cellular extract samples, generally exhibit low signal-to-noise ratio (SNR). While the coherence-transfer pathway (CTP) selection by phase cycling<sup>18,97</sup> also can be introduced to remove undesired coherences contributing a generation of  $t_1$ -noise, it requires several repetition of experiment to acquire desired coherence, not applicable for many *in vivo* or metabolic samples. To address this problem one can introduce PFG element instead of phase cycling by placing the PFG module before or after the  $t_1$ -evolution period.

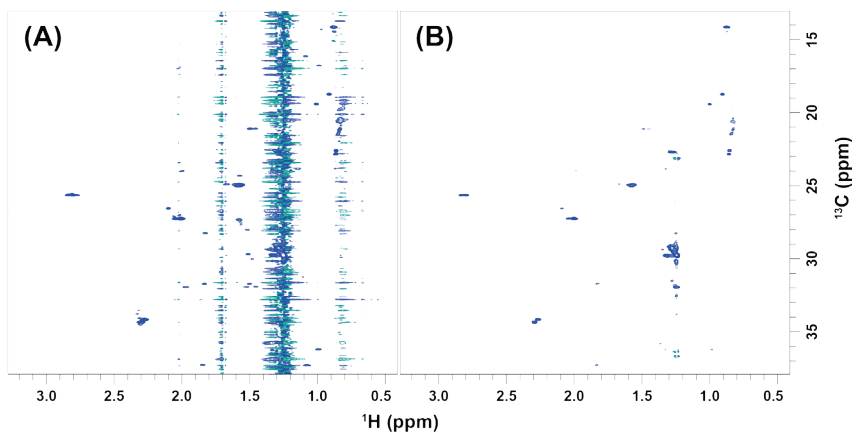


**Figure 4.4 Comparison of HSQC spectra with/without coherence selection by PFG.**

(A) HSQC spectrum with STATE-TPPI frequency discrimination. (B) HSQC spectrum with PFG frequency discrimination.; In here, same NMR acquisition parameters were used except for frequency discrimination method.

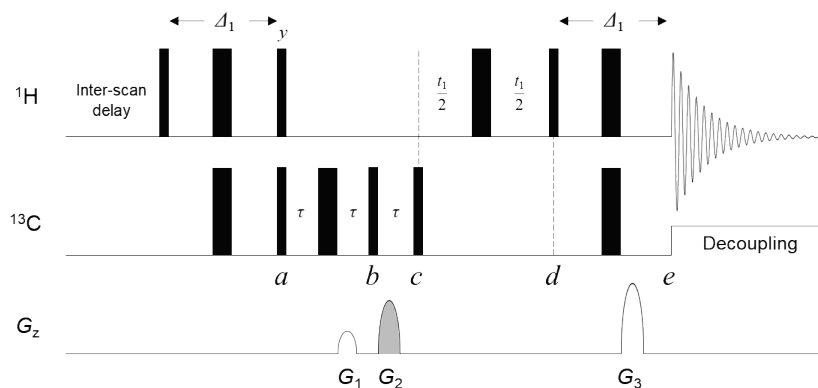


**Figure 4.5 Proposed pulse sequence for HSQC using gradient pulses with coherence selection step outside of the  $t_1$ -evolution period.**

For the frequency discrimination, STATES, TPPI or STATE-TPPI can be used.  $G_1 : G_3 = 4 : 1$  and  $\Delta_1 = \frac{1}{2} J_{CH}$ . Narrow bar indicates an excitation pulse and wide bar indicates an inversion pulse. The semi-ellipsoid shape indicates a gradient pulse.

Assume that, at an equilibrium state, the density operator has a form of  $\hat{I}_z$

Here,  $I$ -spin denotes  $^1\text{H}$  spin and  $S$ -spin denotes  $^{13}\text{C}$  spin.

Then, at a point 'a' the product operator became

$$-2\hat{S}_y\hat{I}_z$$

After applying the pulsed field gradient  $G_1$  with a duration  $\tau$  along the  $z$ -axis, the operator is converted to

$$[\hat{S}_y \cos\{-\gamma G_1(z)\tau\} - \hat{S}_x \sin\{-\gamma G_1(z)\tau\}]2\hat{I}_z$$

The  $G_2$  is a homo-spoil gradient pulse, thus, at a point 'c' the remained product operator is

$$2\hat{I}_z\hat{S}_y \cos\{-\gamma G_1(z)\tau\}$$

After  $t_1$ -evolution period, at a point 'd', the operator has a form of

$$2\hat{I}_z\hat{S}_y \cos\{-\gamma G_1(z)\tau\} \cos(\Omega t_1)$$

Since the ratio of  $G_1 : G_3 = 4 : 1$  and the observable form of operator is  $\hat{I}_-$ , the +1 coherence order of  $S$ -spin can survive only and it is given by

$$\frac{1}{2i} \hat{I}_z\hat{S}_+ \exp(-i\Omega t_1)$$

Before the acquisition, at a point 'e', final observable operator has a form of

$$\frac{1}{4i} \hat{I}_- \exp(-i\Omega t_1)$$

Thereby, one can acquire the  $N$ -type spectrum without any constant delays during the  $t_1$ -evolution delay

#### **4.5.2 Fast broadband adiabatic inversion pulse**

Previous density operator analysis give a conclusion as follows; any constant, not a variable  $t_1$ , delays during the  $t_1$ -evolution period gives rise to generate dispersive anti-phase component signals (DAPs) in the  $F_1$  domain on the two-dimensional HSQC spectrum with  $^{13}\text{C}$  labeled samples. In general, the conventional composite adiabatic refocusing pulse employed in the analyzed sequence has a long duration (2 ms; a four-fold of adiabatic inversion pulse) than the adiabatic inversion pulse, thus it is enough to induce significant DAPs in the resulted spectrum. Moreover, even a pair of adiabatic inversion pulse requires a thousand microseconds. It is still enough to generate undesired DAPs in resulted HSQC spectrum with  $^{13}\text{C}$ -isotope labeled sample. Since the simple rectangular inversion or composite inversion pulses only require few microseconds duration, for the  $J_{\text{CC}}$  coupling interaction which just have tens of hertz values, the generation of DAPs could be neglected. But, their short inversion coverage, even using the well-designed composite inversion pulse, led an introducing a fast broadband adiabatic inversion pulse for obtaining a pure phase HSQC signals with  $^{13}\text{C}$ -isotope labeled samples. T-L. Hwang *et al.*<sup>98</sup> reported several fast adiabatic pulses including a tangential frequency sweeps which can accomplish a broadband inversion amount to tens of kilohertz bandwidth using a practical  $B_1$  strength. In order to evaluate inversion efficiency of each adiabatic inversion pulses with limited pulse duration and its  $B_1$  strength, simulated inversion profile was calculated. A simulation was carried out using a shapetool<sup>TM</sup> in TopSpin 3.6.1 software.

#### **4.5.3 A phase shift problem of the adiabatic inversion**

For spins with a wide spectral range, in particular with the high-field NMR spectrometer, an effective bandwidth acquired from the simple rectangular hard pulse is sometimes inadequate. Thus, adiabatic pulses have been employed in many modern



NMR pulse sequence for the inversion/refocusing of spins have wide chemical shift range such as  $^{13}\text{C}$ . However, as stated above, the adiabatic full/half passage (AFP/AHP) gives undesired phase shift in case of the inversion of transverse magnetizations<sup>26,27</sup>. During the adiabatic passage, a magnitude of the effective magnetic field  $\mathbf{B}_e(t)$  in the frequency frame is<sup>25</sup>

$$B_e(t) = |\mathbf{B}_e(t)| = \sqrt{B_1^2(t) + (\Delta\omega(t)/\gamma)^2}$$

One can decompose the magnetization into two parts, which are collinear with or perpendicular to  $\mathbf{B}_e(t)$  at the onset of the adiabatic pulse. Employing a second rotating frame which change its orientation with  $\mathbf{B}_e(t)$  at the angular velocity of  $d\alpha(t)/dt$ , relative to the frequency frame.  $\alpha(t)$  is defined as

$$\alpha(t) = \arctan\left(\frac{\Delta\omega(t)}{\gamma B_1(t)}\right)$$

In the second rotating frame, the magnitude of the effective magnetic field  $B'_e(t)$  is

$$B'_e(t) = |\mathbf{B}'_e(t)| = \sqrt{B_e^2(t) + \{(d\alpha(t)/dt)/\gamma\}^2}$$

The adiabatic condition is satisfied when  $\mathbf{B}'_e(t) \approx \mathbf{B}_e(t)$ , which means  $|\mathbf{B}_e(t)| \gg |(d\alpha(t)/dt)/\gamma|$ .

A magnetization which is collinear with  $\mathbf{B}_e(t)$  at  $t = 0$  will follow  $\mathbf{B}_e(t)$  during the adiabatic passage. On contrary a magnetization which is perpendicular to  $\mathbf{B}_e(t)$  at  $t = 0$  will rotate in the second rotating frame, through an angle  $\beta(t)$  as follows

$$\begin{aligned}\beta(t) &= \gamma \int_0^t \mathbf{B}_e(t') dt' \\ &= \gamma \int_0^t \sqrt{\{B_1^2(t') + \Delta\omega(t')/\gamma\}^2} dt'\end{aligned}$$

Therefore, adiabatic full/half passage (AFP/AHP) cannot be used for refocusing transvers magnetization. The transverse magnetization  $M_{xy}$  will be rotate by  $\mathbf{B}_e(t)$ .

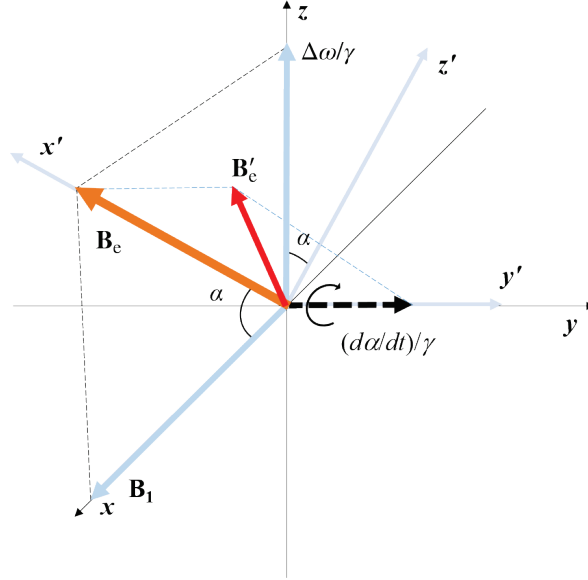


**Figure 4.6** The relation between magnetic field vectors in rotating frames used to describe adiabatic pulses

The first rotating frame of reference,  $xyz$ , precesses at same frequency of the radio frequency pulse which make the  $B_1$  orientation, arbitrarily chosen along  $x$ , static. The second rotating frame  $x'y'z'$  rotates about  $y'$  with angular velocity  $(d\alpha/dt)$  of the  $B_e$  rotation in the first rotating frame. In the second rotating frame, the  $B_e$  orientation is static, leading to an additional vector  $(d\alpha/dt)/\gamma$  along  $y'$  as  $B_e$  is rotating. (Adapted from DeGraaf *et al.*<sup>25</sup> )

#### 4.5.4 Acquiring a pure phase refocusing

Consequently, by an adiabatic inversion pulse, the uniform refocusing of transverse magnetizations cannot be accomplished. There are several solutions to address this type of problems, such as adiabatic composite refocusing pulse<sup>26</sup> and placing a second identical inversion pulse which compensate the phase shift during the first adiabatic passage<sup>27</sup>. Since the adiabatic composite refocusing pulse has a four-fold

longer duration than the single adiabatic inversion pulse, it requires two-fold of duration than a pair of adiabatic inversion pulses. As stated, in addition, a scaling the  $J_{CC}$ -coupling interaction during the  $t_1$ -evolution period requires at least two  $^{13}\text{C}$  refocusing pulses. Thus, choosing a pair of adiabatic inversion pulse can greatly reduce total pulse duration (8-fold) than employing the adiabatic composite pulses. Any constant delays in the  $t_1$ -evolution period give rise to DAPs according to their durations. Therefore, a pair of adiabatic inversion pulse was considered in order to scaling of  $J_{CC}$ -interaction in the  $F_1$  domain of HSQC spectrum. There are some useful explanations<sup>99,100</sup> for a pure-phase refocusing using the inversion pulse pair. But, most general explanation about the pure phase arbitrary rotation including an adiabatic rotation can be induced from a seminal paper written by T.-L. Hwang *et al.*<sup>101</sup>.

Following description is a proof of the pure phase refocusing using an adiabatic inversion pulse pair. Assuming an unitary transformation  $\hat{S}$  which has an arbitrary phase, frequency or amplitude modulation. Since,  $\hat{S}$  can be expressed with three consecutive rotation operators as a form of angular momentum operators

$$\hat{S} = \exp(-i\beta\hat{f}_z) \exp(-i\theta\hat{f}_y) \exp(-i\alpha\hat{f}_x) \exp(i\theta\hat{f}_y) \exp(i\beta\hat{f}_z)$$

Then a density operator form of  $\hat{\rho}'$  after transformation of  $\hat{\rho}$  caused by  $\hat{S}$  is

$$\hat{\rho}' = \hat{S}\hat{\rho}\hat{S}^*$$

Consider,  $\mathbf{m}$  is a magnetization from  $\hat{\rho}$  and  $\mathbf{M}$  is a magnetization from  $\hat{\rho}'$

If  $\mathbf{M} = \mathbf{Tm}$ , then a  $3 \times 3$  transform matrix  $\mathbf{T}$  is

$$\mathbf{T} = \begin{bmatrix} \cos^2 \theta \sin^2(\alpha/2) \cos 2\beta & \cos^2 \theta \sin^2(\alpha/2) \sin 2\beta & 0 \\ \cos^2 \theta \sin^2(\alpha/2) \sin 2\beta & -\cos^2 \theta \sin^2(\alpha/2) \cos 2\beta & 0 \\ 0 & 0 & \cos \alpha \cos^2 \theta + \sin^2 \theta \end{bmatrix}$$

Let us define  $P$ , the probability of spin inversion by  $\mathbf{S}$

$$\begin{aligned} P &= \frac{1}{2} \left( 1 - \frac{M_z}{m_z} \right) \\ &= \frac{1}{2} (1 - \cos \alpha \cos^2 \theta - \sin^2 \theta) \\ &= \cos^2 \theta \sin^2(\alpha/2) \end{aligned}$$

Then, the transform matrix  $\mathbf{T}$  is

$$\mathbf{T} = \begin{bmatrix} P \cos 2\beta & P \sin 2\beta & 0 \\ P \sin 2\beta & -P \cos 2\beta & 0 \\ 0 & 0 & 1 - 2P \end{bmatrix}$$

After applying the transformation  $\mathbf{T}$ , longitudinal magnetization and transverse magnetization are not mixed each other. Each transverse magnetization  $M_x$  and  $M_y$ , however, get mixed to  $P(m_x \cos 2\beta + m_y \sin 2\beta)$  and  $P(m_x \sin 2\beta - m_y \cos 2\beta)$  respectively. Because, the angle  $\beta$  is an inclination of  $B_{\text{eff}}$  due to resonance off-set,  $\Delta\omega/\gamma$ , one can explain a phase shift effect of transverse magnetizations resulted from an adiabatic inversion pulse using this transform matrix expression.

If one applies the transform  $\mathbf{T}$  to the  $\mathbf{M}$  again,  $\mathbf{T}^2$  has a form of

$$\mathbf{T}^2 = \begin{bmatrix} P^2 & 0 & 0 \\ 0 & P^2 & 0 \\ 0 & 0 & (1 - 2P)^2 \end{bmatrix}$$

Resulted transform matrix  $\mathbf{T}^2$  shows that after applying the second identical transformation, each of transverse magnetization returns to their original states; a pure phase inversion/refocusing. The coefficient  $P^2$  means the intensity of magnetization is attenuated according to the inversion efficiency. Consequently, by placing a pair of adiabatic inversion pulse, a spin-echo pulse sequence without any phase shift can be accomplished.

#### 4.5.5 Evaluation of refocusing efficiency

In order to evaluate a pure phase refocusing of the transverse magnetization by the adiabatic inversion pulse pair,  $^{13}\text{C}$  spectra by even-numbered pulse (zero-and double-adiabatic pulse) and odd-numbered pulse (single adiabatic pulse) were compared respectively. As shown in Figure 3.6, in the even-numbered adiabatic pulse spectra, there is no chemical shift dependent phase error due to phase shift during adiabatic passage. On the contrary, in case of the single adiabatic inversion pulse, it exhibits the chemical shift dependent phase error on account of undesired phase evolution during adiabatic passage.

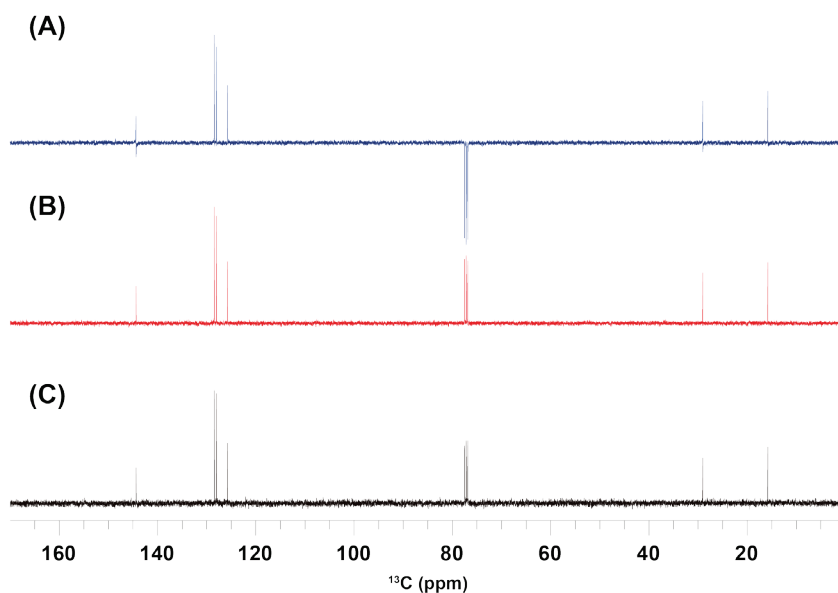


**Figure 4.7 Comparison of  $^{13}\text{C}$  spectra according to the number of adiabatic inversion pulses**

(A) Single-adiabatic inversion pulse (B) Double-adiabatic inversion pulses. (C) Without adiabatic inversion pulses.; To acquire  $^{13}\text{C}$  spectra 10% ethylbenzene in chloroform-d was used. Pulse shape: Tanh/Tan. Pulse duration: 192 microseconds.

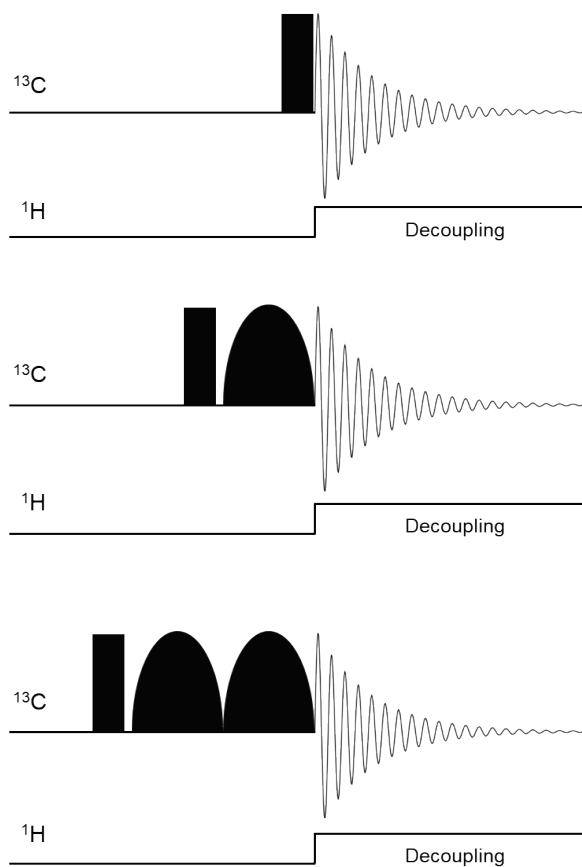


**Figure 4.8** Pulse sequences for comparison of phase shift effects

Pulse sequences for comparison of phase shift effects between zero-, single- and double- adiabatic inversion pulses on transverse magnetization. (Upper) Without adiabatic inversion pulse (Middle) Single-adiabatic inversion pulse (Lower) Double-adiabatic inversion pulse.

## 4.6 Implementation of the *J*-scaling pulse sequence

As stated, the coupling constant and the multiplet structure by *J*-coupling interaction can give structural information such as the number of nearby spins can interact or relative conformation between spins. However, for the indirect domain the observation of their fine structure and exact coupling constant values have been limited due to poor spectral resolution thereof. On the other hands, unlike direct acquisition period in  $t_2$  where the time domain data is actually collected, the indirect detection scheme during the  $t_1$ -evolution period do not requires actual detection of signals by receiver of the spectrometer<sup>13</sup>. Thus, one can manipulate acquisition of the indirect detection scheme without the constraints of data acquisition scheme. Thereby, several manipulation methods, including *J*-scaling<sup>12,13,14</sup> in the indirect domain of two-dimensional NMR have been developed. In the following, first of all, detailed principles based on product operator formalism for *J*-scaling techniques will be addressed and then the implementation of *J*-scaling sequence into actual HSQC pulse sequence will be described.

### 4.6.1 Product operator analysis of the *J*-scaling sequence

Let us consider a pulse sequence consist of two inversion pulse  $\pi(\hat{I}_x + \hat{S}_x)$  and  $\pi\hat{S}_x$ . In this case, consider a weakly coupled two spin system with a Hamiltonian in the rotating frame of reference

$$\hat{H}_0 = \hat{H}_1 + \hat{H}_2; \quad \hat{H}_1 = \Omega_I \hat{I}_z + \Omega_S \hat{S}_z \quad \text{and} \quad \hat{H}_2 = 2\pi J_{IS} \hat{I}_z \hat{S}_z$$

Assuming a density operator,  $\hat{I}_x$ , at  $t = 0$ , the evolution of density operator through the pulse sequence above is described by

$$\begin{aligned} & \hat{I}_x \cos(\Omega_I \tau) \cos(\pi N J_{IS} \tau) + \hat{I}_y \sin(\Omega_I \tau) \cos(\pi N J_{IS} \tau) \\ & - 2\hat{I}_y \hat{S}_z \cos(\Omega_I \tau) \sin(\pi N J_{IS} \tau) + 2\hat{I}_x \hat{S}_z \sin(\Omega_I \tau) \sin(\pi N J_{IS} \tau) \end{aligned}$$

Therefore, one can obtain an N-fold scaled  $J$ -coupling evolution while the scaling of chemical shift evolution being unchanged. If the delay  $\tau$  being changed to a variable delay  $t_1$ ,

$$\begin{aligned} & \hat{I}_x \cos(\Omega_I t_1) \cos(\pi N J_{IS} t_1) + \hat{I}_y \sin(\Omega_I t_1) \cos(\pi N J_{IS} t_1) \\ & - 2\hat{I}_y \hat{S}_z \cos(\Omega_I t_1) \sin(\pi N J_{IS} t_1) + 2\hat{I}_x \hat{S}_z \sin(\Omega_I t_1) \sin(\pi N J_{IS} t_1) \end{aligned}$$

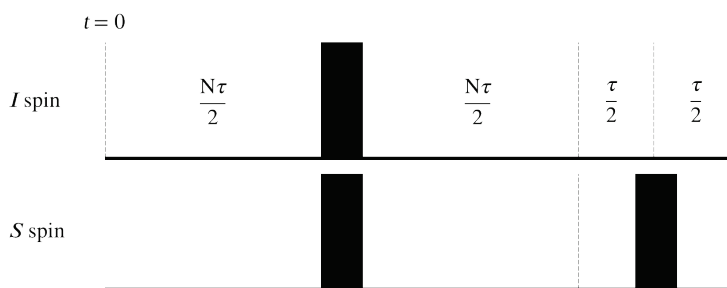


**Figure 4.9** Schematic sequence of the  $J$ -scaling module

Schematic sequence of the  $J$ -scaling module for two spin I and S. Black-bar indicates the inversion pulse  $\pi\hat{I}_x$  and  $\pi\hat{S}_x$ .

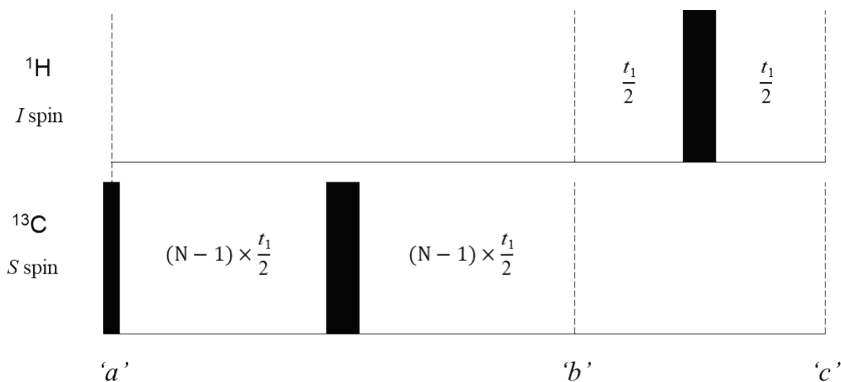


**Figure 4.10** Exemplified  $J$ -scaling module for two-dimensional HSQC

Narrow bar indicates  $\pi/2\hat{I}_x$  excitation pulse and wide bar indicates  $\pi\hat{I}_x/\pi\hat{S}_x$  inversion pulse.



With the stated result, a similar procedure can be applied to HSQC pulse sequence. Suppose that a weakly coupled two spin system with a Hamiltonian in the rotating frame of reference

$$\hat{H}_0 = \hat{H}_1 + \hat{H}_2; \quad \hat{H}_1 = \Omega_1 \hat{I}_z + \Omega_{1,s} \hat{S}_{1,z} + \Omega_{2,s} \hat{S}_{2,z} \quad \text{and} \quad \hat{H}_2 = 2\pi J_{12} \hat{S}_{1,z} \hat{S}_{2,z}$$

where the  $I$ -spin is designated for the  $^1\text{H}$  spin and the  $S$ -pin is designated for the  $^{13}\text{C}$  spin

Assume that at a point ‘a’, the density operator has a form of

$$2\hat{S}_{1,y}\hat{I}_z$$

After a free precession with an inversion pulse the density operator, at a point ‘b’

$$-2\hat{S}_{1,y}\hat{I}_z \cos\{(N-1)\pi J_{12}\} - \hat{S}_{1,x} \sin\{(N-1)\pi J_{12}t_1\}$$

A following pulse sequence gives

$$\begin{aligned} & \cos\{(N-1)\pi J_{12}t_1\} \cos(\Omega_1 t_1) \{2\hat{S}_{1,y}\hat{I}_z \cos(\pi J_{12}t_1) - \hat{S}_{1,x} \sin(\pi J_{12}t_1)\} \\ & - \cos\{(N-1)\pi J_{12}t_1\} \sin(\Omega_1 t_1) \{2\hat{S}_{1,x}\hat{I}_z \cos(\pi J_{12}t_1) + \hat{S}_{1,y} \sin(\pi J_{12}t_1)\} \\ & - \sin\{(N-1)\pi J_{12}t_1\} \cos(\Omega_1 t_1) \{\hat{S}_{1,x} \cos(\pi J_{12}t_1) + 2\hat{S}_{1,y}\hat{I}_z \sin(\pi J_{12}t_1)\} \\ & - \sin\{(N-1)\pi J_{12}t_1\} \sin(\Omega_1 t_1) \{\hat{S}_{1,y} \cos(\pi J_{12}t_1) - 2\hat{S}_{1,x}\hat{I}_z \sin(\pi J_{12}t_1)\} \end{aligned}$$

Using the trigonometric identity, it is simplified to

$$\begin{aligned} & 2\hat{S}_y\hat{I}_z \cos(\Omega_1 t_1) \cos(N\pi J_{12}t_1) - \hat{S}_x \cos(\Omega_1 t_1) \sin(\pi J_{12}t_1) - 2\hat{S}_x\hat{I}_z \cos(\Omega_1 t_1) \cos(\pi J_{12}t_1) \\ & - \hat{S}_y \cos(\Omega_1 t_1) \sin(\pi J_{12}t_1) \end{aligned}$$

After an applying instantaneous  $\pi/2(\hat{I}_x + \hat{S}_x)$  pulse at a point ‘c’,

$$\begin{aligned} & \underbrace{-2\hat{S}_{1,z}\hat{I}_y \cos(\Omega_1 t_1) \cos(N\pi J_{12}t_1) - \hat{S}_{1,x} \cos(\Omega_1 t_1) \sin(\pi J_{12}t_1)}_{\text{Single quantum anti-phase y-magnetization on } I\text{-spin}} \underbrace{-\hat{S}_{1,x} \cos(\Omega_1 t_1) \sin(\pi J_{12}t_1)}_{\text{Single quantum in-phase x-magnetization on } S\text{-spin}} \\ & \underbrace{+2\hat{S}_{1,x}\hat{I}_y \cos(\Omega_1 t_1) \cos(\pi J_{12}t_1) - \hat{S}_{1,z} \cos(\Omega_1 t_1) \sin(\pi J_{12}t_1)}_{\text{Multiple Quantum coherence}} \underbrace{-\hat{S}_{1,z} \cos(\Omega_1 t_1) \sin(\pi J_{12}t_1)}_{\text{z-magnetization on } S\text{-spin}} \end{aligned}$$

Assuming the only retained operator is the single quantum *I*-spin (<sup>1</sup>H) operator, one can get the *N*-fold scaled <sup>13</sup>C-<sup>13</sup>C scalar coupling interaction along the variable  $t_1$  while its (*S*-spin; <sup>13</sup>C) chemical shift evolution is retained.

#### **4.6.2 Effect of the inversion efficiency for the *J*-scaling**

As aforementioned earlier, the adiabatic inversion pulse pair can refocusing the transverse magnetization without any undesirable phase shift. Note that the inversion efficiency affects the intensity of the transverse magnetization. Moreover, in the case of active spin, if the bandwidth of adiabatic inversion pulse is insufficient and these pulse pair conditions are not achieved, it is accompanied by a change in phase of magnetization, along with a reduction in transverse magnetization. Fortunately, most of carbon spins which are detectable in HSQC has rather narrow chemical shift range so that it shows nearly full-inversion efficiency even with the fast adiabatic inversion pulse. Meanwhile, in the case of quaternary carbon with fairly large chemical shift values, only a part of it can be inverted by fast adiabatic inversion pulses with narrow bandwidth, leading to a refocusing of <sup>13</sup>C-<sup>13</sup>C interactions that can cancel the effect of the *J*-scaling module.

Assuming an adiabatic pulse with an inversion efficiency,  $f_k$ , at a specific offset frequency  $\Omega_k$ , the generated *J*-scaled HSQC signal for AMX spin system can be expressed as follows

$$\begin{aligned}
 S(t_1, \omega_2) = & f_2 \cdot f_3 \cdot \prod_{k=2}^3 \left[ \{ \cos(\pi N J_{1k} t_1) \cos(\pi J_{1k} \Delta_t) - \sin(\pi N J_{1k} t_1) \sin(\pi J_{1k} \Delta_t) \} \right] \\
 & + (1 - f_2) f_3 \cdot \{ \cos(\pi J_{12} t_1) \cos(\pi J_{12} \Delta_t) \\
 & - \sin(\pi J_{12} t_1) \sin(\pi J_{12} \Delta_t) \} \cdot \{ \cos(\pi N J_{13} t_1) \cos(\pi J_{13} \Delta_t) \\
 & - \sin(\pi N J_{13} t_1) \sin(\pi J_{13} \Delta_t) \} \\
 & + f_2 (1 - f_3) \cdot \{ \cos(\pi N J_{12} t_1) \cos(\pi J_{12} \Delta_t) \\
 & - \sin(\pi N J_{12} t_1) \sin(\pi J_{12} \Delta_t) \} \cdot \{ \cos(\pi J_{13} t_1) \cos(\pi J_{13} \Delta_t) \\
 & - \sin(\pi J_{13} t_1) \sin(\pi J_{13} \Delta_t) \} \\
 & + (1 - f_2)(1 - f_3) \cdot \prod_{k=2}^3 \left[ \{ \cos(\pi J_{1k} t_1) \cos(\pi J_{1k} \Delta_t) \right. \\
 & \left. - \sin(\pi J_{1k} t_1) \sin(\pi J_{1k} \Delta_t) \} \right]
 \end{aligned}$$

Note that the effect on the *J*-scaling due to the inversion efficiency of second adiabatic inversion pulse was neglected.

Therefore, the final form of the *J*-scaled HSQC signal consists of N-fold (gray-box) and unscaled  $J_{CC}$ -coupling terms depending on the inversion efficiency by the adiabatic pulse of each of passive spins.

## 4.7 Experimental section

### 4.7.1 NMR measurements

All NMR spectra were measured at 298 K with 850 or 800 MHz Bruker Avance III HD spectrometers equipped with 5 mm CPTCI CryoProbes (Bruker BioSpin, Germany). For the U-<sup>13</sup>C acetate and U-<sup>13</sup>C lactate sample, each 1 mM of sample (Sigma-Aldrich, MO, USA) was dissolved in 600  $\mu$ L of deuterium oxide respectively. For *J*-scaled HSQC NMR experiments, the pulse sequence in Figure 3.12 was used. For apodization, cosine-squared function ( $F_1$ ) and cosine function ( $F_2$ ) were employed and zero-filling was applied to both dimensions. All spectra were processed in phased mode along the both  $F_1$  and  $F_2$  domain. The actual time-domain points of pulse sequence were 2048 $\times$ 300 ( $t_2\times t_1$ ) complex points with the final 4096 $\times$ 4096 ( $t_2\times t_1$ ) complex points after zero-filling. The spectral width was 12821 $\times$ 8049 Hz ( $F_2\times F_1$ ) and the frequency offsets were 3761 Hz and 5433 Hz for <sup>1</sup>H and <sup>13</sup>C nuclei respectively. For HSQC (<sup>1</sup> $J_{CH}$ = 145 Hz; delay  $\Delta$ : 3.45 ms), the number of scans was 2 and the total experiment time was about 12 min. For the NUS acquisition, the NUS time-domain points were 2048 $\times$ 3000 complex points with 10% NUS sampling density corresponding to 2048 $\times$ 300 ( $t_2\times t_1$ ) of actual time-domain points complex points and it gives final 4096 $\times$ 4096 ( $t_2\times t_1$ ) complex points after NUS reconstruction and zero-filling

### 4.7.2 Adiabatic pulses

Pulse	Duration ( $\mu$ s)	$\gamma B_{1,max}$ (Hz)	Sweep width (kHz)
Tanh/Tan, $R = 153$	192	13778	800
Tanh/Tan, $R = 390$	300	14051	1300
<sup>a</sup> Crp80comp.4	2000	11283	80
<sup>b</sup> Crp80,0.5,20.1	500	11283	80

<sup>a,b</sup> From Topspin 3.6 preset adiabatic pulses

### 4.7.3 Simulation of the HSQC signal

Simulated  $J$ -HSQC signal was plotted by home-built python 3.6 script. For simulation the equation derived from 3.6.2 was used. In simulated spectrum,  $^{13}\text{C}$ - $^{13}\text{C}$  coupling constants were set to 57 Hz and 36.5 Hz respectively. Delay  $\Delta_t$  was set to 1.6 ms and  $R_2$  relaxation constant was set to 0.3. For the Fourier transformation,  $f_{max}$  was set to 4000 Hz and time-domain points were 150 complex points with the final 4096 complex points after zero-filling. For the apodization cosine-squared function was employed. The inversion efficiency of assumed as 0.94.

## 4.8 Results and discussion

### 4.8.1 Validation of the *J*-scaling sequence

The advantage of *J*-scaling is that the degree of the scaling can be adjusted simply by adjusting the scaling factor, *N*, without increasing the additional measurement time. For its validation, the actual splitting pattern changes according to the scaling factor adjustment using U-<sup>13</sup>C acetate samples was monitored. As shown in Figure 3.10, the coupling constant by <sup>13</sup>C-<sup>13</sup>C coupling interaction between carbonyl carbon and alpha carbon of U-<sup>13</sup>C acetate is increased in proportion to the size of the scaling factor *N*.

### 4.8.2 Comparison of signal distortion effects by adiabatic pulses

Since the finite delay time within the  $t_1$ -evolution period causes the signal distortion of the HSQC signal of the <sup>13</sup>C-isotope labeled compound. To address this, the coherence selection module was moved outside the  $t_1$ -evolution period and a short adiabatic inversion pulse pair was introduced. On the other hand, in the case of fast adiabatic inversion pulse, due to restrictions such as peak power conversion, proper compromise between pulse length and bandwidth is needed. For this purpose, the degree of HSQC signal distortion by their pulse duration was compared using several adiabatic pulses with similar peak power conversion. As shown in Figure 3.12, the intensity of the signal distortion changed with the change in adiabatic pulse length. In the case of composite adiabatic pulse with a pulse length of 2 ms (Figure 3.12A), the magnitude of the signal indicating the signal distortion in the gray box, along with the broadening of the individual signal, was very large, while this signal distortion tended to decrease as the length of the adiabatic pulse became shorter. Meanwhile, the change in the effective bandwidth of each inversion pulse according to the pulse length due to the restriction conditions such as peak power was also evaluated.

As mentioned in 3.6.2, the selective refocusing of  $^{13}\text{C}$ - $^{13}\text{C}$  coupling with a large offset value due to restrictions on the coverage of adiabatic inversion was shown together with the splitting pattern, which does not show the effect of  $J$ -scaling.

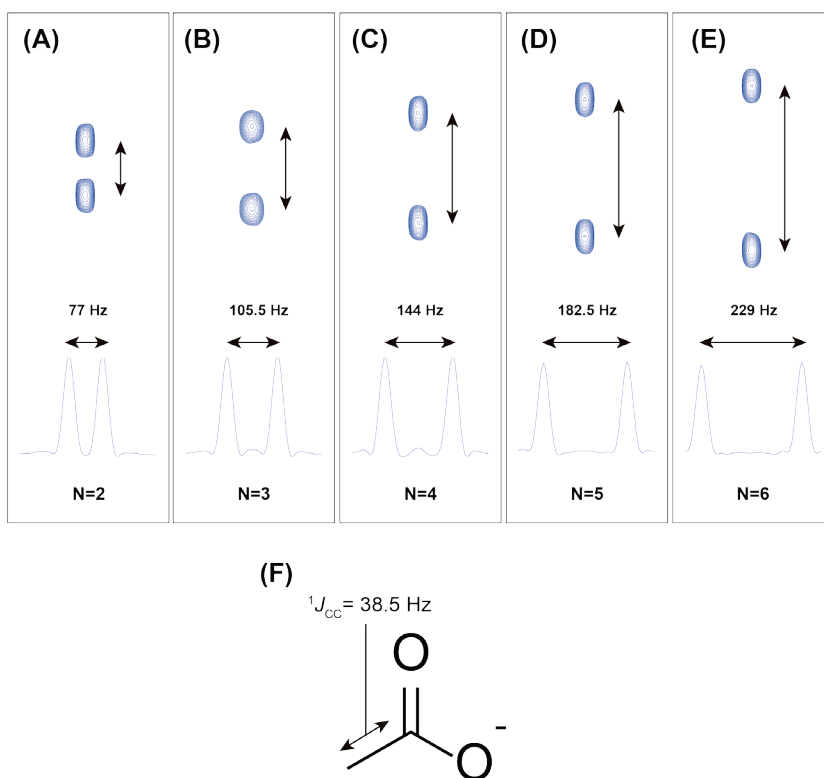


**Figure 4.11 Comparison of HSQC signals according to  $J$ -scaling factor**

Comparison of scale-up of the  $J$ -coupling constant with difference scaling factor ' $N$ '. (A-E) The doublet signals of U- $^{13}\text{C}$  acetate HSQC spectrum produced according to each scaling factor ' $N$ '. The bottom 1D signals are  $F_1$  projection spectrum. (F) Structure of acetate and its  $^1J_{\text{CC}}$  coupling constants.

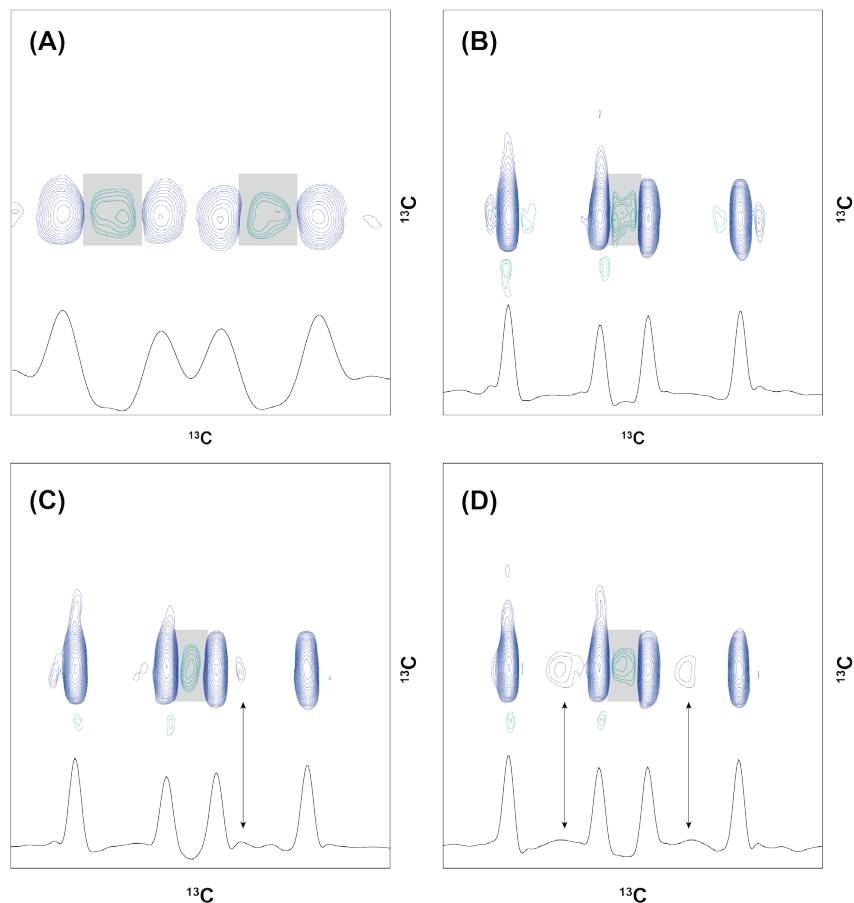


**Figure 4.12 Comparison of HSQC signals according to pulse type and its duration**

Comparison of HSQC signal alpha carbon of U- $^{13}\text{C}$  lactate with different adiabatic pulses, duration; The scaling factor 'N' was set to 6. (A) Composite chirped adiabatic refocusing pulse; Crp80comp.4, 2000  $\mu\text{s}$  (B) Chirped adiabatic inversion pulse; Crp80,0.5,20.1, 500  $\mu\text{s}$  (C) Tangent hyperbolic tangent (Tanh/Tan) adiabatic inversion pulse, 300  $\mu\text{s}$  (D) Tanh/Tan adiabatic inversion pulse, 192  $\mu\text{s}$ .; Gray-boxes indicate signal distortion due to the generation of dispersive anti-phase term according to the duration of adiabatic pulses. Double-headed arrows indicate unscaled  $^{13}\text{C}$ - $^{13}\text{C}$  coupling due to insufficient inversion efficiency of adiabatic pulses.



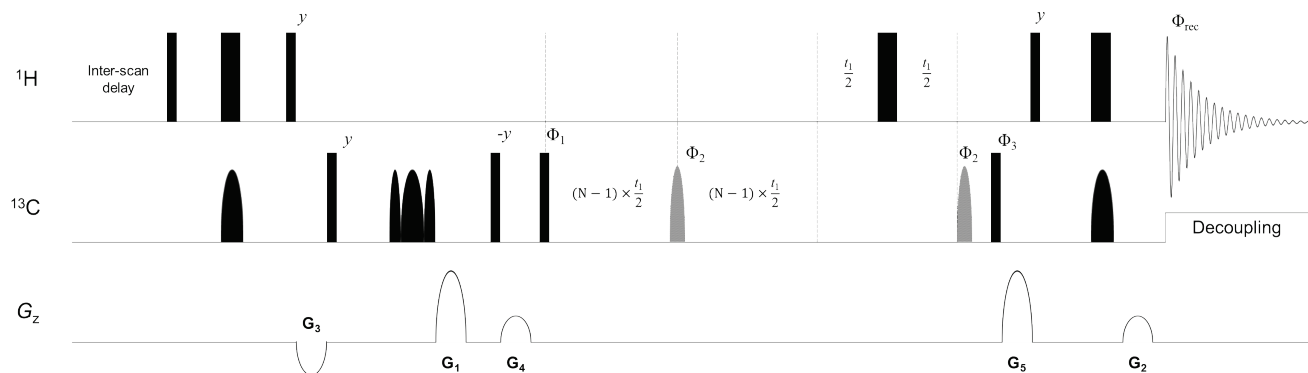


**Figure 4.13** Pulse sequence of <sup>13</sup>C-<sup>13</sup>C distortion-free *F*<sub>1</sub>-pure in-phase *J*-scaled HSQC

Proposed pulse sequence of <sup>13</sup>C-<sup>13</sup>C distortion-free *F*<sub>1</sub>-pure in-phase *J*-scaled HSQC. Phase of  $\Phi_1$  and was shifted by 90° at every increment. The phase cycling is as follows.  $\Phi_1 = x, -x$ ;  $\Phi_2 = -y, -y, y, y$ ;  $\Phi_3 = -x, -x, x, x$   $\Phi_{\text{rec}} = x, -x, -x, x$ . Gradient ratios: *G*<sub>1</sub> : *G*<sub>2</sub> = 4 : 1 and *G*<sub>3</sub>, *G*<sub>4</sub> and *G*<sub>5</sub> are homospoil gradient pulses.

### **4.8.3 Acquiring of the <sup>13</sup>C-<sup>13</sup>C distortion-free HSQC signal**

Finally, the HSQC signals acquired from the proposed pulse sequence (Figure 3.12) were compared with those produced by the conventional HSQC pulse sequence. To this end, using the U-<sup>13</sup>C-lactate, conventional HSQC signals with the same  $t_1$ -time-domain point (TD: 300) and 3000  $t_1$ -time-domain points were obtained and compared with the proposed  $J$ -scaled HSQC signals (scaling factor = 6). In the case of conventional HSQC, the intact doublet of doublet signal at *alpha* carbon of U-<sup>13</sup>C lactate did not appear due to poor resolution of the indirect domain (Figure 3.13A) and signal distortion (Figures 3.13A and B). On the other hand, in the case of  $J$ -scaled HSQC signal (Figure 3.13C), despite the same sampling point value (TD: 300) as in Figure 3.13A, the correct doublet of doublet signal could be confirmed due to the six-fold increased <sup>13</sup>C-<sup>13</sup>C interaction effect, and signal distortion caused by anti-phase also rarely appeared. Of note, the simulated  $J$ -scaled HSQC signal according to the results derived from 3.6.2 also showed almost the same form as the actual signal (Figure 3.13D and E).

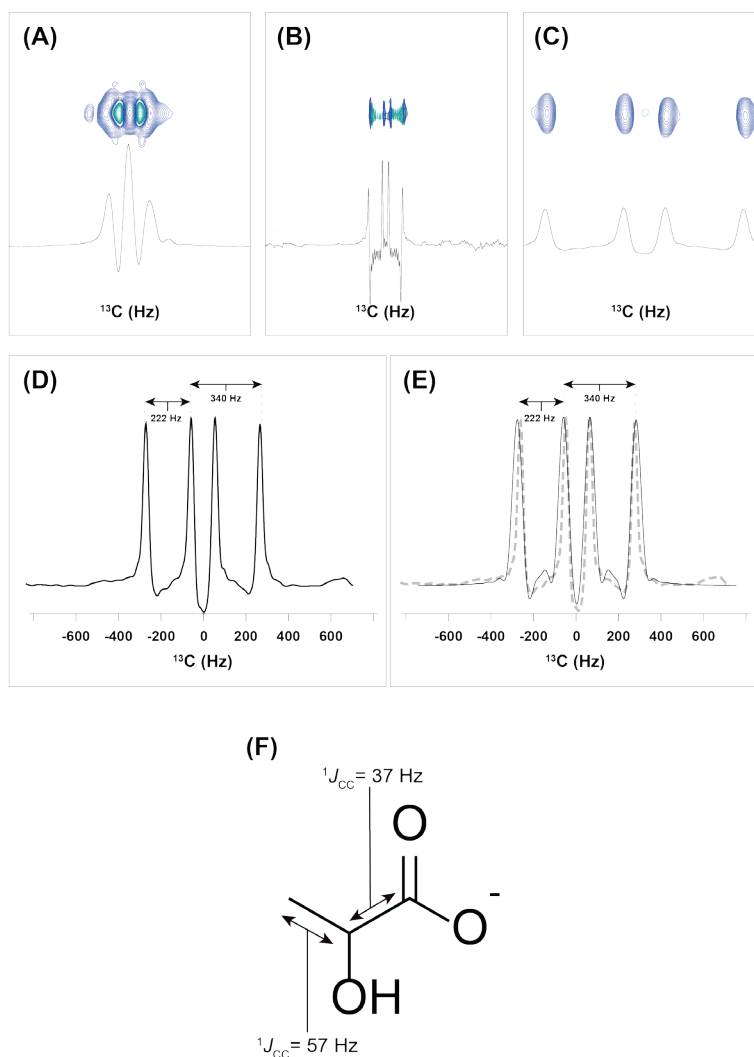


**Figure 4.14 Comparison of HSQC signals using HSQC, NUS-HSQC and J-scaled HSQC**

Comparison of HSQC signal of alpha carbon of U-<sup>13</sup>C lactate. (A) Conventional HSQC signal (TD:300; uniform sampling). (B) Conventional HSQC signal (TD:3000; NUS 10% sampling density was used). (C) J-scaled HSQC signal (TD: 300, scaling factor: 6) (D) Enlarged of (C) (E) Simulated signal (solid line); Dotted line indicates signal of (D). (F) Structure of U-<sup>13</sup>C lactate and its  $^1J_{CC}$ -coupling constants.

## 4.9 Conclusions

In this study, a novel HSQC measurement sequence to effectively analyze the intact peak splitting pattern and to facilitate extract the exact coupling constant by  $^{13}\text{C}$ - $^{13}\text{C}$  interaction of the  $^1\text{H}$ - $^{13}\text{C}$  correlation spectrum (HSQC) signal of a  $^{13}\text{C}$  isotope labeled compound devised. Through this, the peak splitting pattern due to the  $^{13}\text{C}$ - $^{13}\text{C}$  interaction was confirmed without an increase in the additional sampling point (increasing of experiment time).

At this point, an unscaled  $^{13}\text{C}$ - $^{13}\text{C}$  coupling signal was observed due to incomplete coverage of the adiabatic inversion pulse used. These problems will then be addressed by the introduction of other types of the broadband inversion pulse (BIP)<sup>102,103,104</sup>, which provides wider bandwidth under constraints such as limited  $B_{1,max}$  values and pulse duration. In addition, the present *J*-scaled HSQC sequence omitted the introduction of the PEP module due to problems in the decrease of HSQC signal intensity and limited inversion coverage of adiabatic pulse. However, this problem can also be solved by the introduction of an infusion pulse with wider coverage and shorter duration.

In conclusion, the *J*-scaled HSQC may be widely applied in metabolite analysis studies in which the concentration of a sample is low or a  $^{13}\text{C}$  isotope-labeled compound is frequently used for analysis of a specific metabolic pathway. In addition, since NMR experiment proposed here does not require additional measurement time, it can be expected to be used for real-time metabolite analysis based on NMR spectroscopy.

## **Chapter 5**

### **5 Conclusion**

As discussed throughout this thesis,  $^{13}\text{C}$ - $^{13}\text{C}$  correlation gives valuable structural information especially organic molecules consisting of carbon nuclei. In this context, developments of two novel NMR methods were discussed as follows

1. Spectral deconvolution methods for NMR based mixture analysis.
2. Novel  $^{13}\text{C}$ - $^{13}\text{C}$  distortion-free  $J$ -scaled HSQC

In chapter 3, novel NMR acquisition and processing method providing a high-resolution  $^{13}\text{C}$ - $^{13}\text{C}$  correlation spectrum of a compound with many quaternary carbons was presented. It was shown that modified HMBC pulse sequence tailored to the indirect covariance operation in concert with NUS acquisition scheme can give rise to high-quality  $^{13}\text{C}$ - $^{13}\text{C}$  correlation spectrum. Then, a fidelity of resulted  $^{13}\text{C}$ - $^{13}\text{C}$  correlation network was evaluated with rotenone, a natural compound consisting of total 23 carbon nuclei and resulted spectrum shows very reliable correlation  $^{13}\text{C}$ - $^{13}\text{C}$  correlation information. Since, in principle, every  $^{13}\text{C}$  nuclei information in most of single small organic molecule consisting carbon skeleton could be assembled by long-range  $^1\text{H}$ - $^{13}\text{C}$  correlation NMR spectroscopy such as HMBC, it was demonstrated that from proton sensitivity  $^1\text{H}$ - $^{13}\text{C}$  correlation spectrum of certain small organic compounds, one can acquire reliable  $^{13}\text{C}$ - $^{13}\text{C}$  correlation network information.

Additionally, based on the above conclusion, an optimized signal-processing procedure (DECODE) for the extraction of individual carbon NMR spectra from mixture NMR data was developed. For this, several considerations which are tailored to eigendecomposition process including NMR acquisition and indirect covariance operation were discussed and the performance of DECODE then evaluated by 1:1 mixture sample and DECODE provided complete individual  $^{13}\text{C}$  NMR spectra. Since DECODE based on  $^{13}\text{C}$  NMR which has sparse signal distribution comparing to  $^1\text{H}$  NMR, two  $^{13}\text{C}$  signals separated by tens of Hz intervals was distinguished.

In chapter 4, novel HSQC pulse sequence for the analysis of  $^{13}\text{C}$ -isotope labeled compounds which were frequently employed in NMR based cellular metabolic analysis was presented. Firstly, an analytical solution of HSQC signal responsible for a phase-distortion in the indirect domain was deduced using the product operator analysis. It turns out that any constant delays in  $t_1$ -evolution period can generate dispersive anti-phase signals according to the duration of the constant delay. Thus, in order to evaluate the analytical solution, the simulated signal was compared with real HSQC signal. Based on the analytical solution, then, a modified HSQC pulse sequence which can provide distortion-free HSQC signal was presented. In addition, to facilitate  $J$ -coupling splitting analysis within a limited experimental time, consideration for incorporating of  $J$ -scaling pulse sequence into HSQC pulse sequence also discussed. Since the incorporation of  $J$ -scaling module does not affect total experiment time, it effectively and selectively increased the splitting signals due to  $^{13}\text{C}$ - $^{13}\text{C}$  interactions. Overall, suggested novel HSQC pulse sequence successfully provided distortion-free signal containing a fine structure of  $J_{\text{CC}}$ -multiplet within ten-minute.

Since the NMR methods suggested in this thesis do not require any special instruments or computational techniques, it can be easily adopted to previous NMR based analysis and the described approaches should prove useful in various fields of chemistry and cellular metabolomics.

# Appendix A

## A Pulse sequence codes

### A.1 NMR pulse sequence codes for Bruker Topspin 3.6

---

```
;mHMBC sequence for DECODE          "in30=in6"

;J. W. Cha

                                     "d0=3u"

; $CLASS=HighRes                     "d6=1s/(cnst14*2)"

; $DIM=2D                            "d30=d6"

; $TYPE=

; $SUBTYPE=                          "DELTA1=1s/(2 * (cnst6 + 0.146 *
; $COMMENT=                          (cnst7-cnst6)) ) -p16-d16"

                                     "DELTA2=1s/(2 * (cnst7 - 0.146 *
                                     (cnst7-cnst6)) ) -p16-d16"

#include <Avance.incl>               "DELTA3=p16+d16"

#include <Grad.incl>                  "DELTA4=p16*4+d16*4+d13*2+p4"

#include <Delay.incl>                 "DELTA5=DELTA1+DELTA2+p16*2+d16*
                                     2+p3*2-d12"

                                     "DELTA6=d30-d12"

                                     "DELTA7=p2+6u"

                                     "DELTA8=p3*2/3.1416"

                                     "DELTA9=(DELTA7-DELTA8)/2"

                                     "DELTA10=(6u+p2)/2"

"p2=p1*2"

"p4=p3*2"

"d11=30m"

"d12=20u"

"d13=4u"

                                     "cnst30=(1-
                                     sfo2/sfo1)/(1+sfo2/sfo1)"

"in0=infl/2"

define list<gradient> EA1 =
{ 1.000 -cnst30}

define list<gradient> EA2 = { -
cnst30 1.000}

"FACTOR1=( (1s/(cnst14*2)) -
(1s/(cnst15*2)) ) * 10000000 /
td1"

"in6=FACTOR1/10000000"

1 ze
```



```

2 d11 do:f2                                d11 do:f2 mc #0 to 2
3 50u UNBLKGRAD                            F1EA(calgrad(EA1) & cal-
p16:gp4                                    grad(EA2), caldel(d0, +in0) &
d16                                        caldel(d6, -in6) & caldel(d30, -
p1 ph1                                    in30) & calph(ph3, +180) &
p16:gp4                                    calph(ph31, +180))
d16 pl2:f2                                exit
d1
p1 ph1                                    ph1= 0
d6                                        ph2= 0
(p3 ph3):f2 ; for producing MQ            ph3= 0 2
state                                    ph5= 2 2 0 0
DELTA3 pl0:f2                            ph6= 0
DELTA10                                    ph31= 2 0 0 2
(p24:sp7 ph6):f2
DELTA3 pl2:f2
DELTA10
DELTA8
d0
p2 ph2
d0
p16:gp1*EA1
d16 pl0:f2
DELTA8
(p24:sp7 ph6):f2
p16:gp2*EA2
d16 pl2:f2
DELTA10*2
(p3 ph5):f2
DELTA6
d12 pl12:f2 BLKGRAD
go=2 ph31 cpd2:f2

```

## *Pulse sequence codes*

---

```
;d11: delay for disk I/O [30 msec]
;d12: delay for power switching [20 usec]
;d13: short delay [4 usec]
;d16: delay for homospoil/gradient recovery
;d30: decremented delay = d6
;cnst14: = J(XH) long range (min)
;cnst15: = J(XH) long range (max)
;inf1:  $1/SW(X) = 2 * DW(X)$ 
;in0:  $1/(2 * SW(X)) = DW(X)$ 
;nd0: 2
;in6:  $(d6max - d6min)/td1$  [200msec-20msec]
;in30: = in6
;ns:  $2 * n$ 
;ds: 16
;td1: number of experiments
;FnMODE: EA
;cpd2: decoupling according to sequence defined by cpdprg2
;pcpd2: f2 channel - 90 degree pulse for decoupling sequence

;for z-only gradients:
;gpz1:80%
;gpz3:20%
;gpz4:60%

;use gradient files:
```

```
;gpnam1: SMSQ10.100
;gpnam2: SMSQ10.100
;gpnam3: SMSQ10.100
;gpnam4: SMSQ10.100
;gpnam5: SMSQ10.100
;gpnam6: SMSQ10.100
;gpnam7: SMSQ10.100
;gpnam8: SMSQ10.100

;13C-13C distortion-free pure in-phase J-scaled HSQC
;J.W. Cha
;$CLASS=HighRes
;$DIM=2D
;$TYPE=
;$SUBTYPE=
;$COMMENT=

#include <Avance.incl>
#include <Grad.incl>
#include <Delay.incl>

"p2=p1*2"
"p4=p3*2"
"d4=1s/(cnst2*4)"
"d11=30m"

"d0=3u"
```

	(p24:sp10 ph8):f2
"in0=inf1/2"	4u
	p16:gp1
	d16 p12:f2
"DELTA=d0*2+p2"	(p3 ph9):f2
"DELTA1=p16+d16+4u"	4u
"DELTA2=d4-p16-d16-de+p1*2/PI-8u"	p16:gp2
	d16
"DELTA5=p3*2/PI"	(p3 ph10):f2
"DELTA6=d0*2+p2-p3*2/PI"	d0 p10:f2
"DELTA7=d4-larger(p2,p14)/2-4u"	d0
"DELTA8=d4-larger(p2,p14)/2"	d0
"DELTA9=d4-larger(p2,p14)/2-p16-d16-de+p1*2/PI-8u"	d0
	d0
"acqt0=0"	(p17:sp7 ph13):f2
baseopt_echo	d0
	d0
	d0
1 ze	d0
d11 p112:f2	d0
2 d1 do:f2	DELTA5
3 (p1 ph1)	d0
DELTA7 p10:f2	(p2 ph4)
(center (p2 ph1) (p14:sp3 ph6):f2 )	d0
DELTA7 p12:f2	(p17:sp7 ph13):f2
(p1 ph3)	DELTA6 p12:f2
4u UNBLKGRAD	(p3 ph11):f2
p16:gp4	4u
d16	p16:gp5
(p3 ph7):f2	d16
DELTA1 p10:f2	(p1 ph3)
	DELTA8 p10:f2

```

    (center (p2 ph1) (p14:sp3
ph1):f2 )
    4u
    p16:gp3
    d16
    DELTA9 p12:f2
    4u BLKGRAD
    go=2 ph31 cpd2:f2
    d1 do:f2 mc #0 to 2
    F1PH(calph(ph10, +90),
    caldel(d0, +in0))
    exit

ph1=0
ph2=0
ph3=1
ph4=0
ph5=0
ph6=0
ph7=1
ph8=0
ph9=3
ph10=0 2
ph11=2 2 0 0
ph12=0
ph13=3 3 1 1
ph31=0 2 2 0

;pl12: f2 channel - power level
;for CPD/BB decoupling

;p1 : f1 channel - 90 degree
;high power pulse

;p2 : f1 channel - 180 degree
;high power pulse

;p3 : f2 channel - 90 degree
;high power pulse

;p4 : f2 channel - 180 degree
;high power pulse

;p16: homospoil/gradient pulse
;d0 : incremented delay (2D)
[3 usec]

;d1 : relaxation delay; 1-5 * T1

;d4 : 1/(4J)XH

;d11: delay for disk I/O
[30 msec]

;d16: delay for homospoil/gradient
;recovery

;cnst2: = J(XH)

;inf1: 1/SW(X) = 2 * DW(X)

;in0: 1/(2 * SW(X)) = DW(X)

;nd0: 2

;ns: 1 * n

;ds: 16

;td1: number of experiments

;FnMODE: States-TPPI, TPPI,
;States or QSEQ

;cpd2: decoupling according to
;sequence defined by cpdprg2

;pcpd2: f2 channel - 90 degree
;pulse for decoupling sequence

;p11 : f1 channel - power level
;for pulse (default)

;p12 : f2 channel - power level
;for pulse (default)

;CNST60 : center frequency of
;carbon pulse

```

```
;use gradient ratio:  gp 1 : gp
2 : gp 3

;                               80 :
30 : 20.1    for C-13

;                               80 :
30 :  8.1    for N-15


;for z-only gradients:

;gpz1: 80%
;gpz2: 30%

;gpz3: 20.1% for C-13, 8.1% for
N-15

;gpz4:-40%
;gpz5: 30%

;use gradient files:

;gpnam1: SMSQ10.100
;gpnam2: SMSQ10.100
;gpnam3: SMSQ10.100
;gpnam4: SMSQ10.100
;gpnam5: SMSQ10.100
```

---

## Appendix B

### B Python processing scripts

#### B.1 Processing scripts for DECODE procedure

---

```
#Spectral merging
import nmrglue as ng
import numpy as np
import json
import sys
import re

file1 = sys.argv[1]
file2 = sys.argv[2]
file3 = sys.argv[3]
file4 = sys.argv[4]

dic1, data1 =
ng.pipe.read(file1)
dic2, data2 =
ng.pipe.read(file2)
dic3, data3 =
ng.pipe.read(file3)

data11= np.absolute(data1)
data22 = np.absolute(data2)
data3 = np.absolute(data3)

for i in range(0,
len(data1[:,1])):
    for j in range(0,
len(data1[1,:])):
        if data11[i,j] >=
data22[i,j]:
            data1[i,j] = data1[i,j]
        else:
            data1[i,j] = data2[i,j]

    for j in range(0,
len(data3[1,:])):
        if data11[i,j] >=
data3[i,j]:
            data1[i,j] = data1[i,j]
        else:
            data1[i,j] = data3[i,j]

ng.pipe.write(file3, dic1,
data1, overwrite=True)

#Calculation of spectral deriva-
tives
import nmrglue as ng
import numpy as np
```

---

<pre>import json import sys import re import math  file1 = sys.argv[1] file2 = sys.argv[2]  dic, data = ng.pipe.read(file1)  for i in range(0, len(data[:,1])):     data[i,:] = np.gradient(data[i,:])  ng.pipe.write(file2, dic, data, overwrite=True)</pre> <hr/> <pre>#Calculation of magnitude value import nmrglue as ng import numpy as np import json import sys import re import math  file1 = sys.argv[1] file2 = sys.argv[2]  dic, data = ng.pipe.read(file1)</pre>	<pre>print(np.shape(data)) i = 0 while i &lt; len(data[:,1]):     data[i,:] = np.absolute(data[i,:])     i += 1  ng.pipe.write(file2, dic, data, overwrite=True)</pre> <hr/> <pre>#Calculation of the first spectral moment import nmrglue as ng import numpy as np import json import sys import re import math  file1 = sys.argv[1] file2 = sys.argv[2] #file3 = sys.argv[3]  dic, data = ng.pipe.read(file1) data = np.power(data, 2)  def mu(j, k):     s = 0     m = 0     for l in range(-k, k+1):         p = (l+j)*data[:, j+1]         q = data[:, j+1]</pre>
---	--

```
        s += p
        m += q
    r = s/m
    return r
def Range(n):
    c = 0
    while c < n:
        yield c
        c += 1
avg = np.zeros_like(data)
std = np.zeros_like(data)

#for i in range(0,
len(data[:,1])):
for j in Range(len(data[1,:])):
    if j-7 >= 0 and j+7 <
len(data[1,:]):
        avg[:,j] = mu(j, 7)
    else:
        pass

ng.pipe.write(file2, dic, avg,
overwrite=True)
```

---

```
#Calculation of the indirect co-
variance spectrum with the first
spectral moment filter

import nmrglue as ng
import numpy as np
import json
import sys
import re
import math
```

```
from numpy.linalg import
multi_dot

import timeit

start = timeit.default_timer()
file1 = sys.argv[1]
file2 = sys.argv[2]
file3 = sys.argv[3]

dic, data = ng.pipe.read(file1)
dic2, mean = ng.pipe.read(file2)
data2 = np.copy(data)
def Range(n):
    c = 0
    while c < n:
        yield c
        c += 1
def Spec_M(a,b):
    one = (np.ones_like(a))
    delta = 1.4 * one
    c = np.absolute(np.sub-
tract(a,b))
    d = np.recipro-
cal(one+np.exp(-10*(-c+1.25)))
    return d
```

```
def Tri_cov(x,y,z):
    multiply = np.multiply(x,y)
    result = np.dot(multiply, z)
    return result

def Cov(i,j):
    a1 = data[i,:]
    a2 = data2[j,:]
```



```

a = mean[i,:]
b = mean[j,:]
m = Spec_M(a,b)
d = Tri_cov(a1, a2, m)
return i, j, d
import itertools

import multiprocessing as mp

if __name__=='__main__':
    pool = mp.Pool(20)

row_c = len(data[:, 1])
    cov = np.zeros((row_c,
row_c))
    cov = cov.astype(np.float32)
    print(np.shape(cov))
    #result = []
    print('start building a
list')

    list = [(i,j) for i in
Range(len(data[:,1]))
            for j in
Range(len(data[:,1]))]
    print('finishing list
build')

    for i in pool.starmap(Cov,
iterable=list):
        result = i
        #print(result)
        a = result[0]; b = re-
sult[1]; c= result[2]
        cov[a,b] = c
    print(np.max(cov))
    print(np.shape(cov))

    U, s, VT =
np.linalg.svd(cov, full_matri-
ces=True)
    diag = np.diag(s)
    #print(diag)
    #print(np.shape(diag))
    sqrt_diag = np.sqrt(diag)
    part_sqrt = np.dot(U,
sqrt_diag)
    sqrt_cov = np.dot(part_sqrt,
VT)

    sqrt_cov.astype(np.float32)
    par = json.dumps(dic)

    #print(np.shape(sqrt_cov))

    p = re.compile(r'FDF1\w+')
    F1 = p.findall(par)

    F1.sort()

    p = re.compile(r'FDF2\w+')
    F2 = p.findall(par)

    F2.sort()

    for i in range(0, len(F1)):
        F1_key = F1[i]
        F2_key = F2[i]
        dic[F2_key] = dic[F1_key]

    dic["FDSIZE"] =
dic["FDF1FTSIZE"]

```

```
dic["FDSPECNUM"] =
len(cov[1,:])

#print(np.max(cov))

stop = timeit.de-
fault_timer()

print(stop - start)

ng.pipe.write(file3, dic,
sqrt_cov, overwrite=True)

#Signal normalization, peak dig-
itization procedure and eigen-
decomposition

import re
import sys
import math
import numpy as np
from numpy import linalg as la
from scipy import stats
import scipy.signal as signal
import random
import matplotlib.pyplot as plt
import nmrglue as ng
import json

file1 = sys.argv[1]
file3 = sys.argv[3]

dic, data = ng.pipe.read(file1)
dic2, ref = ng.pipe.read(file3)

data[data <= 1] = 1
data = np.log10(data)
data[data < 0] = 0

row_n = len(data[:, 1])
row_r = len(data[1, :])

a = plt.plot(ref)
plt.setp(a, color='r', linewidth
= '0.5')
plt.show()

threshold = float(input("thresh-
old: "))

peaks= signal.find_peaks(ref,
height= threshold)

peaklist = list(peaks[0])

peaklist2=[]
peaklist3=[]
peaklist.sort()
print(peaklist)

for i in peaklist:
    if i-1 >= 0:
        peaklist2.ap-
pend(i-1)

for i in peaklist:
    if i+1 <= row_n-1:
        peaklist3.ap-
pend(i+1)

peaklist = peaklist + peaklist2
+ peaklist3
peaklist.sort()
```

```

max_val = float(np.amax(data))
one = np.ones_like(data)

delta = input("insert delta = ")
delta = float(delta)

data = np.reciprocal(np.exp
(-30*one* (2*data/max_val -
delta*one) ) + one)

for i in peaklist:
    crp = data[i, :]
    cross_peaks= sig-
nal.find_peaks(crp, height=
0.01)
    cross_list =
list(cross_peaks[0])
    for j in range(0,
row_n):
        if j not in
cross_list:
            data[i,
j] = 0
            data[j,
i] = 0
P = []
for i in range(0, row_n):
    if i in peaklist:
        P.append(int(1))
    else:
        P.append(int(0))

D = np.diag(P)
part_D = np.dot(D, data)
data = np.dot(part_D, D)

data = data.astype(np.float32)

w, v = la.eigh(data)
data = np.flip(data, axis=1)

n_eigenmode = sys.argv[2]
template_1 = sys.argv[1]
template_2 = 'test.ft1'

dic_13C, data_ref =
ng.pipe.read(template_1)
dic_1D_1H, data_ref =
ng.pipe.read(template_2)

par = json.dumps(dic_13C)
p = re.compile(r'FDF1\w+')
F1 = p.findall(par)
F1.remove('FDF1LABEL')

par2 = json.dumps(dic_1D_1H)
p = re.compile(r'FDF2\w+')
F2 = p.findall(par2)
F2.remove('FDF2LABEL')

for i in range(0, len(F1)):
    F1_key = F1[i]
    F2_key = F2[i]
    dic_1D_1H[F2_key] =
dic_13C[F1_key]
dic_1D_1H["FDF2LABEL"] = "13C"
dic_1D_1H["FDF2C1"] = 0.0
dic_1D_1H["FDF2QUADFLAG"] = 1.0

```

```
dic_1D_1H["FDSIZE"] =
dic_1D_1H["FDF2FTSIZE"]

FDSIZE = float(row_n)

dic_1D_1H["FDF2LABEL"] = "13C"
dic_1D_1H["FDSIZE"] = FDSIZE
dic_1D_1H["FDF2TDSIZE"] = FDSIZE
dic_1D_1H["FDF2FTSIZE"] = FDSIZE

dic_1D_1H["FDF2OBS"] =
dic_13C["FDF1OBS"]

dic_1D_1H["FDF2SW"] =
dic_13C["FDF1SW"]

dic_1D_1H["FDF2CAR"] =
dic_13C["FDF1CAR"]

dic_1D_1H["FDF2CENTER"] =
dic_13C["FDF1CENTER"]

dic_1D_1H["FDF2ORIG"] =
dic_13C["FDF1ORIG"]

data = np.flip(data, axis=1)

i = 1
k = int(n_eigenmode)
while i <= k:

    ng.pipe.write(f'eigenmode_{i}_{t
hreshold}_{delta}', dic_1D_1H,
v[:, row_n-i], overwrite=True)

    i += 1

ng.pipe.write('DECODE_result',
dic, data, overwrite=True)
```

---

## B.2 Signal simulation scripts for *J*-scaled HSQC

---

```

#Simulation for signal distortion in conventional HSQC using
13C-isotope labeled compound

import numpy as np

import matplotlib.pyplot as plt

f_max = 120
dt = 1/(2*f_max)
TD = 1024
de = 0.0044
de2 = 0.0048

t = np.arange(0, TD*dt, dt)
relax = np.exp(-9.0*t)

J1 = 36.5
J2 = 57

#print(t)

#          fid          =
np.exp(1j*np.pi*3*t)*np.cos(np.p
i*35*t)*np.cos(np.pi*55*t)*relax

fid          =
np.cos(np.pi*J1*t)*np.cos(np.pi*
J1*de)*np.cos(np.pi*J2*t)*np.cos
(np.pi*J2*de)*relax

fid2          =
1*np.cos(np.pi*J1*t)*np.cos(np.p
i*J1*de)*np.sin(np.pi*J2*t)*np.s
in(np.pi*J2*de)*relax

fid3          =
1*np.sin(np.pi*J1*t)*np.sin(np.p
i*J1*de)*np.cos(np.pi*J2*t)*np.c
os(np.pi*J2*de)*relax

fid4          =
np.sin(np.pi*J1*t)*np.sin(np.pi*
J1*de)*np.sin(np.pi*J2*t)*np.sin
(np.pi*J2*de)*relax

freq = np.fft.fftfreq(TD)/dt

fid = fid + fid2 + fid3 + fid4

fid          =
np.exp(2j*np.pi*0*t)*(1+np.cos(n
p.pi*J1*de2)*np.cos(np.pi*J2*de2
))*fid

sig = np.fft.fft(fid)
sig_r = sig.real

np.savetxt('general.csv', sig_r,
delimiter=',')

plt.plot(freq, sig.real)

plt.show()

```

---

```

import numpy as np

import matplotlib.pyplot as plt

f_max = 4000
dt = 1/(2*f_max)
TD = 150
de = 0.0007+0.000036j
de2 = 0.0048
J1=36.5
J2=57

t = np.arange(0, TD*dt, dt)

```

```

relax = np.exp(-0.3*t)

sqcos =
np.square(np.cos((2*np.pi)/(4*TD
*dt)*t))

fid =
np.cos(6*np.pi*J1*t)*np.cos(np.p
i*J1*de)*np.cos(6*np.pi*J2*t)*np
.cos(np.pi*J2*de)*relax

fid2 = -
1*np.cos(6*np.pi*J1*t)*np.cos(np
.pi*J1*de)*np.sin(6*np.pi*J2*t)*
np.sin(np.pi*J2*de)*relax

fid3 = -
1*np.sin(6*np.pi*J1*t)*np.sin(np
.pi*J1*de)*np.cos(6*np.pi*J2*t)*
np.cos(np.pi*J2*de)*relax

fid4 =
np.sin(6*np.pi*J1*t)*np.sin(np.p
i*J1*de)*np.sin(6*np.pi*J2*t)*np
.sin(np.pi*J2*de)*relax

fid5 =
np.cos(6*np.pi*J1*t)*np.cos(np.p
i*J1*de)*np.cos(np.pi*J2*t)*np.c
os(np.pi*J2*de)*relax

fid6 = -
1*np.cos(6*np.pi*J1*t)*np.cos(np
.pi*J1*de)*np.sin(np.pi*J2*t)*np
.sin(np.pi*J2*de)*relax

fid7 = -
1*np.sin(6*np.pi*J1*t)*np.sin(np
.pi*J1*de)*np.cos(np.pi*J2*t)*np
.cos(np.pi*J2*de)*relax

fid8 =
np.sin(6*np.pi*J1*t)*np.sin(np.p
i*J1*de)*np.sin(np.pi*J2*t)*np.s
in(np.pi*J2*de)*relax

fid9 =
np.cos(np.pi*J1*t)*np.cos(np.pi*
J1*de)*np.cos(6*np.pi*J2*t)*np.c
os(np.pi*J2*de)*relax

fid10 = -
1*np.cos(np.pi*J1*t)*np.cos(np.p
i*J1*de)*np.sin(6*np.pi*J2*t)*np
.sin(np.pi*J2*de)*relax

fid11 = -
1*np.sin(np.pi*J1*t)*np.sin(np.p
i*J1*de)*np.cos(6*np.pi*J2*t)*np
.cos(np.pi*J2*de)*relax

fid12 =
np.sin(np.pi*J1*t)*np.sin(np.pi*
J1*de)*np.sin(6*np.pi*J2*t)*np.s
in(np.pi*J2*de)*relax

fid13 =
np.cos(np.pi*J1*t)*np.cos(np.pi*
J1*de)*np.cos(np.pi*J2*t)*np.cos
(np.pi*J2*de)*relax

fid14 = -
1*np.cos(np.pi*J1*t)*np.cos(np.p
i*J1*de)*np.sin(np.pi*J2*t)*np.s
in(np.pi*J2*de)*relax

fid15 = -
1*np.sin(np.pi*J1*t)*np.sin(np.p
i*J1*de)*np.cos(np.pi*J2*t)*np.c
os(np.pi*J2*de)*relax

fid16 =
np.sin(np.pi*J1*t)*np.sin(np.pi*
J1*de)*np.sin(np.pi*J2*t)*np.sin
(np.pi*J2*de)*relax

fid = 0.94*0.94*(fid + fid2 +
fid3 + fid4) + 0.94*0.06*(fid5 +
fid6 + fid7 + fid8) +
0.94*0.06*np.exp(1j*0.1*np.pi)*(
fid9 + fid10 + fid11 + fid12) +
0.06*0.06*(fid13 + fid14 + fid15
+ fid16)

fid = np.exp(2j*np.pi*0*t)*(fid)

#print(fid.size)

fid = fid * sqcos

zeros = np.zeros(4096)

```

```
for i in range(0, len(fid)-1):
    zeros[i] = fid.real[i] + zeros[i]

fid = zeros

sig = np.fft.fft(fid)
sig_r = sig.real
#np.savetxt('J_scale_7.csv',
sig_r, delimiter=',')

freq =
np.fft.fftfreq(len(fid))/dt

fig, ax = plt.subplots()
ax.plot(freq, sig_r, '-')
ax.set(xlabel='J (Hz)')
fig.savefig('spectrum.eps', format='eps')
plt.show()
```

---

## C Bibliography

---

- [1] Snyder, D. A.; Zhang, F.; Robinette, S. L.; Bruschweiler-Li, L.; Bruschweiler, R. Non-negative matrix factorization of two-dimensional NMR spectra: application to complex mixture analysis. *The Journal of Chemical Physics* **2008**, *128* (5), 052313.
- [2] Zhang, F.; Bruschweiler, R. Robust deconvolution of complex mixtures by covariance TOCSY spectroscopy. *Angewandte Chemie-International Edition* **2007**, *46* (15), 2639.
- [3] Zhang, F.; Bruschweiler-Li, L.; Robinette, S. L.; Bruschweiler, R. Self-consistent metabolic mixture analysis by heteronuclear NMR. Application to a human cancer cell line. *Analytical Chemistry* **2008**, *80* (19), 7549.
- [4] Zhang, F.; Bruschweiler, R. Spectral deconvolution of chemical mixtures by covariance NMR. *Chemphyschem* **2004**, *5* (6), 794.
- [5] Braunschweiler, L.; Ernst, R. R. Coherence Transfer by Isotropic Mixing - Application to Proton Correlation Spectroscopy. *Journal of Magnetic Resonance* **1983**, *53* (3), 521.
- [6] Otting, G.; Wuthrich, K. Efficient Purging Scheme for Proton-Detected Heteronuclear Two-Dimensional Nmr. *Journal of Magnetic Resonance* **1988**, *76* (3), 569.
- [7] Lee, S.; Wen, H.; An, Y. J.; Cha, J. W.; Ko, Y. J.; Hyberts, S. G.; Park, S. Carbon Isotopomer Analysis with Non-Uniform Sampling HSQC



- NMR for Cell Extract and Live Cell Metabolomics Studies. *Analytical Chemistry* **2017**, 89 (2), 1078.
- [8] Bruntz, R. C.; Lane, A. N.; Higashi, R. M.; Fan, T. W. Exploring cancer metabolism using stable isotope-resolved metabolomics (SIRM). *Journal of Biological Chemistry* **2017**, 292 (28), 11601.
- [9] Vinaixa, M.; Rodriguez, M. A.; Aivio, S.; Capellades, J.; Gomez, J.; Canyellas, N.; Stracker, T. H.; Yanes, O. Positional Enrichment by Proton Analysis (PEPA): A One-Dimensional (1) H-NMR Approach for (13) C Stable Isotope Tracer Studies in Metabolomics. *Angewandte Chemie-International Edition* **2017**, 56 (13), 3531.
- [10] Kover, K. E.; Forgo, P. J-modulated ADEQUATE (JM-ADEQUATE) experiment for accurate measurement of carbon-carbon coupling constants. *Journal of Magnetic Resonance* **2004**, 166 (1), 47.
- [11] Thiele, C. M.; Bermel, W. J-modulated ADEQUATE experiments using different kinds of refocusing pulses. *Magnetic Resonance in Chemistry* **2007**, 45 (10), 889.
- [12] Lin, Y.; Chen, Z.; Cai, S.; Zhong, J. High-resolution J-scaling nuclear magnetic resonance spectra in inhomogeneous fields via intermolecular multiple-quantum coherences. *Applied Spectroscopy* **2009**, 63 (5), 585.
- [13] Hosur, R. V. Scaling in One-Dimensional and 2-Dimensional Nmr-Spectroscopy in Liquids. *Progress in Nuclear Magnetic Resonance Spectroscopy* **1990**, 22, 1.

- [14] Willker, W.; Flogel, U.; Leibfritz, D. Ultra-high-resolved HSQC spectra of multiple-  $^{13}\text{C}$ -labeled biofluids. *Journal of Magnetic Resonance* **1997**, *125* (1), 216.
- [15] Ernst, R. R.; Bodenhausen, G.; Wokaun, A. *Principles of Nuclear Magnetic Resonance in One and Two Dimensions*; Clarendon press Oxford, 1987.
- [16] States, D. J.; Haberkorn, R. A.; Ruben, D. J. A Two-Dimensional Nuclear Overhauser Experiment with Pure Absorption Phase in 4 Quadrants. *Journal of Magnetic Resonance* **1982**, *48* (2), 286.
- [17] Marion, D.; Wuthrich, K. Application of Phase Sensitive Two-Dimensional Correlated Spectroscopy (Cosy) for Measurements of H-1-H-1 Spin-Spin Coupling-Constants in Proteins. *Biochemical and Biophysical Research Communications* **1983**, *113* (3), 967.
- [18] Bodenhausen, G.; Kogler, H.; Ernst, R. R. Selection of Coherence-Transfer Pathways in Nmr Pulse Experiments. *Journal of Magnetic Resonance* **1984**, *58* (3), 370.
- [19] Freeman, R. *Spin Choreography*; Oxford University Press Oxford, 1998.
- [20] Keeler, J.; Clowes, R. T.; Davis, A. L.; Laue, E. D. Pulsed-field gradients: theory and practice. *Methods in Enzymology* **1994**, *239*, 145.
- [21] Norwood, T. J. Magnetic-Field Gradients in Nmr - Friend or Foe. *Chemical Society Reviews* **1994**, *23* (1), 59.
- [22] Kupce, E.; Freeman, R. Stretched adiabatic pulses for broadband spin inversion. *Journal of Magnetic Resonance Series A* **1995**, *117* (2), 246.

- [23] Rosenfeld, D.; Zur, Y. A new adiabatic inversion pulse. *Magnetic Resonance in Medicine* **1996**, 36 (1), 124.
- [24] Wi, S.; Schurko, R. W.; Frydman, L. Broadband adiabatic inversion cross-polarization phenomena in the NMR of rotating solids. *Solid State Nuclear Magnetic Resonance* **2018**, 94, 31.
- [25] DeGraaf, R. A.; Nicolay, K. Adiabatic rf pulses: Applications to in vivo NMR. *Concepts in Magnetic Resonance* **1997**, 9 (4), 247.
- [26] Hwang, T. L.; van Zijl, P. C.; Garwood, M. Broadband adiabatic refocusing without phase distortion. *Journal of Magnetic Resonance* **1997**, 124 (1), 250.
- [27] Kupce, E.; Freeman, R. Compensated adiabatic inversion pulses: broadband INEPT and HSQC. *Journal of Magnetic Resonance* **2007**, 187 (2), 258.
- [28] Vancauteran, M.; Miot, F.; Segebarth, C. M.; Eisendrath, H.; Osteaux, M.; Willem, R. Excitation Characteristics of Adiabatic Half-Passage Rf Pulses Used in Surface Coil Mr Spectroscopy - Application to C-13 Detection of Glycogen in the Rat-Liver. *Physics in Medicine and Biology* **1992**, 37 (5), 1055.
- [29] Staewen, R. S.; Johnson, A. J.; Ross, B. D.; Parrish, T.; Merkle, H.; Garwood, M. 3-D FLASH imaging using a single surface coil and a new adiabatic pulse, BIR-4. *Investigative Radiology* **1990**, 25 (5), 559.
- [30] Johnson, A. J.; Garwood, M.; Ugurbil, K. Slice Selection with Gradient-Modulated Adiabatic Excitation Despite the Presence of Large B1-Inhomogeneities. *Journal of Magnetic Resonance* **1989**, 81 (3), 653.

- [31] Garwood, M.; Ugurbil, K.; Rath, A. R.; Bendall, M. R.; Ross, B. D.; Mitchell, S. L.; Merkle, H. Magnetic resonance imaging with adiabatic pulses using a single surface coil for RF transmission and signal detection. *Magnetic Resonance in Medicine* **1989**, 9 (1), 25.
- [32] Garwood, M.; Ke, Y. Symmetrical Pulses to Induce Arbitrary Flip Angles with Compensation for Rf Inhomogeneity and Resonance Offsets. *Journal of Magnetic Resonance* **1991**, 94 (3), 511.
- [33] de Graaf, R. A.; Nicolay, K.; Garwood, M. Single-shot, B1-insensitive slice selection with a gradient-modulated adiabatic pulse, BISS-8. *Magnetic Resonance in Medicine* **1996**, 35 (5), 652.
- [34] Bendall, M. R.; Pegg, D. T. Uniform Sample Excitation with Surface Coils for In vivo Spectroscopy by Adiabatic Rapid Half Passage. *Journal of Magnetic Resonance* **1986**, 67 (2), 376.
- [35] Yongbi, M. N.; Ding, S.; Dunn, J. F. Fat suppression at 7T using a surface coil: application of an adiabatic half-passage chemical shift selective radiofrequency pulse. *Journal of Magnetic Resonance Imaging* **1995**, 5 (6), 768.
- [36] de Graaf, R. A.; Luo, Y.; Garwood, M.; Nicolay, K. B1-insensitive, single-shot localization and water suppression. *Journal of Magnetic Resonance Series B* **1996**, 113 (1), 35.
- [37] Breton, R. C.; Reynolds, W. F. Using NMR to identify and characterize natural products. *Natural Product Reports* **2013**, 30 (4), 501.

- [38] Castanar, L.; Parella, T. Recent Advances in Small Molecule NMR: Improved HSQC and HSQMBC Experiments. *Annual Reports on NMR Spectroscopy* **2015**, *84*, 163.
- [39] Furrer, J. Recent Developments in HMBC Studies. *Annual Reports on NMR Spectroscopy* **2011**, *74*, 293.
- [40] Furrer, J. A comprehensive discussion of hmbc pulse sequences, part 1: The classical HMBC. *Concepts in Magnetic Resonance Part A* **2012**, *40a* (3), 101.
- [41] Furrer, J. A comprehensive discussion of HMBC pulse sequences. 2. Some useful variants. *Concepts in Magnetic Resonance Part A* **2012**, *40a* (3), 146.
- [42] Giraudeau, P.; Frydman, L. Ultrafast 2D NMR: an emerging tool in analytical spectroscopy. *Annual Review of Analytical Chemistry* **2014**, *7*, 129.
- [43] Halabalaki, M.; Vougiotiannopoulou, K.; Mikros, E.; Skaltsounis, A. L. Recent advances and new strategies in the NMR-based identification of natural products. *Current Opinion in Biotechnology* **2014**, *25*, 1.
- [44] Martin, G. E. Using 1,1-and 1,n-ADEQUATE 2D NMR Data in Structure Elucidation Protocols. *Annual Reports on NMR Spectroscopy* **2011**, *74*, 215.
- [45] Machonkin, T. E.; Westler, W. M.; Markley, J. L. (13)C[(13)C] 2D NMR: a novel strategy for the study of paramagnetic proteins with slow electronic relaxation rates. *Journal of the American Chemical Society* **2002**, *124* (13), 3204.

- [46] Eletsky, A.; Moreira, O.; Kovacs, H.; Pervushin, K. A novel strategy for the assignment of side-chain resonances in completely deuterated large proteins using  $^{13}\text{C}$  spectroscopy. *Journal of Biomolecular Nmr* **2003**, *26* (2), 167.
- [47] Bax, A.; Freeman, R.; Kempell, S. P. Natural Abundance C-13-C-13 Coupling Observed Via Double-Quantum Coherence. *Journal of the American Chemical Society* **1980**, *102* (14), 4849.
- [48] Bax, A.; Summers, M. F. H-1 and C-13 Assignments from Sensitivity-Enhanced Detection of Heteronuclear Multiple-Bond Connectivity by 2d Multiple Quantum Nmr. *Journal of the American Chemical Society* **1986**, *108* (8), 2093.
- [49] Furrer, J. A comprehensive discussion of HMBC pulse sequences. III. Solving the problem of missing and weakly observed long-range correlations. *Concepts in Magnetic Resonance Part A* **2014**, *43* (5), 177.
- [50] Zhang, F.; Bruschweiler, R. Indirect covariance NMR spectroscopy. *Journal of the American Chemical Society* **2004**, *126* (41), 13180.
- [51] Schoefberger, W.; Smrečki, V.; Vikić-Topić, D.; Müller, N. Homonuclear long-range correlation spectra from HMBC experiments by covariance processing. *Magnetic Resonance in Chemistry* **2007**, *45* (7), 583.
- [52] Barna, J. C. J.; Laue, E. D.; Mayger, M. R.; Skilling, J.; Worrall, S. J. P. Exponential Sampling, an Alternative Method for Sampling in Two-Dimensional Nmr Experiments. *Journal of Magnetic Resonance* **1987**, *73* (1), 69.

- 
- [53] Delaglio, F.; Walker, G. S.; Farley, K. A.; Sharma, R.; Hoch, J. C.; Arbogast, L. W.; Brinson, R. G.; Marino, J. P. Non-Uniform Sampling for All: More NMR Spectral Quality, Less Measurement Time. *American Pharmaceutical Review* **2017**, *20* (4).
- [54] Frueh, D. P.; Sun, Z. Y.; Vosburg, D. A.; Walsh, C. T.; Hoch, J. C.; Wagner, G. Non-uniformly sampled double-TROSY hNcaNH experiments for NMR sequential assignments of large proteins. *Journal of the American Chemical Society* **2006**, *128* (17), 5757.
- [55] Hoch, J. C. Modern spectrum analysis in nuclear magnetic resonance: alternatives to the Fourier transform. *Methods in Enzymology* **1989**, *176*, 216.
- [56] Kazimierczuk, K.; Orekhov, V. Non-uniform sampling: post-Fourier era of NMR data collection and processing. *Magnetic Resonance in Chemistry* **2015**, *53* (11), 921.
- [57] Rovnyak, D.; Frueh, D. P.; Sastry, M.; Sun, Z. Y.; Stern, A. S.; Hoch, J. C.; Wagner, G. Accelerated acquisition of high resolution triple-resonance spectra using non-uniform sampling and maximum entropy reconstruction. *Journal of Magnetic Resonance* **2004**, *170* (1), 15.
- [58] Rovnyak, D.; Hoch, J. C.; Stern, A. S.; Wagner, G. Resolution and sensitivity of high field nuclear magnetic resonance spectroscopy. *Journal of Biomolecular Nmr* **2004**, *30* (1), 1.
- [59] Schmieder, P.; Stern, A. S.; Wagner, G.; Hoch, J. C. Improved resolution in triple-resonance spectra by nonlinear sampling in the constant-time domain. *Journal of Biomolecular Nmr* **1994**, *4* (4), 483.

- [60] Schmieder, P.; Stern, A. S.; Wagner, G.; Hoch, J. C. Application of nonlinear sampling schemes to COSY-type spectra. *Journal of Biomolecular Nmr* **1993**, *3* (5), 569.
- [61] Sibisi, S.; Skilling, J.; Brereton, R. G.; Laue, E. D.; Staunton, J. Maximum-Entropy Signal-Processing in Practical Nmr-Spectroscopy. *Nature* **1984**, *311* (5985), 446.
- [62] Bruschiweiler, R.; Zhang, F. Covariance nuclear magnetic resonance spectroscopy. *The Journal of Chemical Physics* **2004**, *120* (11), 5253.
- [63] Bruschiweiler, R. Theory of covariance nuclear magnetic resonance spectroscopy. *The Journal of Chemical Physics* **2004**, *121* (1), 409.
- [64] Trbovic, N.; Smirnov, S.; Zhang, F.; Bruschiweiler, R. Covariance NMR spectroscopy by singular value decomposition. *Journal of Magnetic Resonance* **2004**, *171* (2), 277.
- [65] Bro, R.; Smilde, A. K. Principal component analysis. *Analytical Methods* **2014**, *6* (9), 2812.
- [66] Bodenhausen, G.; Ruben, D. J. Natural Abundance N-15 Nmr by Enhanced Heteronuclear Spectroscopy. *Chemical Physics Letters* **1980**, *69* (1), 185.
- [67] Furihata, K.; Seto, H. Decoupled Hmhc (D-Hmhc), an Improved Technique of Hmhc. *Tetrahedron Letters* **1995**, *36* (16), 2817.
- [68] Keeler, J.; Neuhaus, D. Comparison and Evaluation of Methods for Two-Dimensional Nmr-Spectra with Absorption-Mode Lineshapes. *Journal of Magnetic Resonance* **1985**, *63* (3), 454.
- [69] Davis, A. L.; Keeler, J.; Laue, E. D.; Moskau, D. Experiments for Recording Pure-Absorption Heteronuclear Correlation Spectra Using



- Pulsed Field Gradients. *Journal of Magnetic Resonance* **1992**, 98 (1), 207.
- [70] Kogler, H.; Sorensen, O. W.; Bodenhausen, G.; Ernst, R. R. Low-Pass J-Filters - Suppression of Neighbor Peaks in Heteronuclear Relayed Correlation Spectra. *Journal of Magnetic Resonance* **1983**, 55 (1), 157.
- [71] Kock, M.; Reif, B.; Fenical, W.; Griesinger, C. Differentiation of HMBC two- and three-bond correlations: A method to simplify the structure determination of natural products. *Tetrahedron Letters* **1996**, 37 (3), 363.
- [72] Delaglio, F.; Grzesiek, S.; Vuister, G. W.; Zhu, G.; Pfeifer, J.; Bax, A. NMRPipe: a multidimensional spectral processing system based on UNIX pipes. *Journal of Biomolecular Nmr* **1995**, 6 (3), 277.
- [73] Hyberts, S. G.; Milbradt, A. G.; Wagner, A. B.; Arthanari, H.; Wagner, G. Application of iterative soft thresholding for fast reconstruction of NMR data non-uniformly sampled with multidimensional Poisson Gap scheduling. *Journal of Biomolecular Nmr* **2012**, 52 (4), 315.
- [74] Blasko, G.; Shieh, H. L.; Pezzuto, J. M.; Cordell, G. A. <sup>13</sup>C-nmr spectral assignment and evaluation of the cytotoxic potential of rotenone. *Journal of Natural Products* **1989**, 52 (6), 1363.
- [75] Verpoorte, R. Assignment of <sup>13</sup>C-NMR spectra of strychnine and brucine. *Journal of Pharmaceutical Sciences* **1980**, 69 (7), 865.
- [76] Morris, G. A.; Freeman, R. Enhancement of Nuclear Magnetic-Resonance Signals by Polarization Transfer. *Journal of the American Chemical Society* **1979**, 101 (3), 760.

- [77] Takeda, K.; Kobayashi, Y.; Noda, Y.; Takegoshi, K. Inner-product NMR spectroscopy: A variant of covariance NMR spectroscopy. *Journal of Magnetic Resonance* **2018**, *297*, 146.
- [78] Krishnamurthy, K.; Seffler, A. M.; Russell, D. J. Application of CRAFT in two-dimensional NMR data processing. *Magnetic Resonance in Chemistry* **2017**, *55* (3), 224.
- [79] Bingol, K.; Salinas, R. K.; Bruschweiler, R. Higher-Rank Correlation NMR Spectra with Spectral Moment Filtering. *Journal of Physical Chemistry Letters* **2010**, *1* (7), 1086.
- [80] Harden, B. J.; Nichols, S. R.; Frueh, D. P. Facilitated assignment of large protein NMR signals with covariance sequential spectra using spectral derivatives. *Journal of the American Chemical Society* **2014**, *136* (38), 13106.
- [81] Helmus, J. J.; Jaroniec, C. P. Nmr glue: an open source Python package for the analysis of multidimensional NMR data. *Journal of Biomolecular Nmr* **2013**, *55* (4), 355.
- [82] Jaspars, M. Computer assisted structure elucidation of natural products using two-dimensional NMR spectroscopy. *Natural Product Reports* **1999**, *16* (2), 241.
- [83] Yoon, J. W.; Godsill, S.; Kupce, E.; Freeman, R. Deterministic and statistical methods for reconstructing multidimensional NMR spectra. *Magnetic Resonance in Chemistry* **2006**, *44* (3), 197.
- [84] Orekhov, V. Y.; Jaravine, V. A. Analysis of non-uniformly sampled spectra with multi-dimensional decomposition. *Progress in Nuclear Magnetic Resonance Spectroscopy* **2011**, *59* (3), 271.

- 
- [85] Mobli, M.; Hoch, J. C. Maximum Entropy Spectral Reconstruction of Non-Uniformly Sampled Data. *Concepts in Magnetic Resonance Part A* **2008**, *32A* (6), 436.
- [86] Hyberts, S. G.; Heffron, G. J.; Tarragona, N. G.; Solanky, K.; Edmonds, K. A.; Luithardt, H.; Fejzo, J.; Chorev, M.; Aktas, H.; Colson, K. et al. Ultrahigh-resolution (1)H-(13)C HSQC spectra of metabolite mixtures using nonlinear sampling and forward maximum entropy reconstruction. *Journal of the American Chemical Society* **2007**, *129* (16), 5108.
- [87] Hyberts, S. G.; Frueh, D. P.; Arthanari, H.; Wagner, G. FM reconstruction of non-uniformly sampled protein NMR data at higher dimensions and optimization by distillation. *Journal of Biomolecular Nmr* **2009**, *45* (3), 283.
- [88] Linnet, T. E.; Teilum, K. Non-uniform sampling of NMR relaxation data. *Journal of Biomolecular Nmr* **2016**, *64* (2), 165.
- [89] Gruetter, R.; Adriany, G.; Choi, I. Y.; Henry, P. G.; Lei, H.; Oz, G. Localized in vivo <sup>13</sup>C NMR spectroscopy of the brain. *Nmr in Biomedicine* **2003**, *16* (6-7), 313.
- [90] Sorensen, O. W.; Eich, G. W.; Levitt, M. H.; Bodenhausen, G.; Ernst, R. R. Product Operator-Formalism for the Description of Nmr Pulse Experiments. *Progress in Nuclear Magnetic Resonance Spectroscopy* **1983**, *16*, 163.
- [91] Palmer, A. G.; Cavanagh, J.; Wright, P. E.; Rance, M. Sensitivity Improvement in Proton-Detected 2-Dimensional Heteronuclear

- Correlation Nmr-Spectroscopy. *Journal of Magnetic Resonance* **1991**, 93 (1), 151.
- [92] Kay, L. E.; Keifer, P.; Saarinen, T. Pure Absorption Gradient Enhanced Heteronuclear Single Quantum Correlation Spectroscopy with Improved Sensitivity. *Journal of the American Chemical Society* **1992**, 114 (26), 10663.
- [93] Price, W. S. Pulsed-field gradient nuclear magnetic resonance as a tool for studying translational diffusion: Part II. Experimental aspects. *Concepts in Magnetic Resonance* **1998**, 10 (4), 197.
- [94] Marion, D.; Ikura, M.; Tschudin, R.; Bax, A. Rapid Recording of 2d Nmr-Spectra without Phase Cycling - Application to the Study of Hydrogen-Exchange in Proteins. *Journal of Magnetic Resonance* **1989**, 85 (2), 393.
- [95] Mehlkopf, A. F.; Korbee, D.; Tiggelman, T. A.; Freeman, R. Sources of T1 Noise in Two-Dimensional Nmr. *Journal of Magnetic Resonance* **1984**, 58 (2), 315.
- [96] Lin, G.; Liao, X.; Lin, D.; Zheng, S.; Chen, Z.; Wu, Q. t(1) noise and sensitivity in pulsed field gradient experiments. *Journal of Magnetic Resonance* **2000**, 144 (1), 6.
- [97] Bain, A. D. Coherence Levels and Coherence Pathways in Nmr - a Simple Way to Design Phase Cycling Procedures. *Journal of Magnetic Resonance* **1984**, 56 (3), 418.
- [98] Hwang, T. L.; van Zijl, P. C.; Garwood, M. Fast broadband inversion by adiabatic pulses. *Journal of Magnetic Resonance* **1998**, 133 (1), 200.

- [99] Levitt, M. H.; Freeman, R. Compensation for Pulse Imperfections in Nmr Spin-Echo Experiments. *Journal of Magnetic Resonance* **1981**, *43* (1), 65.
- [100] Stott, K.; Stonehouse, J.; Keeler, J.; Hwang, T. L.; Shaka, A. J. Excitation Sculpting in High-Resolution Nuclear-Magnetic-Resonance Spectroscopy - Application to Selective Noe Experiments. *Journal of the American Chemical Society* **1995**, *117* (14), 4199.
- [101] Hwang, T. L.; Shaka, A. J. Water Suppression That Works - Excitation Sculpting Using Arbitrary Wave-Forms and Pulsed-Field Gradients. *Journal of Magnetic Resonance Series A* **1995**, *112* (2), 275.
- [102] Kobzar, K.; Skinner, T. E.; Khaneja, N.; Glaser, S. J.; Luy, B. Exploring the limits of broadband excitation and inversion pulses. *Journal of Magnetic Resonance* **2004**, *170* (2), 236.
- [103] Kobzar, K.; Skinner, T. E.; Khaneja, N.; Glaser, S. J.; Luy, B. Exploring the limits of broadband excitation and inversion: II. Rf-power optimized pulses. *Journal of Magnetic Resonance* **2008**, *194* (1), 58.
- [104] Smith, M. A.; Hu, H.; Shaka, A. J. Improved broadband inversion performance for NMR in liquids. *Journal of Magnetic Resonance* **2001**, *151* (2), 269.

국문초록

## 고해상도 $^{13}\text{C}$ - $^{13}\text{C}$ NMR

### 스펙트럼을 활용한 혼합물 분석

차 진 욱

천연물과학 전공

약학과

서울대학교 대학원

$^{13}\text{C}$ - $^{13}\text{C}$  상호작용에 의한 짝지음은 ( $J_{\text{CC}}$  coupling) 탄소골격으로 이루어진 유기화합물의 NMR 기반 구조분석에 있어 매우 중요한 정보이다. 그러나  $^{13}\text{C}$  핵의 낮은 자연존재 비로 인해 이들의 직접적인 NMR 상관관계 분석은 매우 제한된 영역에서 이루어졌다. 이 연구에서 이러한  $^{13}\text{C}$ - $^{13}\text{C}$  상호작용을 활용한 천연물/혼합물 및 대사체 분석에 응용될 수 있는 신규 NMR 분석법을 개발하고 그 적용결과를 제시하였다.

첫째로 이차원  $^1\text{H}$ - $^{13}\text{C}$  HMBC 스펙트럼을 통한 고해상도  $^{13}\text{C}$ - $^{13}\text{C}$  상관 스펙트럼의 생성방법에 관한 연구를 수행하였고, 이를 실제 천연물 (로테논, rotenone)에 적용하여 구조분석에 대한 활용가능성을 평가하였다.

또한, 이렇게 얻어진  $^{13}\text{C}$ - $^{13}\text{C}$  상관 스펙트럼으로부터 복잡한 천연물의 구조분석을 위한 신규 후처리 기법 (DECODE procedure)을 제안하였다. 이후 이를 실제 천연물의 혼합물에 적용하여 혼합물의 NMR 스펙트럼으로부터 개별 순수 화합물의  $^{13}\text{C}$  스펙트럼을 추출할 수 있음을 확인하였다. 많은 4 차탄소를 포함하는 로테논 및 브루신 (brucine)과 같은 복잡한 구조를 지닌 천연물의 혼합물에 DECODE 분석법을 적용하였을 때, 매우 인접한 개별 탄소신호들을 포함, 각 화합물의 개별  $^{13}\text{C}$  스펙트럼을 성공적으로 추출하였다. 이 방법은 복잡한 구조를 지닌 유기 혼합물의 범용적인  $^1\text{H}$ - $^{13}\text{C}$  이차원 상관 NMR 스펙트럼으로부터 개별 분자의  $^{13}\text{C}$ - $^{13}\text{C}$  상관정보 및 개별 탄소 정보를 제공하므로 천연물 구조화학을 포함한 다양한 분야의 NMR 분석연구에 적용될 수 있을 것이다.

다음으로, 세포 추출물과 같은 대사체 화합물에서 흔히 활용되는  $^{13}\text{C}$  동위원소 표지 화합물의 HSQC 스펙트럼에서  $^{13}\text{C}$ - $^{13}\text{C}$  상호작용에 의한 신호 갈라짐을 효과적으로 분석할 수 있는 새로운  $^1\text{H}$ - $^{13}\text{C}$  상관 NMR 분석법 (HSQC)을 개발하였다.  $^{13}\text{C}$ - $^{13}\text{C}$  상호작용에 의한 신호 갈라짐은 특정 대사과정의 분석에 매우 효과적으로 활용될 수 있으므로 그 정확한 형태 및 짝지음 상수 ( $J_{\text{CC}}$  constant) 등의 분석은 매우 중요한 대사과정 측면의 구조 정보를 제공할 수 있다. 이 연구에서는 이러한  $^{13}\text{C}$ - $^{13}\text{C}$  상호작용 정보를 효과적으로 분석할 수 있는 새로운  $^1\text{H}$ - $^{13}\text{C}$  HSQC 측정 시퀀스를 제안하였고 이를 실제  $^{13}\text{C}$  동위원소로 표지된 U- $^{13}\text{C}$  아세테이트 및 락테이트와 같은 대사체 화합물에 적용하여 기존 HSQC 측정 결과와 비교, 새롭게 고안된 측정 시퀀스가 기존 방법 대비 매우 개선된  $^{13}\text{C}$ - $^{13}\text{C}$  상호작용 정보를 제공할 수 있음을 확인하였다.

새로 개발된 HSQC 측정 시퀀스는 상대적으로 짧은 측정시간에도 고해상도의  $^{13}\text{C}$ - $^{13}\text{C}$  상호작용에 의한 신호 갈라짐 정보를 제공할 수 있으므로 실시간 NMR 대사체 분석과 같은 측정시간의 제약이 있는 분석연구에도 효과적으로 적용될 수 있을 것이다.

**주요어:** 탄소-탄소 상관,  $J$ -짝지움, 공분산, 스펙트럼 디컨볼루션, 혼합물분석, 천연물

**학번:** 2016-30517